Geophys. J. R. astr. Soc. (1983) **74**, 377–449

Glacial isostatic adjustment and the free air gravity anomaly as a constraint on deep mantle viscosity

Patrick Wu and W. R. Peltier *Department of Physics, University of Toronto, Toronto, Ontario M5S 1A7, Canada*

Received 1982 October 6; in original form 1982 February 22

Summary. A gravitationally self-consistent theory for relative sea-level variations forced by Pleistocene deglaciation events is employed to explore the extent to which RSL and free air gravity observations together constrain the viscosity of the mantle beneath the seismic discontinuity at 670 km depth. A trade-off is revealed between errors in the assumed deglaciation history and errors in the inferred value of the viscosity of the lower mantle. Taking full account of such uncertainty, plausible values of the viscosity beneath the transition region are bounded above by 10^{23} poise (cgs units). The preferred value is at least a factor of 2 lower than this and is strongly constrained by the observed free air gravity anomaly over Hudson Bay. The calculations described in detail here show for the first time that the relatively large gravity anomalies observed over sites of Würm–Wisconsin deglaciation do not require any pronounced increase of mantle viscosity with depth in order to explain them.

1 Introduction

The magnitude of the viscosity contrast across the seismic discontinuity at 670 km depth provides an important constraint on models of the mantle convective circulation (e.g. Peltier 1980, 1981). The only direct means which we have available to measure this contrast is through analysis of the various signatures of the process of glacial isostatic adjustment. There are three general classes of such data which have been shown to be particularly useful: relative sea-level histories, present-day gravity anomalies and historical records of polar motion. Histories of relative sea-level (RSL) are obtained from C^{14} dated material in relict beaches at various heights above or depths below present-day sea-level. Such RSL curves are now available from an extremely large set of geographic locations and constitute the primary data base for studies of glacial isostasy. A detailed theoretical model now exists which may be employed to investigate the extent to which the RSL data themselves may serve to constrain the mantle viscosity profile. This model has been developed in Peltier (1974, 1976, 1980, 1981, 1982), Peltier & Andrews (1976), Farrell & Clark (1976), Peltier, Farrell & Clark (1978), Clark, Farrell & Peltier (1978), and extended in Wu & Peltier (1982). The full model has not previously been employed to investigate the sensitivity of the RSL

predictions to variations of the mantle viscosity profile. One purpose of this paper is to describe the results of such an investigation which is focused upon an attempt to constrain the magnitude of the viscosity contrast across the 670 km seismic discontinuity.

The second class of data for glacial isostatic adjustment, and one which has played an important role in the historical development of the subject, consists of observations of the free air gravity anomaly over previously ice-covered centres of rebound. The interpretation of these data has been extremely controversial. One reason for the controversy has been that early efforts were restricted to consideration of the gravitational field over Fennoscandia, a field which is influenced by complex geological and topographic variations as well as by the degree of glacial isostatic disequilibrium. Niskanen (1939), for example, believed there to be an anomaly of −30 mgal over the Gulf of Bothnia and deduced from this that there must be approximately 200 m of uplift remaining in this region before glacial isostatic equilibrium would be restored. Heiskanen & Vening Meinesz (1958) determined that this anomaly was only −20 mgal and found it to be in accord with relaxation at a rate compatible with a mantle viscosity of 10^{22} poise. Honkasolo (1964), on the other hand, compiled a gravity map for all of Fennoscandia and concluded from it that there was no spatial correlation between the gravity anomaly and the region of most rapid present-day emergence. He found, rather, a strong correlation with the local geological structure. Cathles (1975) averaged the gravity map of Honkasolo and obtained an anomaly of −3.5 mgal corresponding to 25 m of remaining uplift. The most recent and complete analysis of the Fennoscandia data is that by Balling (1980). He averaged the observed anomalies over $2^\circ \times 4^\circ$ grids and removed that part of the anomaly which was correlated with topography. The residual anomaly was found to be approximately −20 mgal and was very well correlated with the region of present-day emergence. This is the same anomaly obtained by Heiskanen & Vening Meinesz (1958) and we will provide further theoretical support for its validity here.

The free air gravity anomaly which is centred on Hudson Bay and well correlated spatially with the ancient Laurentide ice sheet is relatively uncontaminated by topographic and geological noise. The map compiled by Walcott (1970) is dominated by an elliptical negative anomaly of about −35 mgal with a zero anomaly contour very nearly coincident with the location of the ice margin at 18 kBP. On the basis of the magnitude of the observed anomaly Walcott deduced an amount of uplift remaining of about 200 m. Given the relatively short relaxation time of about 1700 yr indicated by the RSL data from the Richmond Gulf of Hudson Bay (e.g. Peltier, Yuen & Wu 1980a; Peltier, Wu & Yuen 1980b) it did not seem possible to Walcott that a simple model with uniform viscosity could reconcile both data sets. In order to circumvent this difficulty he proposed a model in which each wavelength in the relaxation spectrum was governed by two characteristic decay times and ascribed this property to a layering of the viscosity structure such that the upper mantle had a characteristic viscosity of 10^{22} poise whereas the lower mantle had a characteristic viscosity considerably in excess of 10^{23} poise. This channel flow model for the Canadian rebound was preferred by both Artyushkov (1971) and Walcott (1972) and had been suggested previously by Van Bemmelen & Berlage (1935) for Fennoscandia. Cathles (1975) accepted O'Connell's (1971) conclusion, based upon an early satellite geopotential map for spherical harmonic degrees 2–14, that there was no perceptible anomaly correlating with the centre of rebound. More recent satellite data (e.g. Philips & Lambeck 1980), however, show the same anomaly over Hudson Bay of about −35 mgal as is evident on Walcott's surface map.

A second purpose of the present paper is to demonstrate that the controversy over the interpretation of free air gravity data which is evident in the above cited references may be

resolved in a very straightforward way when realistic viscoelastic models of the planet constructed in Wu & Peltier (1982, companion paper) are employed. We will show that the same models which fit the RSL data simultaneously reconcile the observed free air gravity anomalies over *both* Hudson Bay and Fennoscandia. As we will also show, the earth models which fit the data are characterized by a viscosity contrast across 670 km depth which is considerably less than an order of magnitude. When the RSL and gravity data are combined with the third class of glacial isostatic adjustment information the constraint on the viscosity of the deep mantle becomes very tight indeed. This third class of data consists of historical polar motion observations and of the observed non-tidal component of the acceleration of the Earth's rotation. Peltier (1982) has shown that both the secular drift of the pole evident in the ILS pole path (which is occurring at the rate of about $1^\circ/10^6$ yr) and the non-tidal acceleration are due to deglacial forcing. Although these data do not in themselves yield a unique measurement of mantle viscosity they are extremely important because, being sensitive only to the long-wavelength second-degree harmonic of the deglaciation induced deformation, they are sensitive essentially to the mean viscosity of the entire mantle. Of the two values of the mean mantle viscosity which are compatible with the rotation data, $\approx 1.5 \times 10^{22}$ and $\approx 3 \times 10^{23}$ poise, only the former is simultaneously able to reconcile the RSL and free air gravity information.

The feature of our realistic viscoelastic earth models which allows them simultaneously to fit the relative sea-level and free air gravity data with no substantial increase of viscosity with depth is the fact that each deformation wavelength in these models is governed by a decay spectrum which consists of more than a single relaxation time (Peltier 1976). These extra modes are supported not, as Walcott supposed, by the viscosity structure in the model but rather by the major radial density discontinuities which are characteristic of planetary models which satisfy the data of body wave and free oscillation seismology (e.g. Gilbert & Dziewonski 1975). In the Earth, the important density discontinuities are those across the Mohorovičić discontinuity, across the olivine → spinel and the spinel → perovskite + magnesiowustite phase transitions at 420 and 670 km depths respectively, and across the core–mantle interface. In so far as glacial isostasy is concerned the most important boundary is that which marks the 670 km phase transition because of the relatively shallow depth at which the boundary is located and the relatively large density increase which takes place across it. Since the extra modes of relaxation supported by these boundaries may have relaxation times somewhat in excess of 10^5 yr, their existence poses an important question as to the influence which initial isostatic disequilibrium (prior to deglaciation) might have upon the inference of mantle viscosity from isostatic adjustment data. As has been suggested previously (Peltier 1982; Wu & Peltier 1982) oxygen isotope data from deep sea sedimentary cores may be employed to estimate the time-scale of the glaciation–deglaciation cycle and this information may in turn be employed to investigate the importance of initial disequilibrium. An additional purpose of the present paper will be to provide a more complete analysis of this problem.

The paper is arranged as follows. Section 2 contains a complete description of the gravitationally self-consistent model of glacial isostatic adjustment and a discussion of numerical methods. It also discusses the relationship between the gravitationally self-consistent theory and approximate methods of solution which have been employed previously. This discussion establishes by direct numerical comparison that the self-consistent theory is necessary for some applications. Section 3 is devoted to a description of the inputs which are required for the adjustment calculation and Section 4 consists of a discussion of the observations which the theoretical model is intended to explain. Computational results discussed in Section 5 are based upon the assumption of initial isostatic

equilibrium while those presented in Section 6 constitute an attempt to provide a direct assessment of the effects of initial disequilibrium upon various observational signatures of the response. Section 7 is devoted to an investigation of the sensitivity of the results to errors in the deglaciation history. Our conclusions are summarized in Section 8 in which the reader will also find a discussion of the implications of our results to the question of the style of convection in the Earth's mantle.

2 A gravitationally self-consistent model of glacial isostatic adjustment

2.1 THE SEA-LEVEL EQUATION

The theoretical prediction of relative sea-level histories and anomalies in the present-day free air gravity field due to Pleistocene deglaciation requires two distinctly different pieces of input information. The first is a glaciation–deglaciation history which can be described in terms of a functional $L_I(\mathbf{r}, t)$ which gives the variation in space and time of ice thickness on the Earth's surface. The second input which is required for such calculations is a viscosity profile for the Earth's mantle $\nu(r)$ which, when coupled with the seismically determined profile of density $\rho(r)$ and elastic Lame parameters $\lambda(r)$ and $\mu(r)$, can be employed to calculate a Green's function $G(\mathbf{r}, t)$ for the surface mass load boundary value problem (see previously cited references, including Wu & Peltier 1982). A detailed discussion of these two inputs will be found in the following section. Here we shall assume that these inputs are known and focus upon the theoretical structure of the numerical calculation which must be performed to make RSL and free air gravity predictions from them.

The first step in this calculation is to solve an equation which tells us how the meltwater produced by deglaciation is distributed over the major ocean basins. It should be quite clear on physical grounds that the increase in ocean bathymetry effected by glacial disintegration cannot be independent of geographic location. Rather, meltwater must be distributed over the surface of the global ocean in such a way that the surface of the ocean (geoid) is at all times a surface of constant gravitational potential. As deglaciation proceeds, perturbations of potential on the ocean surface are produced not only by the redistribution of the surface load but also by the elastic and viscous redistribution of matter in the interior of the planet which this loading forces. Farrell & Clark (1976), Clark *et al.* (1978), and Peltier *et al.* (1978) derive an equation, which we will call the sea-level equation, solution of which yields the space- and time-dependent change of ocean bathymetry which is required to keep the gravitational potential of the sea surface constant for a specific deglaciation chronology and viscoelastic earth model. We will provide a brief sketch of the derivation of this equation here and note that it follows a discussion given by Platzman (1971) and elaborated by Farrell (1973) for the effect of redistribution of water on the ocean tides produced by tidal loading of the seafloor. An early discussion of the basic idea will be found in Woodward (1888).

The change in potential Φ on the ocean surface at point $\mathbf{r}$ and time t produced by the melting event $L_I(\mathbf{r}, t)$ which generates bathymetry change $S(\mathbf{r}, t)$ may be calculated from

$$\Phi(\mathbf{r}, t) = \rho_I L_I *_I \varphi + \rho_w S *_o \varphi \tag{1}$$

in which $*_I$ and $*_o$ indicate convolution over the ice and convolution over the ocean respectively, where ρ_I and ρ_w are the densities of ice and water respectively and where φ is the potential perturbation Green's function (Peltier & Andrews 1976). The convolution operations in (1) are also implicitly over time as well as space from $t = -\infty$ until present time t. The change of potential Φ also causes a change in sea-level with respect to the surface of the

deformed Earth which is in the amount

$$S(\mathbf{r}, t) = \frac{\Phi(r, t)}{g} + C \tag{2}$$

where g is the gravitational acceleration at the Earth's surface and C is a constant determined such as to ensure conservation of mass. Mass conservation demands that the integral of the product $\rho_w S$ over the oceans is equal to the prescribed mass loss history of the ice sheets, i.e.

$$\langle \rho_w S \rangle_o = \rho_w \left\langle \rho_I L_I *_I \frac{\varphi}{g} + \rho_w S *_o \frac{\varphi}{g} \right\rangle_o + \rho_w \langle C \rangle_o = -\dot{M}_I(t) \tag{3}$$

where $M_I(t) = \langle \rho_I L_I \rangle_I$ is the known mass loss history of the ice sheets. $\langle \ \rangle_o$ and $\langle \ \rangle_I$ represent integration over the oceans and ice sheets respectively. Since C is a constant, $\langle C \rangle_o = CA_o$ where A_o is the total area of the ocean surface. Substituting from (3) for C into (2) the final form of the sea-level equation is

$$S = \rho_I \frac{\varphi}{g} *_I L_I + \rho_w S *_o \frac{\varphi}{g} - \frac{1}{A_o} \left\langle \rho_I L_I *_I \frac{\varphi}{g} + \rho_w S *_o \frac{\varphi}{g} \right\rangle_o - \frac{M_I(t)}{\rho_w A_o} . \tag{4}$$

In (4) we note that S is the local variation of sea-level with respect to the deformed surface of the solid earth and that this is precisely the variation of sea-level which is recorded in radiocarbon controlled RSL histories.

2.2 DISCRETIZATION OF THE SEA-LEVEL EQUATION

The sea-level equation (4) is an integral equation because the unknown field S appears both on the left-hand side and in the convolution integrals on the right-hand side. In order to solve (4) it must be discretized both in time and in space. For the purposes of all of the calculations to be discussed here we have elected to sample the temporal evolution of the fields at a sampling interval of 10^3 yr. The deglaciation history, for example, is replaced by a sequence of step load removals or additions δL_i separated by $\Delta t = t_i - t_{i-1} = 10^3$ yr as

$$L_I(\mathbf{r}^1, t) = \sum_{l=0}^{P} \delta L_l(\mathbf{r}^1) H(t - t_l) \tag{5}$$

in which $H(t)$ is the Heaviside step function. With this discretization in time the sea-level equation (4) may be rewritten as

$$\begin{aligned} S(\mathbf{r}, t) = & \int_I \int \rho_I L_I(\mathbf{r}^1, t) G^E(\mathbf{r} - \mathbf{r}^1) \, d^2 r^1 + \int_o \int \rho_w S(\mathbf{r}^1, t) G^E(\mathbf{r} - \mathbf{r}^1) \, d^2 r^1 \\ & + \rho_I \sum_{l=0}^{P} \int_I \int \delta L_l(\mathbf{r}^1) G^{H,V}(\mathbf{r} - \mathbf{r}^1, t - t_l) \, d^2 r^1 \\ & + \rho_w \sum_{l=0}^{P} \int_o \int \delta S_l(\mathbf{r}^1) G^{H,V}(\mathbf{r} - \mathbf{r}^1, t - t_l) \, d^2 r^1 - C(t). \end{aligned} \tag{6}$$

In (6) δS_l is the increment in seawater thickness at time $t = t_l$ and the convolution of the Heaviside step functions in (5) with φ/g gives $\varphi^H/g = G^H = G^E + G^{H,V}$ for the kernel of the convolution integrals. The expansion of the Green's functions into elastic and viscous parts

follows Peltier (1974) and Peltier & Andrews (1976). The function $C(t)$ in (6) is given by

$$C(t) = \frac{\perp}{A_o}\left[\int_o\int d^2r \int_o\int \rho_I L_I(\mathbf{r}^1, t)\, G^E(\mathbf{r}-\mathbf{r}^1)\, d^2r^1 + \int_o\int d^2r \int_o\int \rho_w S(\mathbf{r}^1, t)\, G^E(\mathbf{r}-\mathbf{r}^1)\, d^2r^1 + \int_o\int d^2r \left\{\sum_{l=0}^{P}\int_I\int \rho_I \delta L_1(\mathbf{r}^1)\, G^{H,V}(\mathbf{r}-\mathbf{r}^1, t-t_1)\, d^2r^1\right\} + \int_o\int d^2r \left\{\sum_{l=0}^{P}\int_o\int \rho_w \delta S_1(\mathbf{r}^1)\, G^{H,V}(\mathbf{r}-\mathbf{r}^1, t-t_1)\, d^2r^1\right\}\right] + S_{EUS}(t) \tag{7}$$

where the 'eustatic' water rise is just

$$S_{EUS}(t) = \frac{\rho_I}{\rho_w A_o}\iint_I L_I(\mathbf{r}^1, t)\, d^2r^1. \tag{8}$$

It remains to discretize the spatial dependence in (6). In order to accomplish this what we do (Peltier *et al.* 1978) is to divide the surface of the Earth into a number of finite geometric elements. The 'active' elements cover all of the ocean surface and those regions of the continents where glaciation and deglaciation actually take place. For the calculations to be discussed here the ice-covered portions of the surface are covered by 236 elements, all equally spaced with 5° of longitude or latitude separating the centroids of adjacent elements. The ice grid over North America is shown in Fig. 1(a) while that over Europe is shown in

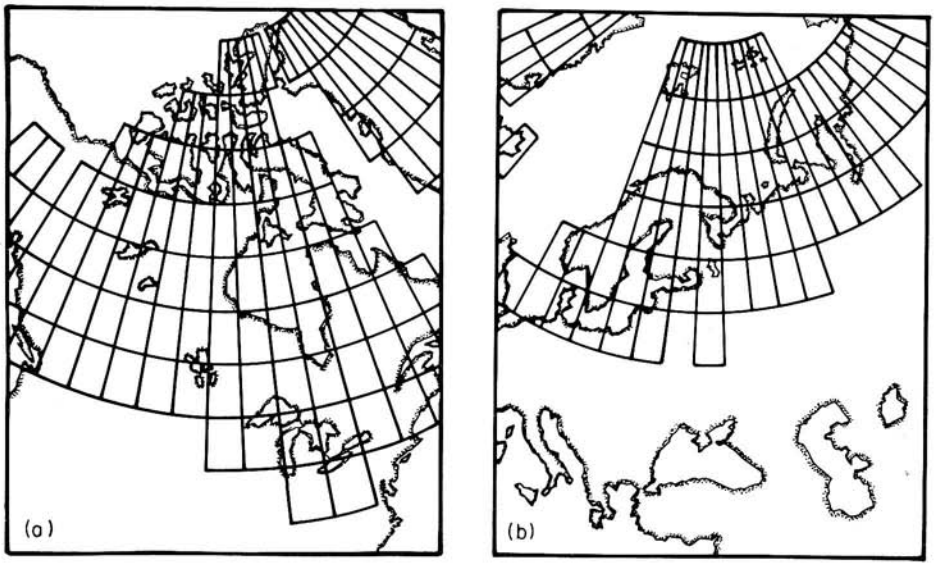

Figure 1. Density and distribution of the grid elements under the ice in (a) Laurentide, (b) Fennoscandia.

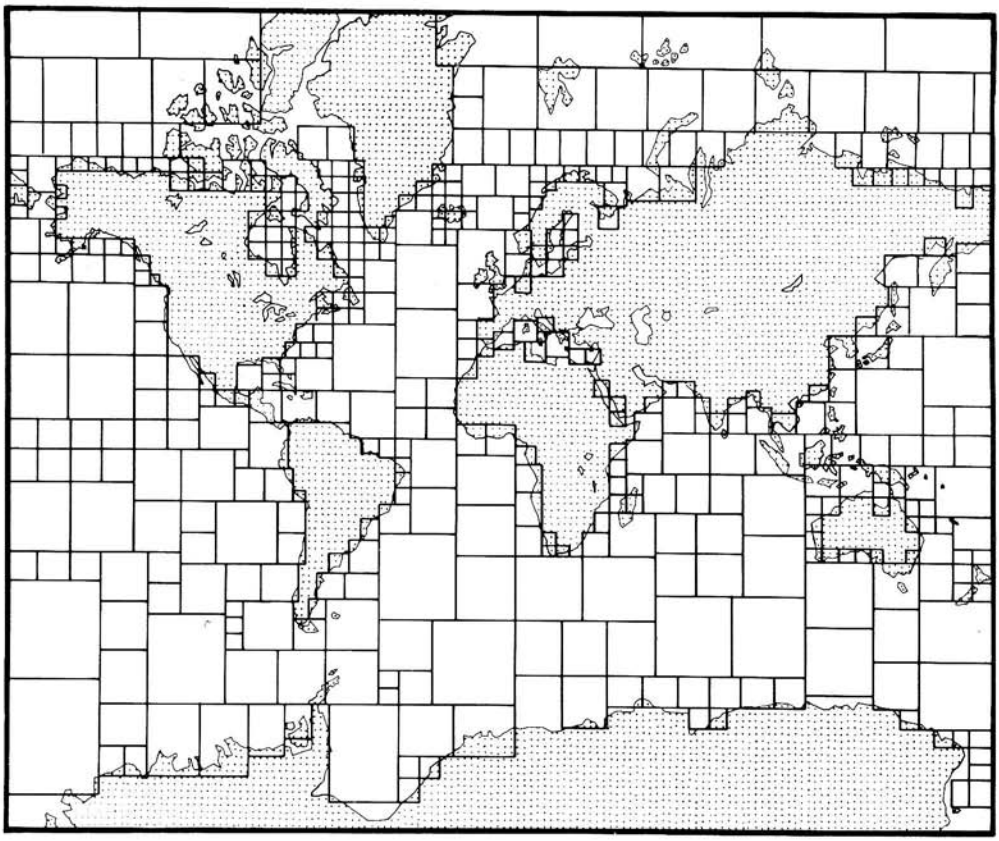

Figure 2. Density and distribution of the grid elements in the ocean.

Fig. 1(b). The ocean basins are covered by 470 elements but these are not spaced uniformly, the small elements being packed close to continental shorelines. The largest oceanic elements are located in the central basins and span 20° of latitude and longitude. The density of the ocean grid is illustrated in Fig. 2.

If we denote the area of the jth active element by E_j and assume that the loads on each element are piecewise constant in time, then at the centroid of the ith element, $\mathbf{r}_i$, equation (6) may be written in discrete form as

$$S_{ip} = \rho_w G^E_{ij} S_{jp} + \rho_I G^E_{ij} I_{jp} + \rho_w G^{H,V}_{ijpl} \delta S_{jl} + \rho_I G^{H,V}_{ijpl} \delta I_{jl} - \frac{\rho_I}{\rho_w A_o} E_j I_{jp}$$

$$- \frac{1}{A_o} \left\{ E_k (\rho_w G^E_{kj} S_{jp} + \rho_I G^E_{kj} I_{jp} + \rho_w G^{H,V}_{kplj} \delta S_{jl} + \rho_I G^{H,V}_{kplj} \delta I_{jl} \right\} . \quad (9)$$

In writing (9) we have made use of the convention of summation over repeated indices. For terms involving S_{jp} and δS_{jp}, j is summed over the finite elements in the ocean from 1 to $N(= 470)$. For terms in I_{jp} and δI_{jp}, j is summed over the elements in the ice sheets from 1 to $M(= 236)$. Terms involving δS_{jp} and δI_{jp} have p summed from 1 to P_0 where P_0 is the number of time intervals ($\Delta t = 10^3$ yr) since deglaciation commenced. The matrices which

appear in (9) are defined as:

$S_{ip} = S(\mathbf{r}_i, t_p)$, total relative sea-level change at $\mathbf{r}_I$ by time t_p

$I_{ip} = L_i(\mathbf{r}_i, t_p)$, total thickness of ice removed at $\mathbf{r}_i$ by time t_p

$\delta S_{ip} = \delta S(\mathbf{r}_i, t_p)$, increment of seawater thickness at $\mathbf{r}_i$ for time $t_p = S_{ip} - S_{i(p-1)}$

$\delta I_{ip} = \delta L_p(\mathbf{r}_i)$, increment of ice thickness at $\mathbf{r}_i$ for time t_p

$G^{\mathrm{E}}_{ij} = \int_{E_j} \int G^{\mathrm{E}}(\mathbf{r}-\mathbf{r}^1)\, d^2r^1$, the elastic response at $\mathbf{r}_i$ due to the jth finite element.

$G^{\mathrm{H,V}}_{ip\,lj} = \int_{E_j} \int G^{\mathrm{H,V}}(\mathbf{r}-\mathbf{r}^1, t_p - t_l)\, d^2r^1$, the viscous reponse at $\mathbf{r}_i$ for time t_p due to Heaviside loading of the jth element at time t_l.

2.3 NUMERICAL SOLUTION OF THE DISCRETIZED SEA-LEVEL EQUATION

The output from equation (9) is S_{ip} and the inputs to the equation consist of the I_{ip} and the interaction matrices G^{E}_{ij} and $G^{\mathrm{H,V}}_{ip\,lj}$. The first step in the solution of (9) involves calculation of the interaction matrices. In general the response at the centroid of the ith element due to loading of the jth element depends not only on the separation $\mathbf{r}_i - \mathbf{r}_j$ but also on the shape of the elements. In order to reduce the costs of computation we have suppressed the shape dependence and so have effectively replaced each finite element by a circular disc of equivalent area in the calculation of the G^{E}_{ij} and $G^{\mathrm{H,V}}_{ip\,lj}$. The computation speed is further increased by computing the individual elements of these matrices using the method of interpolation in a sparse table of interaction strengths computed for discs with a range of radii and at a range of source point fieldpoint separations. Our table contains 10 different disc radii and the response at 19 different angular separations from the disc centre. The method employed to do the individual disc integrations is described in detail in Wu & Peltier (1982), where it is employed in a discussion of the response to disc load approximations to the main Pleistocene ice sheets.

Given the interaction matrices computed in this fashion and a deglaciation history I_{ip}, equation (9) is solved for each consecutive time from the onset of deglaciation. Normal runs proceed for 20 time steps, that is simulate a real time interval of 20 000 yr. At each time we make a first guess to the unknown S_{ip} as

$$S^1_{ip} = -\rho_{\mathrm{I}} \frac{E_j I_{jp}}{(\rho_{\mathrm{W}} A_{\mathrm{o}})} \tag{10}$$

that is we try a solution which corresponds to the eustatic water rise. When this is substituted into (9) we obtain a residual amount S^{R}_{ip} by which the equation fails to be satisfied at each point in space. The first guess (10) is corrected by this residual amount to produce a second guess

$$S^2_{ip} = S^1_{ip} + S^{\mathrm{R}}_{ip} \tag{11}$$

and the process continued until a converged solution is obtained. In practice three or four such iterations are normally sufficient.

2.4 THE GRAVITATIONALLY SELF-CONSISTENT ISOSTATIC RESPONSE

For reasons which will become obvious in the next subsection it is desirable to know how the meltwater will be distributed over the ocean basins after infinite time has elapsed. The function $S(\mathbf{r}, \infty)$ may be determined from a modified version of (6). Consider the third and fourth terms on the right-hand side in the limit $t \to \infty (p \to \infty)$. Expansion of the fourth term gives

$$\rho_w \int_o \int d^2r^1 \, [\delta s_1(\mathbf{r}^1)\, G^{H,V}(\mathbf{r}-\mathbf{r}^1, t-t_1) + \delta S_2(\mathbf{r}^1)\, G^{H,V}(\mathbf{r}-\mathbf{r}^1, t-t_2) + \ldots$$

$$+ \delta S_\infty(\mathbf{r}^1)\, G^{H,V}(\mathbf{r}-\mathbf{r}^1, t-t_\infty)].$$

Since $t-t_l \to \infty$ as $t \to \infty$, all of the $G^{H,V}(\mathbf{r}-\mathbf{r}^1, t-t_l)$ can be replaced by $G^{H,V}(\mathbf{r}-\mathbf{r}^1, t_\infty)$ and factored out of the square bracket. The above expression therefore reduces to

$$\rho_w \iint_o d^2r^1 \, [G^{H,V}(\mathbf{r}-\mathbf{r}^1, t_\infty)\, S(\mathbf{r}^1, t_\infty)]$$

where we have used the fact that as $t \to \infty$

$$S(\mathbf{r}^1, t) \to \sum_{l=0}^{\infty} \delta S_l(\mathbf{r}^1)\, H(t-t_l) \to \sum_{l=0}^{\infty} \delta S_l(\mathbf{r}^1).$$

The third term in equation (6) can be simplified likewise so that in the limit of infinite time the complete equation becomes

$$S(\mathbf{r}, t_\infty) = \int_I \int \rho_I L_I(\mathbf{r}^1, t_\infty)\, G^H(\mathbf{r}-\mathbf{r}^1, t_\infty)\, d^2r^1 + \int_o \int \rho_w S(\mathbf{r}^1, t_\infty)\, G^H(\mathbf{r}-\mathbf{r}^1, t_\infty)\, d^2r^1$$

$$- \frac{\rho_I}{\rho_w A_o} \iint_I L_I(\mathbf{r}^1, t_\infty)\, d^2r^1 - \frac{1}{A_o} \left[\int_I \int \rho_I L_I(\mathbf{r}^1, t_\infty)\, G^H(\mathbf{r}-\mathbf{r}^1, t_\infty)\, d^2r^1 \right.$$

$$\left. + \int_o \int \rho_w S(\mathbf{r}^1, t_\infty)\, G^H(\mathbf{r}-\mathbf{r}^1, t_\infty)\, d^2r^1 \right]. \tag{12}$$

Here $G^H(\mathbf{r}, t_\infty) = G^E(\mathbf{r}) + G^{H,V}(\mathbf{r}, t_\infty)$ is the Heaviside viscoelastic Green's function for the infinite time response (see Wu & Peltier 1982). We note that (12) is similar to (9) except that it does not contain a temporal convolution. The discrete version of (12) is

$$S_{i\infty} = \rho_w G^H_{ij} S_{j\infty} + \rho_I G^H_{ij} I_{j\infty} - \frac{\rho_I}{\rho_w A_o} E_j I_{j\infty} - \frac{E_k}{A_o} (\rho_w G^H_{kj} S_{j\infty} + \rho_I G^H_{kj} I_{j\infty}) \tag{13}$$

where

$$G^H_{ij} = \int_{E_j} \int \{G^E(\mathbf{r}_i-\mathbf{r}^1) + G^{H,V}[(\mathbf{r}_i-\mathbf{r}^1), t_\infty]\}\, d^2r^1.$$

Equation (13) may be solved by the same relaxation method employed to solve (9) but the number of iterations required is normally 4 rather than 3.

2.5 RSL AND FREE AIR GRAVITY COMPUTATIONS FOR 'PASSIVE' OBSERVATION POINTS

In the preceding four subsections we have described the theoretical calculations which we perform in order to determine the history of relative sea-level at the centroid of each of the finite elements into which the surface of the oceans is divided. These RSL histories are not directly useful for comparison with observations because most of the sea-level data come from coastal regions. Given the S_{ip} obtained by solving (4) we can make accurate computations of the RSL history expected at any coastal site from which data are available. The product $\rho_w S(\mathbf{r}_i, t)$ is the surface mass density variation on the ith oceanic element and together with the input $L_I(\mathbf{r}_i, t)$ provides a complete history of the surface loading produced by deglaciation. Equation (6) can now be solved directly to compute the RSL history at any point $\mathbf{r}$ due to the known loading histories of the grid elements with centroids at $\mathbf{r}_i^1$.

The free air gravity anomaly can likewise be calculated at any point on the Earth's surface and at any time by convolving the same global history of surface loading with a Green's function for the free air signal. The Green's function is (e.g. see Peltier 1974)

$$G^H = G^E + G^{H,V} = \frac{g}{M_e} \sum_{n=0}^{\infty} [n - 2h_n^H(t) - (n+1)\, k_n^H(t)]\, P_n(\cos\theta) \tag{14}$$

in which h_n^H and k_n^H are the Heaviside forms of the surface load Love numbers for the viscoelastic earth model. The equation for the free air signal is

$$\begin{aligned}\Delta g^1(\mathbf{r}, t) = &\int_I \int \rho_I L_I(\mathbf{r}^1, t)\, G^E(\mathbf{r}-\mathbf{r}^1)\, d^2 r^1 + \int_o \int \rho_w S(\mathbf{r}^1, t)\, G^E(\mathbf{r}-\mathbf{r}^1)\, d^2 r^1 \\ &+ \rho_I \int_I \int \sum_{l=0}^{P} \delta L_l(\mathbf{r}^1)\, G^{H,V}(\mathbf{r}-\mathbf{r}^1, t-t_l)\, d^2 r^1 \\ &+ \rho_w \int_o \int \sum_{l=0}^{P} \delta S_l(\mathbf{r}^1)\, G^{H,V}(\mathbf{r}-\mathbf{r}^1, t-t_l)\, d^2 r^1 \end{aligned} \tag{15}$$

the signal Δg^1 computed from (15) is not in fact the signal which is observed since it obtains a maximum value in the isostatic equilibrium state which obtains in the limit of infinite time. If isostatic equilibrium prevails before deglaciation begins and all the ice was melted by t_∞, then the initial gravity anomaly simply equals $-\Delta g^1(\mathbf{r}, t_\infty)$ and the gravity anomaly at any time t thereafter is simply given by

$$\Delta g(\mathbf{r}, t) = \Delta g^1(\mathbf{r}, t) - \Delta g^1(\mathbf{r}, t_\infty). \tag{16}$$

We note from (16) that knowledge of the load distribution at $t = \infty$ and knowledge of the infinite time Green's functions are necessary for computation of observed gravity anomalies. The load distribution at infinite time may be computed in the manner discussed above and calculation of the infinite time Green's functions is discussed in detail in Wu & Peltier (1982).

2.6 LIMITATIONS OF THE FINITE ELEMENT CALCULATION

Of the several limitations of the calculation described above, perhaps the most important physically is that imposed by the assumption that isostatic equilibrium prevails initially. To the extent that this assumption is correct, we may predict RSL histories and free air gravity anomalies from a knowledge only of the history of load removal. Because of the important implications of this assumption we have devoted a separate section of this paper to an assessment of its validity. This assessment will be found in Section 6.

A far less serious assumption in the calculations to be discussed here is that the ocean basins have vertical lateral boundaries. It follows from this assumption that the surface area of the oceans cannot increase by continental inundation as the melting event proceeds. In reality, of course, this does occur so that the actual sea-level rise in the global ocean will be slightly overestimated in our calculations. This effect, however, is extremely small and completely negligible compared to other sources of error in the calculations.

One such important source of error is that produced by the rather coarse temporal discretization of the sea-level equation which we have been obliged to employ in our calculations. This discretization introduces a certain ambiguity of interpretation, as may be seen by consideration of the discretization of the deglaciation history $L_I(t)$. For example, suppose that

$$L_I(t_0) = \delta L_0$$

$$L_I(t_1) = \delta L_0 + \delta L_1$$

$$L_I(t_n) = \sum_{l=1}^{n} \delta L_l. \tag{17}$$

With the coarse sampling interval of $\Delta t = 10^3$ yr there is clearly a limit on the accuracy with which we can approximate a given unloading event. If significant deglaciation were to take place on a time-scale much less than Δt it might not be well described by the piecewise discontinuous unloading history. This problem is not too severe, however, since the last deglaciation event took place on a time-scale of many thousand years (Peltier & Andrews 1976).

More important is the spatial discretization. As mentioned previously we have employed 236 finite elements to define the ice sheets and 470 finite elements for the ocean basins. Since the ice grids are $5^\circ \times 5^\circ$ in areal extent there will clearly be a problem of spatial resolution in some, perhaps crucial, geographical locations. For example, over Nova Scotia and Prince Edward Island on the east coast of Canada we have only a single finite element and the actual deglaciation history of this region was almost certainly more complex than a single element can possibly represent. A second problem with the spatial discretization is that which arises because the finite elements are represented by equivalent circular discs. A consequence of this is that there are inevitably points in the oceans at which two discs overlap and others which are covered by no finite element at all. These problems with the spatial discretization may be minimized in general so long as one is aware of their existence. A final problem with the spatial discretization occurs as a consequence of the fact that the continental coastlines may not be well represented by them. Although this problem has been to a large extent alleviated by employing a relatively fine discretization of the ocean basins along the continental margins it has not been removed entirely. If a site where raised or drowned beaches are observed happens not to be on the edge of the ocean grid element as it should, but rather further landward of the edge, then the effect of crustal tilting by the offshore water load will be emphasized. On the other hand, if the site lies oceanward of the effective coast then this effect will not appear. In order to investigate the magnitude of such effects

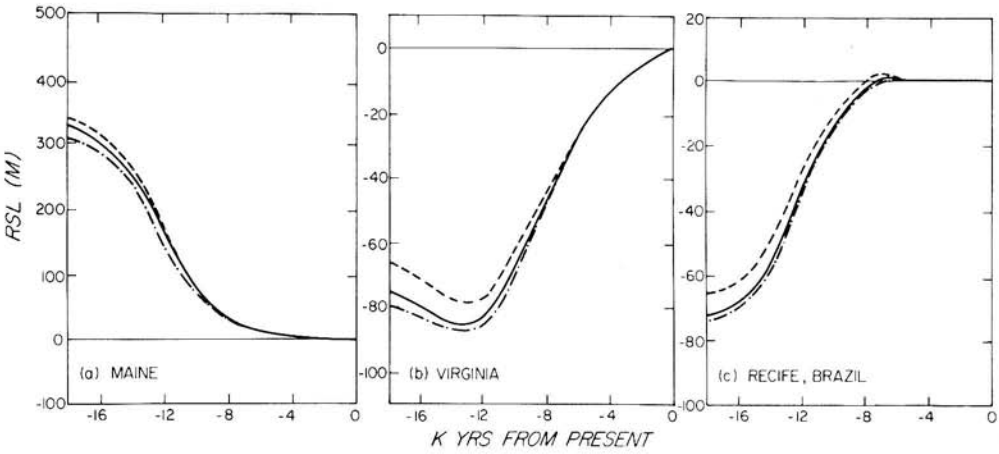

Figure 3. Comparison of RSL curves for three locations that traverse each of the locations at (a) Maine, (b) Virginia and (c) Recife, Brazil. The solid lines are the RSL curves at the site, the dotted lines are for the site lying 100 km inland and the dash-dot line is for the site lying 100 km into the ocean.

we show in Fig. 3 $S(\mathbf{r}_i, t)$ data for coastal Maine and Virginia of the United States and for Recife, Brazil. At each of these locations we have computed a sequence of three relative sea-level curves at sites ranging from 100 km inland to 100 km (10°) into the adjacent ocean. These calculations are for a representative melting history and a representative mantle viscosity profile which need not concern us here. The largest effects of mislocation are seen to occur at sites in the far field of the ice sheets like Recife, Brazil which shows higher raised beaches as one goes further inland but no raised beaches as one goes further offshore. For sites in the near field of the ice sheets like Virginia, the effect of moving inland is to reduce the depth of the drowned beaches. For sites immediately adjacent to the edge of the ice sheet like Maine, inland sites are closer to the ice sheet centre and the effect is thus to increase the height predicted for raised beaches.

Although the results shown in Fig. 3 are for a wide range of distances δ from the effective coast with $-100\,\text{km} \leqslant \delta \leqslant 100\,\text{km}$, the actual uncertainty in the location rarely exceeds this limit. Therefore the uncertainty due to discretization for sites near the edge (or centre) of the ice sheet is extremely small. For sites beyond the ice margin and also in the far field the errors due to spatial discretization are also small for times less than 8×10^3 yr before present (8 KBP). For times of order 18 KBP the error may exceed 5 m but this too is small compared to uncertainties in the data for beaches of that age.

2.7 APPROXIMATE AND GRAVITATIONALLY SELF-CONSISTENT RSL CALCULATIONS

At the beginning of Section 2.1 we asserted that the meltwater which entered the ocean basins as the ice sheets disintegrated could not enter eustatically because this would result in a global ocean with a non-equipotential surface. We furthermore claimed implicitly that this effect was important to the accurate prediction of RSL variations and derived a complicated integral equation formulation of the adjustment problem which included it correctly. The question remains as to how large the error would be in RSL predictions made on the basis of the assumption that the oceans were loaded eustatically. This question has not previously been addressed. In Fig. 4(a, b, c, d) we provide direct numerical comparisons between the

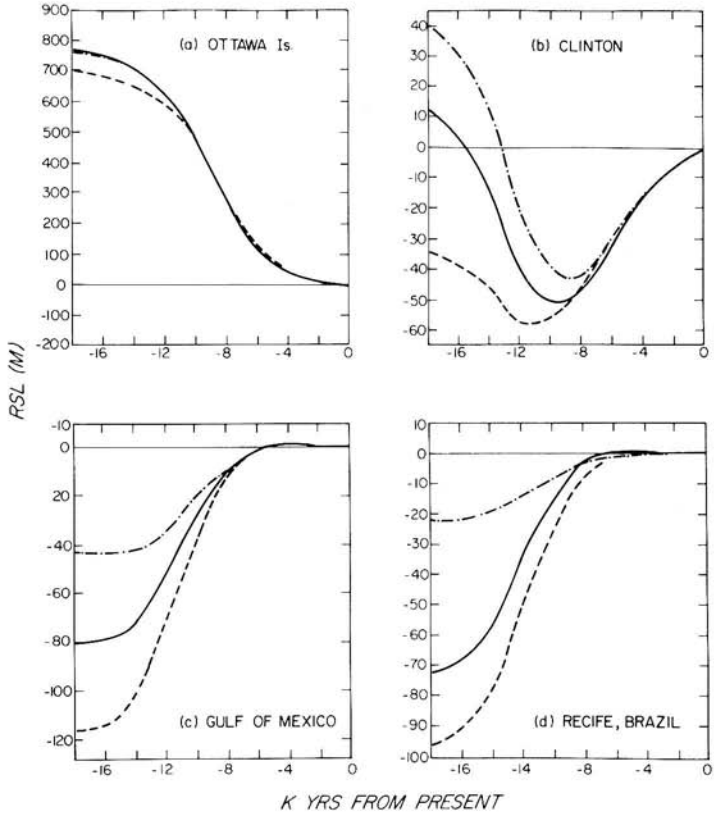

Figure 4. Comparison of sea-level curves computed using the gravitationally self-consistent equations (solid line) and that assuming eustatic rise in sea-level (dotted line). The dash-dot line is the negative of the radial response $R(r, t)$ as given in equation (18).

gravitationally self-consistent RSL calculation (solid curves) and those computed on the basis of the assumption of eustatic water rise (dashed curves). The approximations are compared as suggested in Peltier (1980) from

$$S^1(\mathbf{r}, t) = S_{\mathrm{EUS}}(t) - R(\mathbf{r}, t) \tag{18}$$

where

$$S_{\mathrm{EUS}}(t) = \frac{-M_{\mathrm{I}}(t)}{\rho_{\mathrm{w}} A_{\mathrm{o}}}$$

and

$$R(\mathbf{r}, t) = \rho_{\mathrm{I}} L_{\mathrm{I}} *_{\mathrm{I}} U + \rho_{\mathrm{w}} S_{\mathrm{EUS}} *_{\mathrm{o}} U$$

in which U is the viscoelastic Green's function for radial displacement. It is clear by inspection of these comparisons that the errors are really significant only for times earlier than about 7 kBP at near field sites. At far field sites like Recife, Brazil, however, the errors are extremely large. If data from these sites are to be employed to constrain earth models then the full computation must be employed to predict them.

3 Inputs to the isostatic adjustment model

As discussed in the last section, we require two distinct inputs in order to perform the isostatic adjustment calculations. These consist of a set of Green's functions for the surface mass load boundary value problem, imbedded in which is the unknown viscosity profile of the planetary mantle, and a deglaciation chronology. We will discuss these two inputs in turn.

3.1 VISCOELASTIC GREEN'S FUNCTIONS

The surface load Green's functions are determined entirely by the elastic and viscous structure of the earth model. For the purposes of this paper the earth models will be assumed spherically symmetric with elastic structures identical to model 1066B of Gilbert & Dziewonski (1975). They will differ from one another only in their viscosity profiles, a few of which are displayed in Fig. 5. Model 1 has a uniform viscosity mantle of 10^{22} poise while models 2, 3, 4 and 5 have lower mantle viscosities of 10^{23}, 5×10^{23}, 3×10^{22} and 7×10^{22} poise respectively. Model 6 has a 100 km 10^{21} poise low viscosity zone, and a 10^{23} poise lower mantle. All models have a 120 km thick lithosphere and this is important in so far as the isostatic response is concerned as discussed in Wu & Peltier (1982). The theory for the construction of viscoelastic Green's functions was developed in Peltier (1974, 1976) and extended in Wu & Peltier (1982).

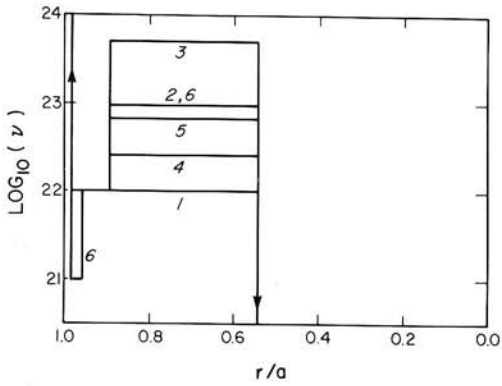

Figure 5. Viscosity profile for models L1, L2, L3, L4, L5 and L6.

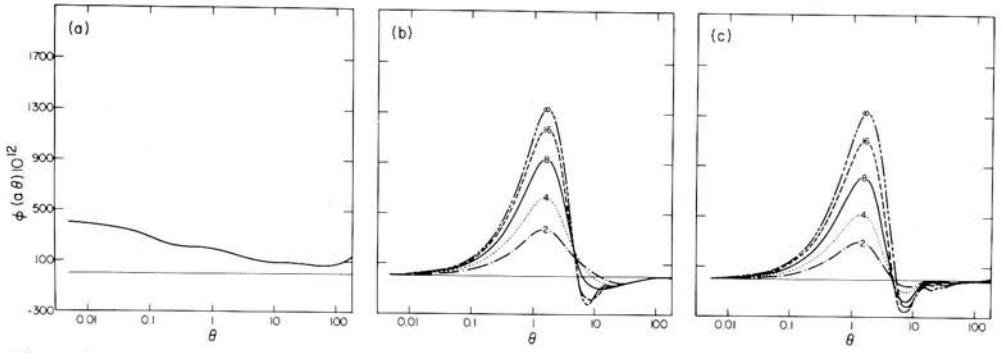

Figure 6. (a) Elastic part of the potential perturbation Green's function. Viscous part of the Heaviside potential perturbation Green's function for model L1 is shown in (b), and for model L2 is shown in (c). These Green's functions have been normalized by $a\theta\times10^{12}$.

Examples of the potential perturbation Green's function which are required in the sea-level equation (6) are shown in Fig. 6. Fig. 6(a) illustrates the elastic part of the potential perturbation Green's function while parts (b) and (c) of Fig. 6 respectively show the viscous part of the Heaviside Green's functions for viscosity models 1 and 2. Each of these response functions has been multiplied by $a\theta$ to remove the geometric singularity at $\theta = 0$ for plotting purposes. Comparison of Figs 6(b) and 6(c) shows that the difference between the two viscous Green's functions is most marked in the region of the forebulge outside the depression at small θ. The model with uniform mantle viscosity (model 1) shows an inward migrating trough which increases in width whereas for models with high lower mantle viscosity (model 2), the trough shows no substantial inward migration and little change of width with time. This fact was first pointed out in Peltier (1974) based upon analysis of radial displacement Green's functions for a similar pair of models. We expect this feature of the Green's functions to be manifested most clearly in the relative sea-level curves from sites near the edge of the ice sheet and that it will prove a useful diagnostic characteristic of the viscosity of the deep mantle.

Another feature of these response functions which turns out to be rather important physically is that they are highly localized, that is, as one moves away from the load the amplitude of the response decreases rapidly. This characteristic of the point load response means that for RSL sites inside the ice sheets the amplitude of the emergence will be mainly controlled by the local ice thickness and deglaciation chronology. As discussed in more detail below, we have exploited this characteristic of the response functions in a computationally interactive manner to refine our first guesses to the melting histories.

3.2 DEGLACIATION HISTORIES OF THE WÜRM–WISCONSIN ICE SHEETS

The second input which is required for the sea-level equation (6) is the history of surface deglaciation. Unless we can construct a reasonably accurate first guess to this function we will not be able to proceed with the calculation. In fact Quaternary geological information does exist which allows such a first guess reconstruction of the melting histories. Information on the total amount of ice residing on the continents at any given time may be obtained by examining the submergence curves from sites sufficiently distant from the glaciation centres. At such sites the vertical motion of the solid earth does not contribute significantly to the RSL history so that these histories may be averaged to obtain a first guess to $S_{\mathrm{EUS}}(t)$. From $S_{\mathrm{EUS}}(t)$ we may obtain $M_{\mathrm{I}}(t)$, using (18) and the known area of the ocean basins A_{o} and the density of water ρ_{w}. Observation of submerged beaches in the far field shows that the eustatic rise was about 80–100 m over the last 18 kyr since glacial maximum, with the time of most rapid ice sheet disintegration centred on about 10 kBP (Shepard 1963).

Although the far field submergence data nicely constrain the total ice volume as a function of time they provide no information on the spatial distribution at each time. This is clear from (8) which expresses $S_{\mathrm{EUS}}(t)$ as a spatial integral. In order to determine $L_{\mathrm{I}}(\mathbf{r}^1, t)$, which is the integrand in this expression, we have to invoke additional information. The necessary observations are provided by end morain data on the basis of which disintegration isochrones for the major ice sheets may be constructed. These isochrones show the location of the ice margin as a function of time during the disintegration history. An example of such information is shown in Fig. 7 which is adapated from Bryson *et al.* (1969). This is for the Laurentide disintegration and shows the location of the ice margin at times given in thousands of radiocarbon years before present on each contour. From this map and similar information from Fennoscandia one may compute the surface area of the major ice

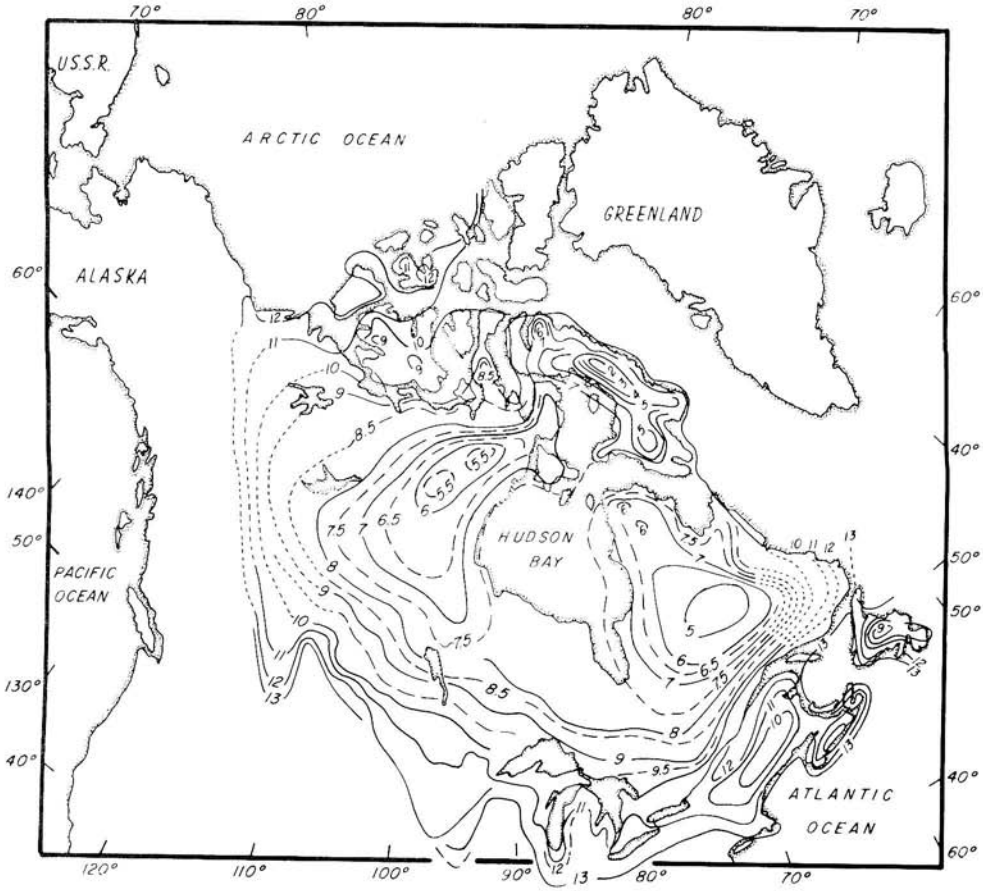

Figure 7. Isochrone map showing the retreat of the Laurentide ice sheet. Contours are in thousands of radiocarbon years BP (adapted from Bryson *et al.* 1969).

sheets as a function of time. The time-dependent ice mass $M_I(t)$ obtained from $S_{EUS}(t)$ is then partitioned among the major ice sheets in proportion to their instantaneous areas.

The question remains then as to how the known ice masses are to be distributed within the known ice sheet boundaries. As a first approximation one may postulate a distribution which gives ice sheet profiles which are in accord with those predicted by steady state ice mechanics (e.g. Paterson 1972). Based on these three distinct types of information, Peltier & Andrews (1976) constructed disintegration histories for the Laurentide and Fennoscandian ice sheets to produce a global model which they called ICE-1. In Fig. 8 we show three time slices through their Laurentide and Fennoscandia deglaciation histories for 18, 12 and 8 kBP.

It should be quite clear from the manner in which it was constructed that ICE-1 is to be considered a first approximation to the actual global history of deglaciation. It is in fact a property of the problem of glacial isostasy that both of the inputs which are required for the theoretical model embodied in equation (6) are imperfectly known. The viscoelastic Green's functions are imperfectly known mainly because the mantle viscosity profile is imperfectly known. The ice sheet melting histories are imperfectly known because the geological data which constrain them are not unambiguously invertible. By fitting the theoretical model embodied in (6) to the geophysical data to be discussed in the next

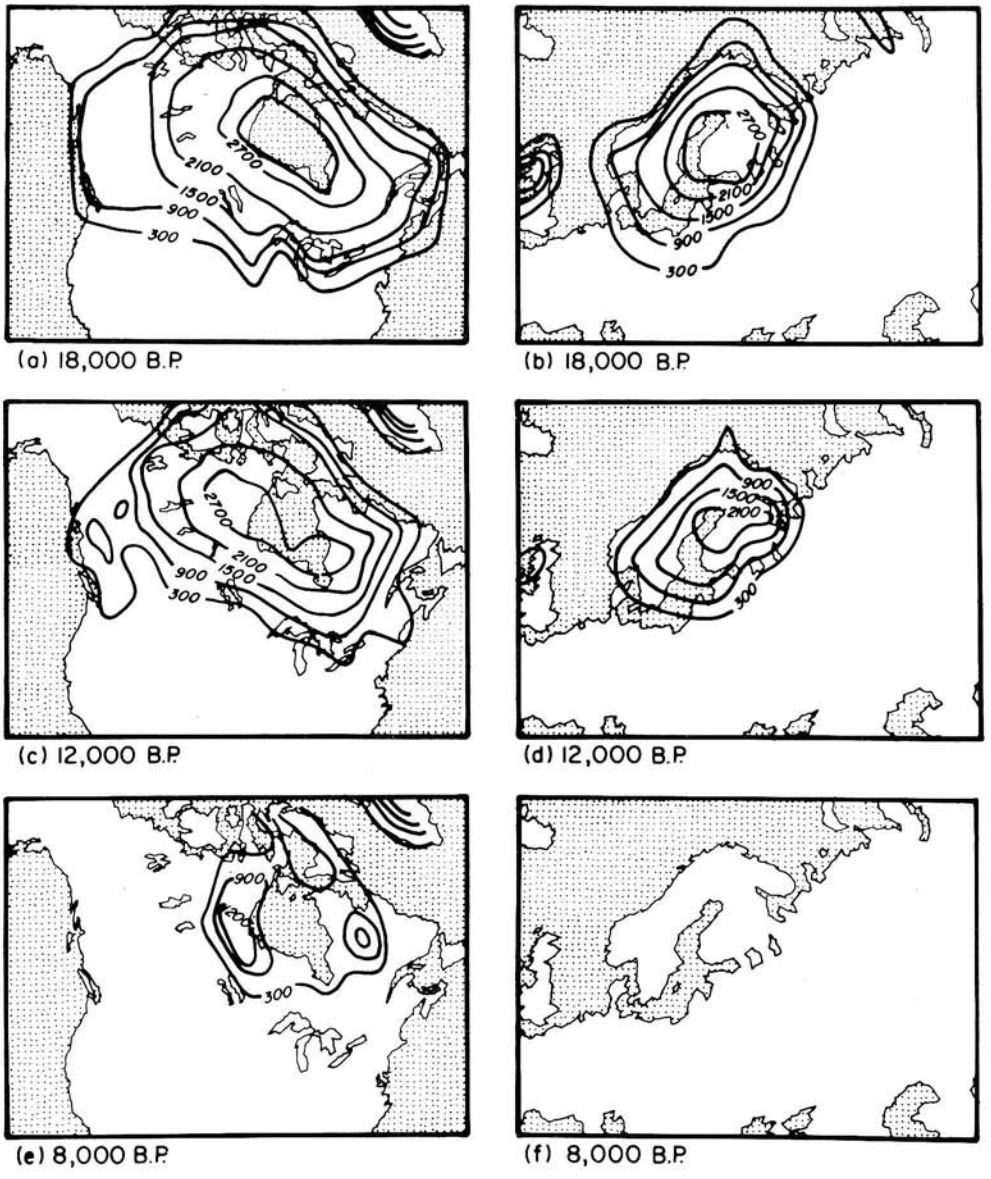

Figure 8. Three time slices through the ICE-1 model. Contours are ice thickness in metres.

section we hope to determine both a more accurate model of the deglaciation history *and* a good approximation to the viscosity profile of the Earth's mantle. The problem is in every way analogous to the problem of employing the observed free oscillation frequencies of the Earth to invert both for the elastic structure of the planet and for the moment tensor of the earthquake responsible for exciting a given set of such oscillations (Gilbert & Dziewonski 1975). As a problem in the theory of inference the isostatic adjustment problem is non-linear because the solution of the forward problem essentially involves a convolution of two unknown functionals. It is our ability to obtain an initial linearization of this inverse problem by making a good *a priori* first guess to the deglaciation history which makes it possible for us to proceed with the analysis (Peltier 1976). This analysis must proceed

iteratively. We first fix the ice history and find an appropriate viscosity profile. We next fix the viscosity profile and refine the ice history. We then fix the ice history and further refine the viscosity profile, etc., continuing until (as we hope!) the process converges. Considered in these terms, the analysis to be presented in this paper will for the most part be concerned with the second two steps in this iterative procedure. We consider that the analysis in Peltier & Andrews (1976) constitutes a successful completion of step 1 since it established that the combination of the ICE-1 melting history and a uniform mantle viscosity profile (with $\nu \cong 10^{22}$ poise) provided an acceptable fit to much of the RSL data. Although Peltier & Andrews (1976) employed the approximate model embodied in equation (18) the comparisons shown in Fig. 4 show that their inference based upon this model will not be significantly affected at near field sites by effects due to the non-eustatic rise of sea-level which actually occurs. Calculations described in Clark *et al.* (1978) and Peltier *et al.* (1978) using the gravitationally self-consistent model embodied in equation (6) and the uniform mantle viscosity profile (for a model with no lithosphere) show that the same model is also capable of fitting far field data if some adjustment of the melting history is introduced.

One difficulty of proceeding to solve a non-linear inverse problem in the manner outlined above is that solutions which are not linearly close to the first guess may be missed entirely. This problem turns out to be of some relevance because there are a few data which suggest that the ICE-1 load history may be significantly in error. An analysis of this question is presented in Section 7 in an attempt to determine how serious a problem this might be. Before discussing these numerical results we shall present an overview of the two types of observational data which our analysis will be concerned to interpret.

4 The observational data base

The two types of data which we will employ here to constrain the ice sheet melting histories and mantle viscosity profile consist of relative sea-level (RSL) histories and free air gravity maps. It is extremely important to note that these two types of information are complementary rather than redundant for at least two reasons. In the first instance it should be quiter clear that RSL data constitute a direct measure of the amount of vertical adjustment which has occurred over some *past* time interval. The free air gravity anomaly, on the other hand, provides an instantaneous measure of the amount of vertical motion which will take place in the *future* as isostatic equilibrium is eventually restored. Given the fact mentioned in the Introduction and discussed at length in Wu & Peltier (1982), that the relaxation spectrum for a single spatial harmonic of the deformation contains several significant relaxation times, this complementary nature of the RSL and free air gravity data becomes particularly important. Relative sea-level will be most sensitive to the shortest relaxation time components of the spectrum whereas the free air gravity signal will be more sensitive to the longest relaxation time components (Peltier 1976; Peltier *et al.* 1978). The second reason for the complementary nature of these two types of observation concerns the fact that they are affected in a strikingly different way by effects due to initial isostatic disequilibrium. This has been demonstrated quite clearly (Wu & Peltier 1982, see figs 22 and 23) and is in the sense that RSL curves are skewed only slighly by such influence whereas the free air signal may be strongly modified.

4.1 THE OBSERVED FREE AIR SIGNALS OVER FENNOSCANDIA AND LAURENTIA

The free air gravity data for North America which will be employed in this paper are those compiled by Walcott (1970, 1972) and redrawn in Fig. 10(a). The map was constructed by

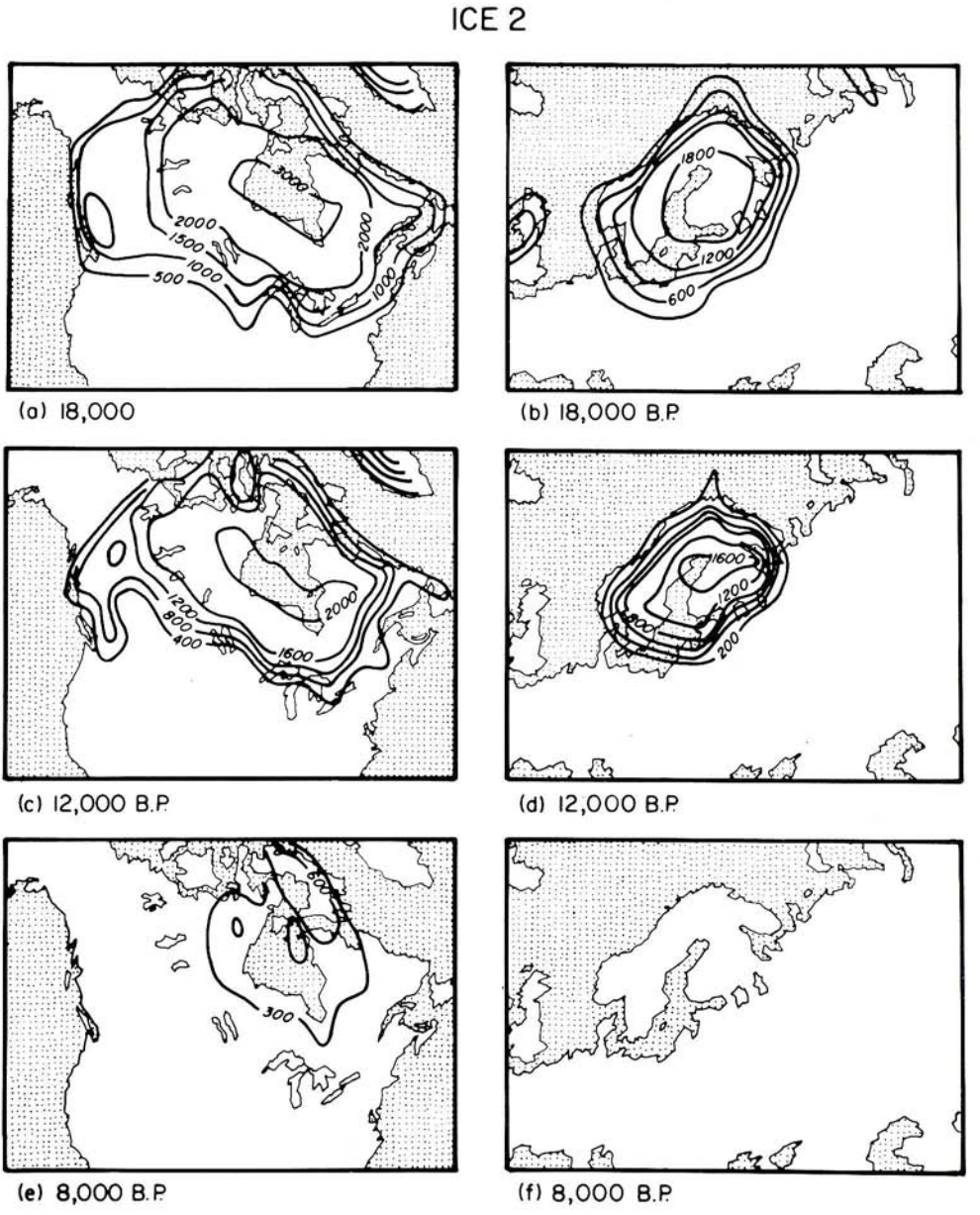

Figure 9. Same as in Fig. 8 except for ICE-2.

averaging the observed free air anomalies in $1° \times 2°$ grid elements. Each of these elements typically contains about 100 observations over land and 40 observations over water (on Hudson Bay). This averaging procedure effectively eliminates any anomaly with wavelength less than 400 km so that influences due to near surface geological structure and surface topography are filtered. Inspection of Fig. 10(a) shows that the major anomalous structure which remains consists of an elongated elliptical trough trending in a north-westerly direction with an amplitude of -26 to -30 mgal for the contour around Hudson Bay. Walcott (1972) has correctly cautioned that since the centre of the bay itself is a Phanerozoic basin, the

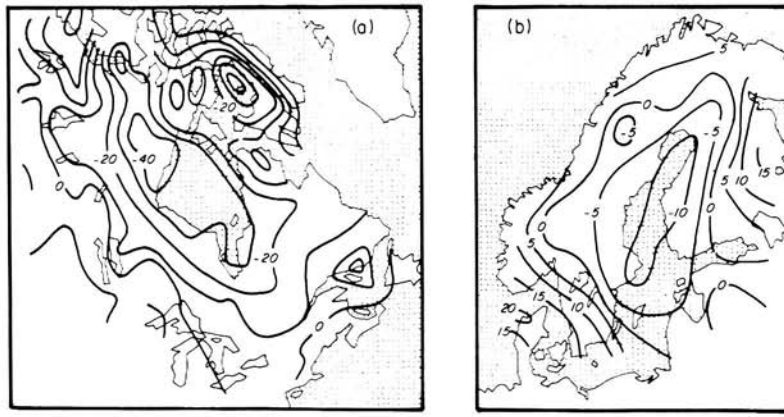

Figure 10. (a) Free air gravity anomaly map in north-eastern Canada (adapted from Walcott 1972). (b) Mean residual gravity anomaly map in Fennoscandia. The anomaly which is correlated to elevation has been removed. Balling (1980) noted that the gravity low correlates with the present rate of land uplift and deduced -15 to -20 mgal over the area of emergence. Contours of both maps are in mgals.

anomaly actually associated with current glacial isostatic disequilibrium could be as much as 10 mgal more negative than that shown in Fig. 10(a). This must be considered something of a speculation, however, and for the most part in what follows we shall accept the observed magnitude of the anomaly as correctly indicative of the extent of current disequilibrium.

As mentioned in the Introduction, the gravity data over Fennoscandia are somewhat more difficult to interpret because of the combined effects of topography and surface geological structure. Balling (1980) has nevertheless managed to obtain the residual gravity anomaly map for this region shown in Fig. 10(b) by removing from the raw gravity anomaly data the portion which is linearly correlated with the surface topography. The map shown in Fig. 10(b) obtained by this least squares reduction has a peak anomaly of about -10 mgal and an anomaly shape which is very well correlated with the pattern of present day emergence. The analysis given in Balling (1980) shows that this anomaly has been biased by +5 to +10 mgal due to bias from features of large spatial scale. He concludes that the anomaly representative of the current degree of isostatic disequilibrium is -15 to -20 mgal in magnitude. This is the anomaly which we will attempt to fit with the isostatic adjustment model.

4.2 THE RELATIVE SEA-LEVEL DATA

The raw RSL data consist of measured elevations and radiocarbon ages of beach materials such as peat, wood or shells taken from specific geographic locations. The relative sea-level curve for each such location consists of a plot of sample elevation versus age for materials taken from that site. Such RSL data for North America have been compiled by Walcott (1972) and by Newman *et al.* (1980). Similar data for Fennoscandia have been compiled by Mörner (1980) and in Bloom (1980).

The original data reproduced in these compilations are for the most part taken from papers published in *Radiocarbon,* the publication of the American Journal of Science which lists the age and other information for samples dated from sites everywhere. These ages are

based upon the earlier accepted value for the half-life of C^{14} of 5570 ± 40 yr, which has since been shown by Godwin (1962) to be in error, the correct half-life being 5730 ± 40 yr. Systematic study of tree ring data, particularly from the bristlecone pine (Stuiver 1971; Suess 1970) has furthermore established that the relation between the true sidereal age T and the published radiocarbon age R between 2500 and 6000 BP can be reasonably well approximated by the relation $T = 1.4R - 900$. For ages greater than 6.5 kBP, however, the actual age is uniformly offset from the radiocarbon age by about 1500 yr with the sidereal age being of course the older.

In all of the RSL compilations mentioned above (e.g. Walcott 1972) these required corrections to the radiocarbon age to give proper sidereal age have not been made so that the error bars attached to the experimental measurements are of limited utility. For the purposes of this paper what we have elected to do to obtain a more realistic presentation of the experimental uncertainty in the data is to represent the RSL data not by the individual plotted points from which each curve is actually constructed but rather by a hatched region within which all of the observational data lie and the width of which in time includes the mapping from radiocarbon to sidereal age. As a result principally of the uncertainty in the age determination for the oldest samples the ability of individual RSL curves to distinguish between various viscosity models will be somewhat reduced. We believe that it is important, however, that the ambiguities of interpretation implied by errors in the observational data be carefully assessed.

For the most part measured sample elevations are taken with respect to a present-day sea-level represented by that at high tide. Of course, not all the emergence/submergence which obtains for a specific age at each site need be produced by glacial isostatic adjustment, other factors may well be involved. Newman *et al.* (1980), for example, believe that sedimentary loading has caused tilting of the continental platform along the US east coast. Bloom (1980) believes that a small part of the observed subsidence around Florida and in Micronesia may be produced by cooling of the oceanic lithosphere. It is quite clear also that other epeirogenic, tectonic and seismic activity may be responsible for vertical displacements along many oceanic coasts (e.g. Japan, west coast of North America, etc.). Unfortunately we usually have no way of estimating the magnitude of these contaminating 'signals' and therefore can make no correction for them in the raw data.

For purposes of discussion in the following section we have generally elected to follow Walcott (1972) in grouping the observational data into one of four geographical bins. Examples of the raw data and our representation of them for sites in each of these four regional categories are shown in Fig. 11. The sites in category 1 are locations which were once ice covered and the RSL curves from them are characterized by continuous emergence. In North America such data are obtained from all of the sites around Hudson Bay, Baffin Island, and the northern Arctic Islands. The sites around Hudson Bay are of special interest because they are near what was the centre of the Laurentide ice sheet. Corresponding locations with respect to the Fennoscandia ice sheet from which good RSL data are available would include sites near Oslo, Norway and from the Angerman River, Sweden.

Sea-level data from sites in category 2 are characterized by initial emergence followed by submergence after about 10 kBP. Such sites are found near the edge of the ice sheets at glacial maximum and the non-monotonic RSL variations which they display may be attributed to the propagation of the peripheral bulge following ice sheet disintegration (Peltier 1974). Representative sites in this category from North America would include Prince Edward Island, Canada, and the eastern coastal states of Maine and Massachusetts of the USA.

Sites in category 3 have RSL curves characterized by continuous submergence and are

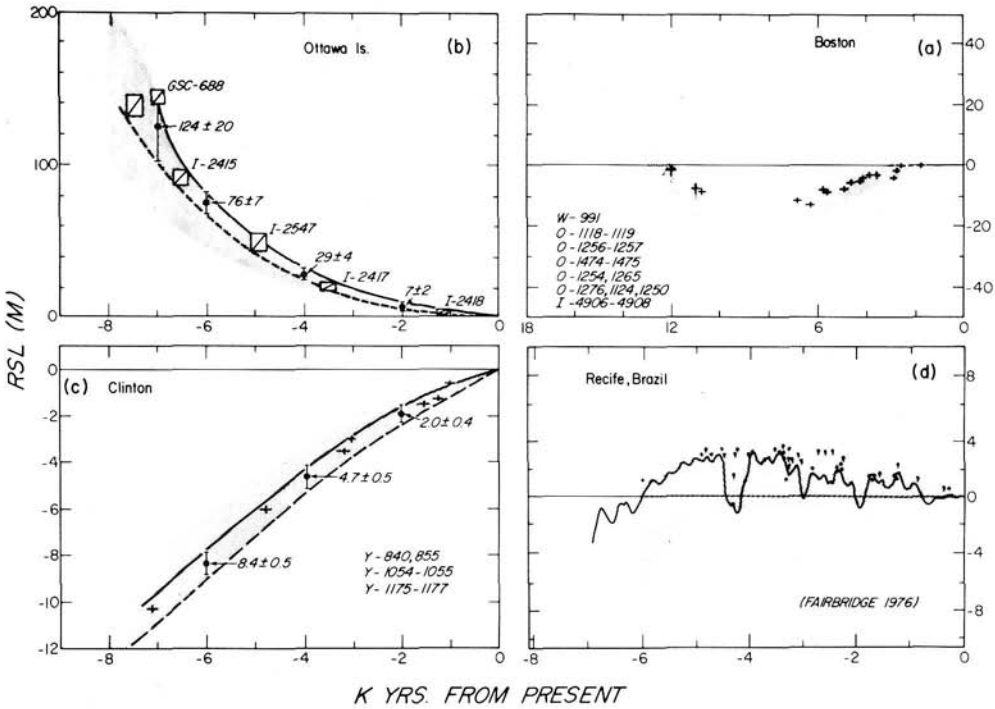

Figure 11. These figures show how the observation of sea-level data are represented in this paper (stippled region). They also show the four categories of sea-level data discussed in Section 4.2.

also found close to the ice sheets. In Europe such data are obtained from sites along the coast of France while in North American all of the sites along the east coast of the USA south of the city of Boston would fall in this category. The sea-level data for the past 4000 yr show that the rate of present-day submergence decreases to the south of New York City through North California to Florida.

The remainder of the RSL data which lie outside the peripheral region of monotonic submergence have been assigned to category 4. The sites in this category come from a geographical area of the Earth's surface which is very much greater than that spanned by the first three categories combined and no single RSL signature is characteristic of the data from all sites. Some sites such as Micronesia and the East Caroline Islands show only submergence whereas others show submergence followed by emergence subsequent to 7–5 kBP, with raised beaches appearing at that time which are now a few metres above present-day sea-level (e.g. Brazil, west coast of Africa). The interpretation of these slightly raised beaches has been somewhat controversial in past work on the theory of RSL variations and it has often been debated whether or not the emergence was 'real'. The collection of such sites is sufficiently diverse, however, including locations such as Recife and Bahia, Brazil, the west coast of Africa, South Island, New Zealand, New Caledonian, North Queensland, Australia, that there can be little present debate that this is a sufficiently widespread observation to demand a general explanation. While Bloom (1980) has attributed the observed emergence at these sites to tectonic activity, it was demonstrated in Clark *et al.* (1978) and Peltier *et al.* (1978) that such features were completely expected consequences of glacial isostatic adjustment. Indeed we might well claim that it is one of the successes of the gravitationally self-consistent model of glacial isostasy developed in Section 2 that it was able to explain this global

characteristic of many of the far field RSL histories. In order to fit these data, however, Clark *et al.* (1978) were obliged to modify the ICE-1 melting history of Peltier & Andrews (1976) by delaying the entire melting event by 2000 yr. As we will show in the following sections, however, there are severe problems encountered if this 'modification' of the ICE-1 history is adopted. We will develop in this paper a somewhat less extreme explanation of this subset of the RSL data in category 4. In the following section we begin our discussion of the numerical results.

5 Free air gravity and RSL constraints on deep mantle viscosity under the assumption that isostatic equilibrium prevails initially

Once a deglaciation chronology and mantle viscosity profile are specified we may employ the theory developed in Section2 to predict the sea-level history which would be observed at any point on the Earth's surface, and the present-day free air gravity anomalies which would exist over deglaciation centres. Since the deglaciation chronology is reasonably well constrained by *a priori* information, we could in principle employ a Monte Carlo approach to explore the range of viscosity profiles which are allowed by the observations or, preferably, the methods of linear inverse theory to converge on a solution which fits the data and to analyse the extent of its uniqueness (Backus & Gilbert 1967, 1968, 1970). Although the basic theoretical ideas which are required to implement the latter analysis have already been developed (Peltier 1976), they have yet to be employed for the simple reason that insufficient experience has yet been obtained with the forward problem to encourage us to believe that we can make a sufficiently accurate 'first guess' to $\nu(r)$ to satisfy the assumptions upon which a successful implementation of formal inverse theory depends.

Our goal in these calculations is therefore more modest. We will for the most part restrict our attention to the investigation of a single family of mantle viscosity profiles which differ from one another only in the magnitude of the viscosity beneath 670 km depth. Our reason for considering such models interesting should be quite clear. It has now been established by direct high pressure petrological investigation (Mao, Bell & Yagi 1979), that the seismic discontinuity at this depth is fully explicable in terms of the structural phase transition from spinel to a more closely packed and therefore more dense mixture of perovskite plus magnesiowustite. As Sammis *et al.* (1977) and others have pointed out, the more dense phase will have a higher creep activation energy than the less dense phase and therefore in the absence of any significant temperature change across the boundary the viscosity should increase from the upper to the lower mantle. Sammis *et al.* (1977) assumed that the temperature change across the boundary was small and adiabatic with a gradient equal to about $0.3^{\circ}\mathrm{C\ km^{-1}}$ and were led to predict a viscosity increase of about 1 order of magnitude (based upon oxygen ion packing systematics). Their assumption is reasonable, however, only if the mantle is convectively well mixed since only then will its interior be adiabatic. Although whole mantle convection is the preferred mode of radial heat transport from most geophysical points of view (Peltier 1980, 1981) recent geochemical evidence based upon the Sm-Nd isotopic system (DePaolo & Wasserburg 1976, 1979; O'Nions, Evensen & Hamilton 1977) has been interpreted as requiring extremely limited exchange of material between the upper and lower mantles. In order to satisfy the constraints of the thermal history, the upper and lower mantles must then be convecting separately and the boundary between them must be a thermal boundary layer across which there is a rather large ($> 500^{\circ}\mathrm{C}$) increase of temperature from upper to lower mantle (e.g. Jeanloz & Richter 1979). Such a temperature increase would be sufficient to overwhelm completely the expected viscosity increase due to the increase of creep activation energy and therefore if the lower and upper mantles are

convecting separately the viscosity of the lower mantle should be lower than that of the upper mantle (Peltier 1981). It should therefore be clear that the magnitude of the observed viscosity change across 670 km depth may be extremely useful in distinguishing which of the proposed models for mantle mixing is actually closer to the truth.

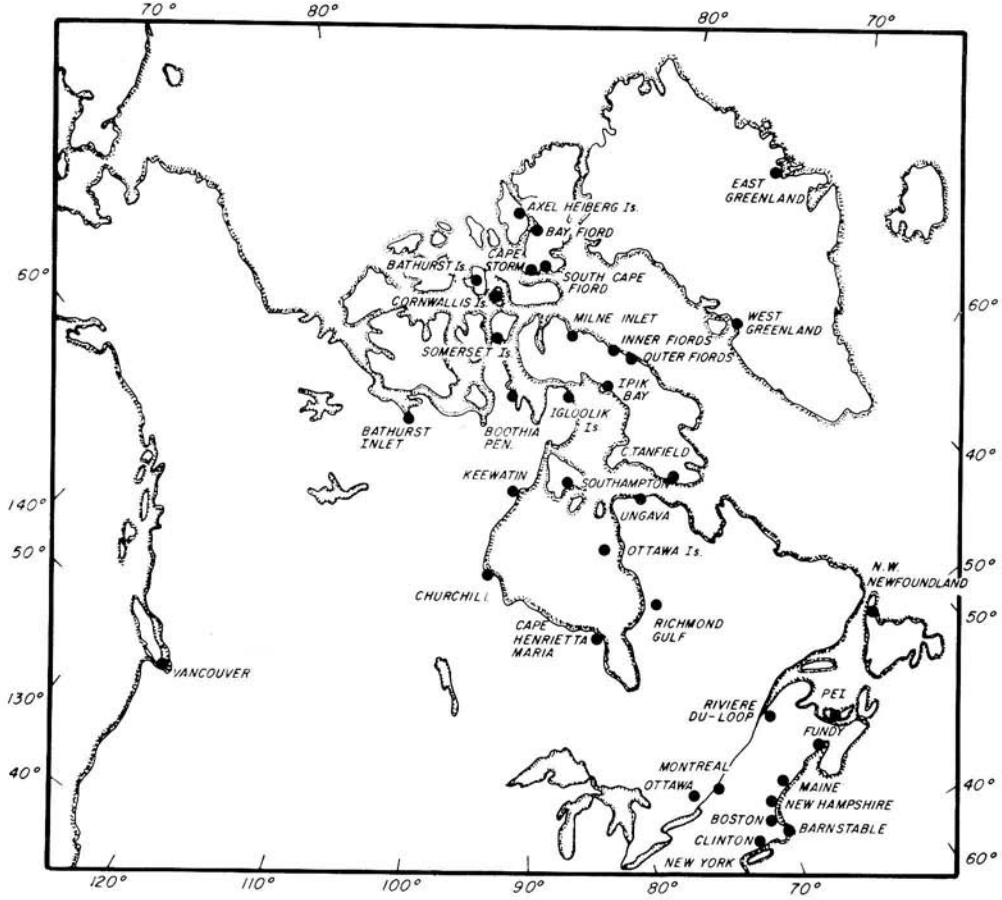

Figure 12. Location map of the sites where sea-level data have been obtained.

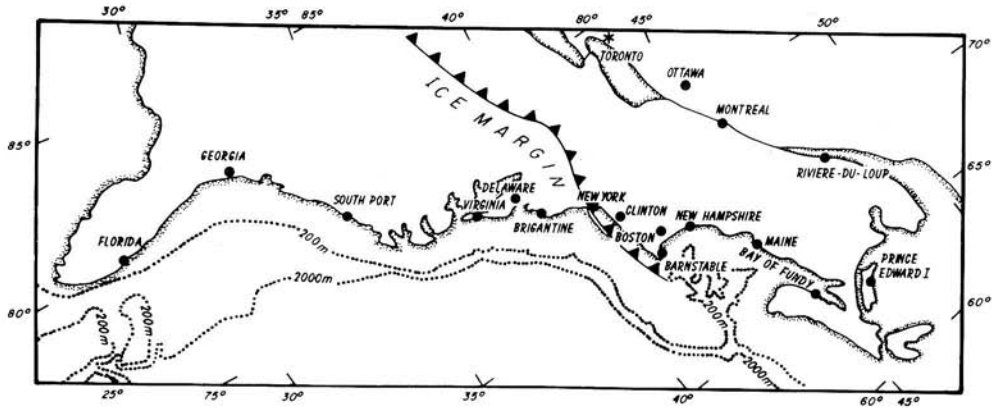

Figure 13. Same as Fig. 12.

The calculations upon which we will base our initial measurement of the required viscosity variation across the boundary are all predicated upon the assumption of initial isostatic equilibrium. We will also employ a deglaciation chronology which is very close to the C^{14} controlled model ICE-1 of Peltier & Andrews (1976). As we will show, however, ICE-1 does have several minor inadequacies and so we will also proceed to refine this model somewhat before employing it to produce a final set of RSL and free air gravity comparisons. This refined deglaciation history will be called ICE-2 and the process we have followed to produce it is discussed in the following subsection and is based in part upon RSL data from the North American sites shown on the location maps in Figs 12 and 13.

5.1 THE INADEQUACIES OF ICE-1

The left-hand plates of Figs 14–19 show comparisons of observed and predicted RSL histories at a subset of the geographical sites from which we have data. These calculations are all based upon the ICE-1 chronology and are shown for three different mantle viscosity models, each of which has a 120 km thick lithosphere and an upper mantle viscosity of 10^{22} poise. The short dashed line, the long dashed line, and the solid line on each of these figures are respectively for models with lower mantle viscosities of 10^{22}, 10^{23} and 5×10^{23} poise. As discussed in the last section, the stippled area on each frame represents the observations. The horizontal lines adjacent to the right-hand edge of each frame shows the RSL variation which will have obtained after infinite elapsed time and it will be observed that the net RSL change since the start of deglaciation is independent of the viscosity model (Peltier 1976). It should also be noted that these comparisons differ from the similar preliminary analysis contained in Peltier & Andrews (1976) in three respects: (i) the viscosity models employed here all have lithospheres whereas those used by Peltier & Andrews did not, (ii) in Peltier & Andrews the boundary between the upper and lower mantle was nominally placed at 10^3 km depth, whereas here it is at the seismically constrained depth 670 km, (iii) the calculations of RSL in Peltier & Andrews were not gravitationally self-consistent.

Inspection of the left-hand plates in Figs 14–19 shows that there are systematic differences between observation and theoretical prediction at most sites, including locations well within the ice sheet margin and those in the far field. Some of these deviations are clearly associated with errors in the ice history while others may be due to errors in the mantle viscosity profile. Until we have removed all of the errors which are obviously due to errors in the deglaciation model we will not be able to make clear inferences concerning the viscosity profile. In the remainder of the subsection we will discuss the inadequacies of ICE-1 which are revealed by the RSL comparisons.

Three qualitative measures of the goodness of fit of theory and observation turn out to provide useful indications of obvious errors in the deglaciation model: (i) the general shape of the RSL curve, (ii) the height predicted for the oldest beach, (iii) the predicted present-day rate of uplift. Inspection of Figs 14 and 15 shows that none of the viscosity models is able simultaneously to fit the height of the oldest beach and the present-day rate of rebound for sites around Hudson Bay near the centre of rebound. As pointed out in the last section, since melting is complete in ICE-1 by 8 KBP the relaxation curves since that time represent free decay and so have shapes which depend only on the viscosity model. However, their amplitudes are determined mostly by the local ice thickness. Inspection of the RSL information for the Ottawa Islands (Fig. 14) shows the way in which this differential dependence on the ice history and viscosity profile may be exploited to refine ICE-1. At the Ottawa Islands site, for example, the general shape of the relaxation curve is best predicted by the model with lower mantle viscosity of 10^{22} poise. The other two models both predict a

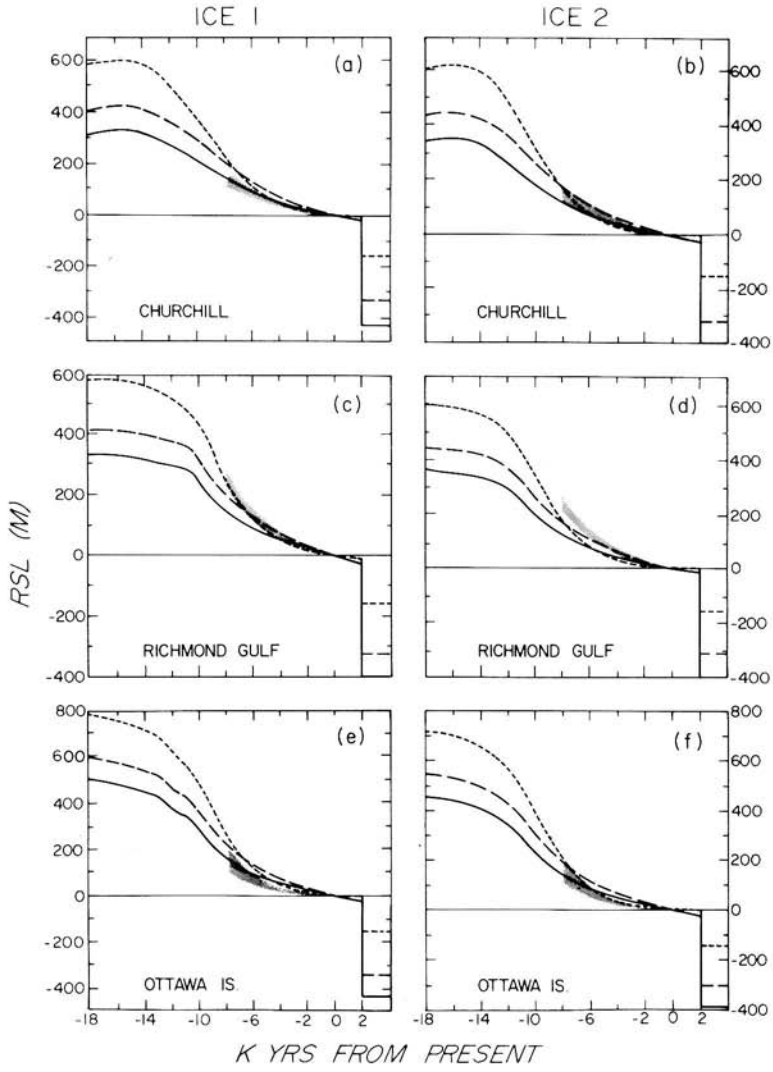

Figure 14. Comparison of RSL curves for three viscosity models. The dotted lines, the long dashed lines and the solid lines are for models with lower mantle viscosities of 10^{22}, 10^{23} and 5×10^{23} poise respectively. The stippled region represents the data. The horizontal lines on the right side of each diagram are the response at infinite time. Diagrams (a), (c), (e) are when the ICE-1 chronology is used, diagrams (b), (d), (f) are when ICE-2 is used.

present-day rate of uplift which is much higher than observed and a free decay relaxation time which is too long. However, the model with the 10^{22} poise lower mantle predicts a height for the oldest beach which is greater than observed which suggests that the ice thickness in this region was somewhat excessive. Using arguments of this sort we may proceed to refine ICE-1 in a computationally interactive fashion.

The theoretical predictions and observations for several sites near the edge of the Laurentian ice sheet are shown in Fig. 15. For NW Newfoundland the data show monotonic emergence whereas the prediction of the model with a lower mantle viscosity of 10^{22} poise is of emergence followed by submergence: the typical signature produced by inward propa-

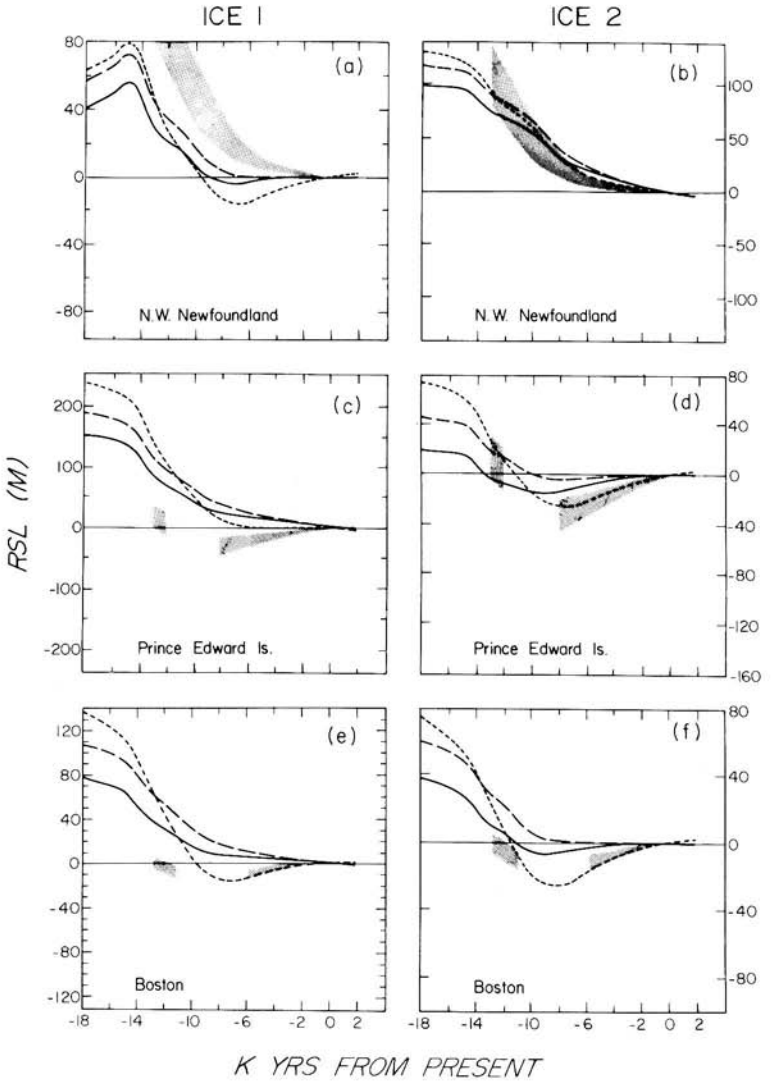

Figure 15. Same as Fig. 14.

gation of the forebulge. Neither of the other viscosity models fit the data better than the uniform one. There is therefore clear evidence of an error in the local ice history and as we shall see in the next subsection the difficulty may be resolved by delaying by 4000 yr the melting of Newfoundland ice. A similar difficulty is evidenced in Fig. 15(c) for Prince Edward Island. The observations clearly indicate submergence during the past 8 kyr whereas each of the viscosity models predicts monotonic emergence during this period of time. The observation of a 12 kBP beach at or above present-day sea-level further indicates that local ice melted much earlier than supposed in ICE-1 – sufficiently so as to allow the peripheral bulge to migrate through this site at about 10 kBP. The data for Boston shown in Fig. 15(e) are reconciled only by the model with uniform mantle viscosity since only this model allows substantial peripheral bulge migration and this predicts the observed emergence followed by submergence. However, it is clear by inspection of this plate that either the predicted ampli-

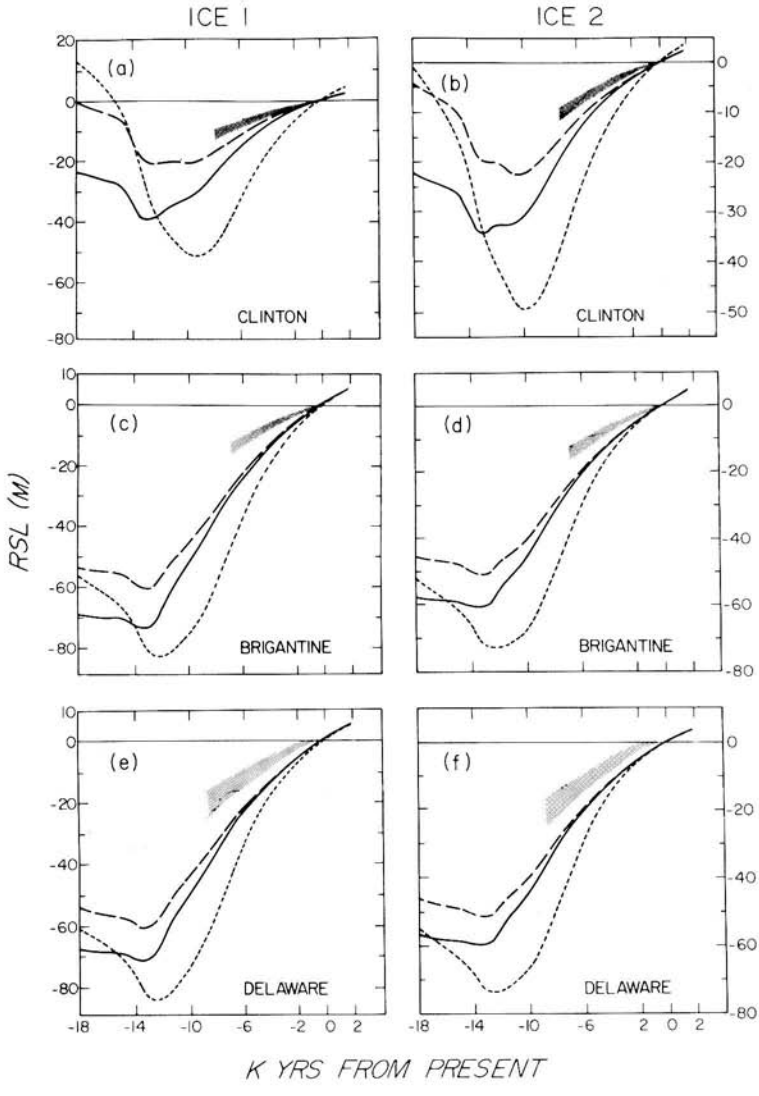

Figure 16. Same as Fig. 14.

tude of the migrating bulge is too small or its time of arrival is late by about 2000 yr. This also indicates that modification of the ice history is required.

At locations further removed from the ice sheet terminus, such as those in Delaware, and at Brigantine, New Jersey and Clinton, Connecticut shown in Fig. 17, there are also certain characteristic misfits between the observations and predictions of the theory. Although all viscosity models predict the same shape of the submergence curve for the past 10 kyr, the predicted amplitude of the submergence curve is strongly dependent upon the deep mantle viscosity. The model with uniform mantle viscosity overpredicts the amount of submergence. As the lower mantle viscosity is increased to 10^{23} poise the misfit is reduced, while further increase to 5×10^{23} poise cause the error to increase again. We will defer further discussion of these discrepancies until the following subsections which deal with the refined deglaciation history.

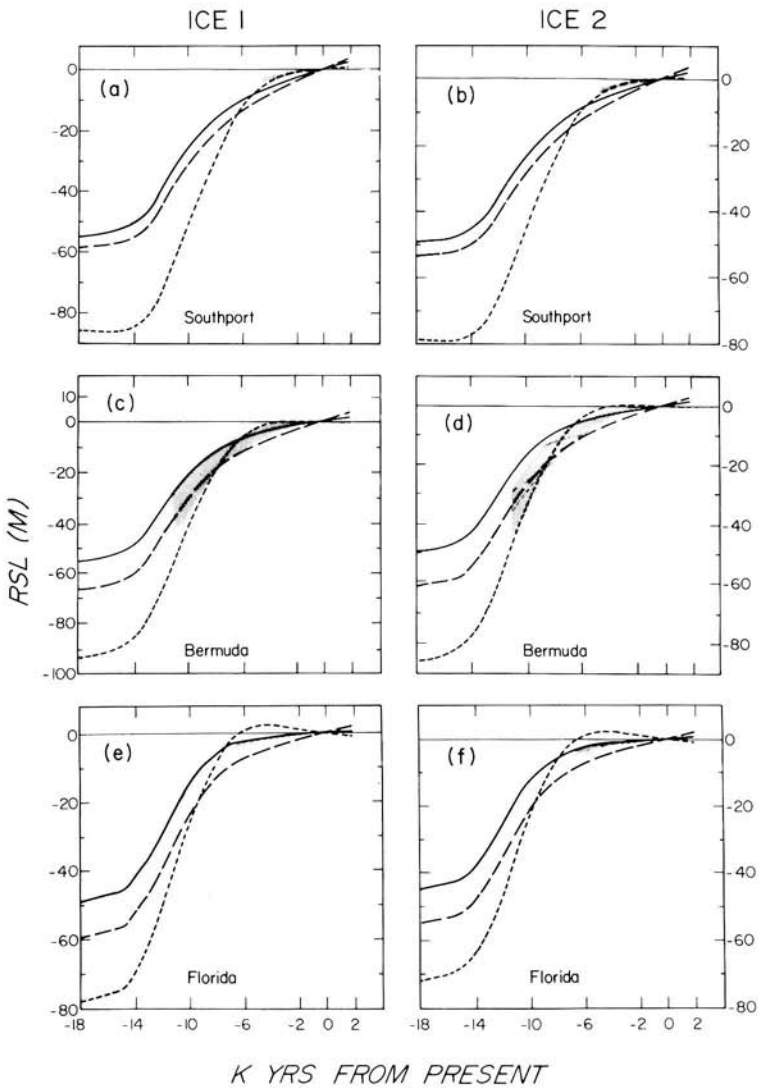

Figure 17. Same as Fig. 14.

Some data from Fennoscandia are shown in Fig. 19 where again the left-hand plates are for the ICE-1 deglaciation history. It will be observed that the uniform viscosity 10^{22} poise model fits the observed uplift histories at the mouth of the Angerman River very well. At this location even the present-day 8–9 mm yr^{-1} rate of uplift is predicted accurately with this viscosity model. At Oslo the uniform model predicts a present-day rate of uplift of 6 mm yr^{-1} which is 2 mm yr^{-1} greater than the observation but the amplitude of the uplift is overestimated.

A sequence of observations from sites in the far field of the ice sheets is shown in Fig. 18. The data from the NW Gulf of Mexico, which is the nearest of the sites shown in this Figure, are particularly important since they extend back to 18 KBP and thus provide some constraint upon the total ice volume of the deglaciation model. We see that the combination of ICE-1 with the uniform 10^{22} poise viscosity model fits the total submergence very well

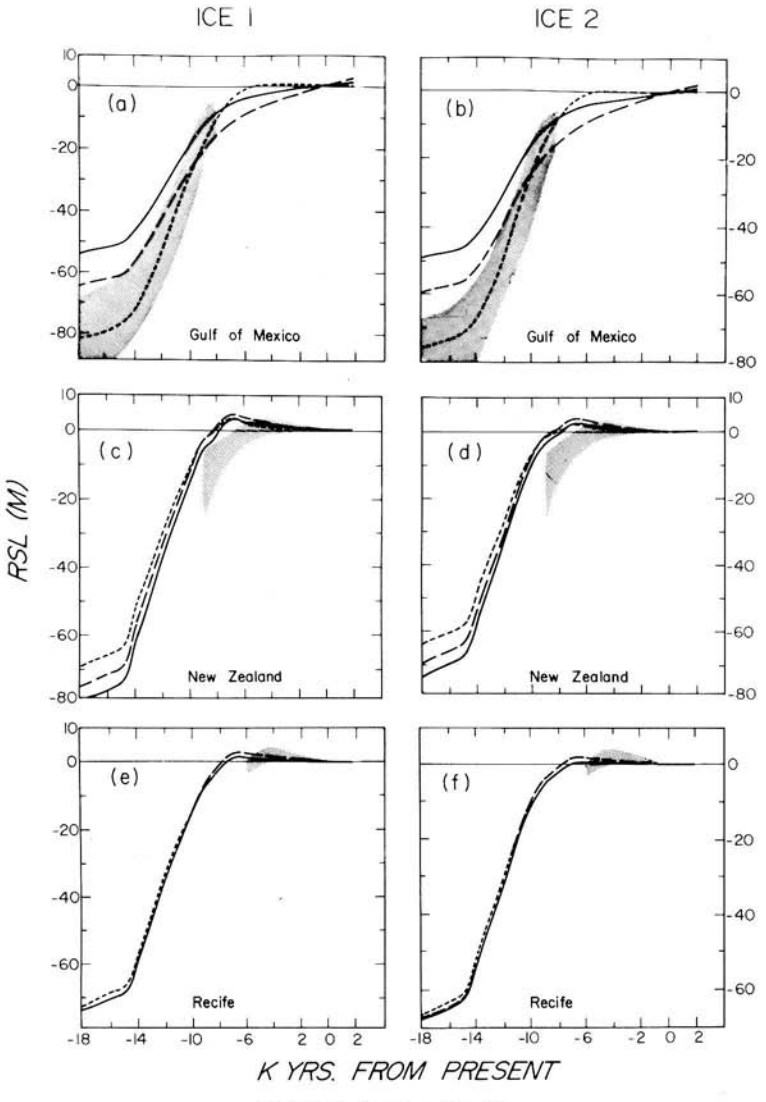

Figure 18. Same as Fig. 14.

whereas both models with high lower mantle viscosity predict too little submergence. The fact that submergence at this site is viscosity model dependent, however, indicates that the data cannot be employed unambiguously to constrain the total ice volume. Inspection of the plates for the two southern hemisphere sites of Recife, Brazil and South Island, New Zealand shows that for such locations the predictions are only weakly dependent on the viscosity model, all of which predict the appearance of a raised beach at about 8 KBP. This is in sharp disagreement with the observations, however, which show that this raised beach actually appears only after 6 KBP. On the basis of this disagreement we might be tempted to conclude that the timing of the entire northern hemisphere deglaciation event has been chosen to be 2000 yr in advance of its actual occurrence. Clark *et al.* (1978) and Peltier *et al.* (1978) actually succumbed to this temptation and showed that such delayed histories could reconcile the far field data. As we will show in Section 7, however, this line of argument leads to the construction of models which cannot simultaneously fit both the RSL and free

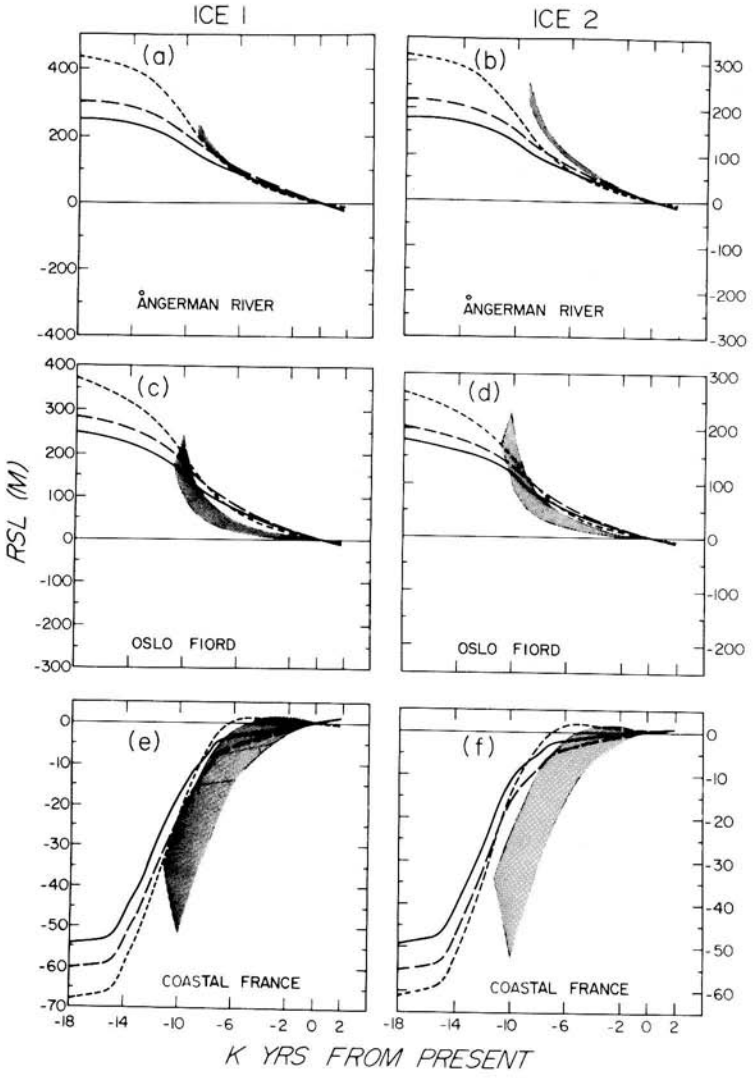

Figure 19. Same as Fig. 14.

air gravity data. Such models also, and very severely, violate the radiocarbon controlled disintegration isochrones of Bryson *et al.* (1969).

Calculated present-day free air anomaly maps for the Laurentian region have already been shown in Peltier (1981) for each of the mantle viscosity models. There it is shown that as the viscosity of the lower mantle is increased from 10^{22} to 10^{23} and 5×10^{23} poise the peak free air anomalies over Hudson Bay are respectively -28, -56 and -72 mgal. These maps, which were computed on the basis of the assumption of initial isostatic equilibrium, demonstrate quite clearly that realistic viscoelastic models of the planet require *no* substantial increase of viscosity with depth in order to explain the observed free air signal over the Canadian shield. This is in striking contrast to the conventional view (e.g. Walcott 1980 and previously cited references). Comparison of our predicted anomalies with Walcott's (1972) observations show that even the model with the 10^{23} poise lower mantle is strongly rejected if ICE-1 is a reasonable approximation to the actual deglaciation chronology since the

observed anomaly is between −30 and −40 mgal. As we will show in the next section, where the effect of initial isostatic equilibrium is discussed, some increase of lower mantle viscosity (by about a factor of 3) is nevertheless required to fit the observation.

The situation in Fennoscandia is also very similar to that in Laurentia. As will be shown in Section 6, the gravity anomalies computed from the instantaneous removal of a parabolic load with size and thickness comparable to the Fennoscandian ice sheet have peak free air anomalies of −19, −37 and −46 mgal for models with lower mantle viscosities of 10^{22}, 10^{23} and 5×10^{23} poise respectively. Since the observed anomaly in Fennoscandia is about −20 mgal (Balling 1980), we again conclude that models with lower mantle viscosity much greater than 10^{22} poise are strongly rejected. When the effect of disequilibrium is taken into account, we shall see that a small (factor of 2) increase in the lower mantle viscosity is also necessary. Thus the same viscosity model is able to reconcile the observed gravity anomaly over *both* Hudson Bay and the Gulf of Bothnia.

The preceding discussion of RSL predictions made with the ICE-1 deglaciation chronology have revealed several inadequacies of the model. In the following subsection we will describe the process of refinement which we used to produce the improved model which will be called ICE-2.

5.2 THE REFINEMENT OF ICE-1

Given that the uniform mantle viscosity model is quite strongly preferred by both the RSL and gravity data we may proceed to employ the Green's functions for this model to improve the ice history. In principle one could employ standard linear inverse theory to iterate on to a 'best' deglaciation chronology since, as Peltier (1976) has pointed out, the viscoelastic Green's functions are the appropriate Frechet kernels for this problem. Clark (1980) has attempted to employ this method of reconstruction but has obtained rather disappointing results. The difficulty with the method arises because of the magnitude of the required computational effort when one attempts to retrieve best histories of deglaciation for each of the 86 $5^\circ \times 5^\circ$ elements which cover the Laurentian region (say). In order to reduce the problem to manageable size Clark (1980) was obliged to approximate the entire melting history by eight large disc loads. Because of this crude discretization his 'best' deglaciation histories are characterized by wild and aphysical oscillations in time.

We have elected to refine the ICE-1 chronology in a way which, although less elegant in principle, is considerably more effective in practice. What we do is to follow a computationally interactive procedure which consists of continuously altering the ice history to remedy local errors in RSL fits to the predictions of the 10^{22} poise uniform viscosity model and of fits to the free air gravity observations. After each set of alterations we recompute the model predictions and check to ensure that the alterations have produced the desired effect. This manual process works very well because the ICE-1 chronology is in fact a good first guess to the actual load functional. Some of the more significant modifications which this procedure has produced are visible in the maps of ice thickness as a function of time shown in Fig. 9. The new model, called ICE-2, is also tabulated in Appendix A. In this model melting is delayed over Igoolik Island by approximately 2000 yr. There are also substantial changes in NW Newfoundland and near the coast of Labrador where the ice thickness is maintained at about 500 m until its final disappearance at approximately 10 KBP. In addition both Nova Scotia and Prince Edward Island are taken to be free of ice soon after the onset of deglaciation. Aside from these modifications of the ICE-1 model near its terminus, ICE-2 also includes a major realignment of the long axis of the entire elliptical load in order that the predicted free air anomaly trough should more closely match that on Walcott's map

(Fig. 10a). Finally, ICE-2 also includes a 25 per cent reduction in ice thickness over Fennoscandia.

This reduction was based on the conclusion drawn from an earlier erroneous calculation of the gravity anomaly. At the time of that calculation, we were unable to obtain the isostatic response of the Earth accurately. Also in that calculation the effect of water entering the Gulf of Bothnia after deglaciation was not taken care of properly. The first problem has been discussed in Wu & Peltier (1982), and the second problem will be discussed in more detail elsewhere. These problems are of no concern to us here, and as will be shown in this subsection, the reduction in ice thickness results in a smaller amplitude of emergence for sites inside Fennoscandia, and degrades the fit already achieved in the calculation with ICE-1, except at Oslo. This implies that the ice deglaciation history described in ICE-1 better approximates the real situation in central Fennoscandia, but for sites like Oslo a reduction in ice thickness is necessary.

5.3 THE ICE-2 CHRONOLOGY: FREE AIR GRAVITY AND RSL CONSTRAINTS ON DEEP MANTLE VISCOSITY

The new RSL data generated with the ICE-2 chronology is shown in the right-hand plates of Figs 14–19 and on all of the plates in Fig. 20. Inspection of the data from sites which were under the Laurentian ice sheet (Figs 20, 14b, d, f and 15b, d, f) shows that with the slight adjustments in ICE-1 described in the last subsection the new deglaciation chronology fits most of the data very well and the uniform mantle viscosity model is still strongly preferred. When the model with the 10^{23} poise lower mantle is employed the theoretical predictions match the net amount of emergence acceptably but predict a present-day rate of emergence which is excessive. For the model with lower mantle viscosity of 5×10^{23} poise the converse is true. This model is able to fit the present-day rate of emergence but predicts far too little net emergence and is rejected by the data. Exceptions to this generalization can, however, be found and all such exceptional sites apparently lie in the south-west corner of Hudson Bay. For example, at Churchill (Fig. 14b) the amplitude predicted by the 10^{22} poise uniform model can be adjusted to fit the observation but the observed present-day rate of emergence is then found to be low. With the 10^{23} poise lower mantle model the predicted amplitude is also correct but the emergence rate is too high while the model with the 5×10^{23} poise lower mantle fits the uplift rate but misses the amplitude.

At sites near the edge of the ice sheet, ranging from Prince Edward Island to Boston, the model with a uniform mantle viscosity of 10^{22} poise fits the observations very nicely. Two examples are shown in Fig. 15(d, f). From these graphs we also see that models with high viscosity lower mantle are strongly rejected, because the amplitude of submergence is either too small or even completely absent. The fact that models with high viscosity lower mantle are also able to produce some (although small) submergence after emergence requires some explanation. As shown in Fig. 4(b), the RSL curve has two opposing contributions, one is due to the radial displacement response which for models with high viscosity lower mantle produces mostly emergence, and the other contribution is due to the rise in sea-level which produces about 20–30 m of submergence here. The radial response produces mostly emergence because for these viscosity models, the forebulge does not migrate substantially – the model with 10^{23} poise lower mantle can produce less than two degrees of migration in the first 20 kyr, compared with the 5° (or more) of migration for the model with 10^{22} poise uniform mantle in this period of time (Fig. 13b). Thus for the model with the 10^{23} poise lower mantle, the motion of inward migration is detected only at sites within one degree angular distance near Prince Edward Island, and not at Boston. As for the model with

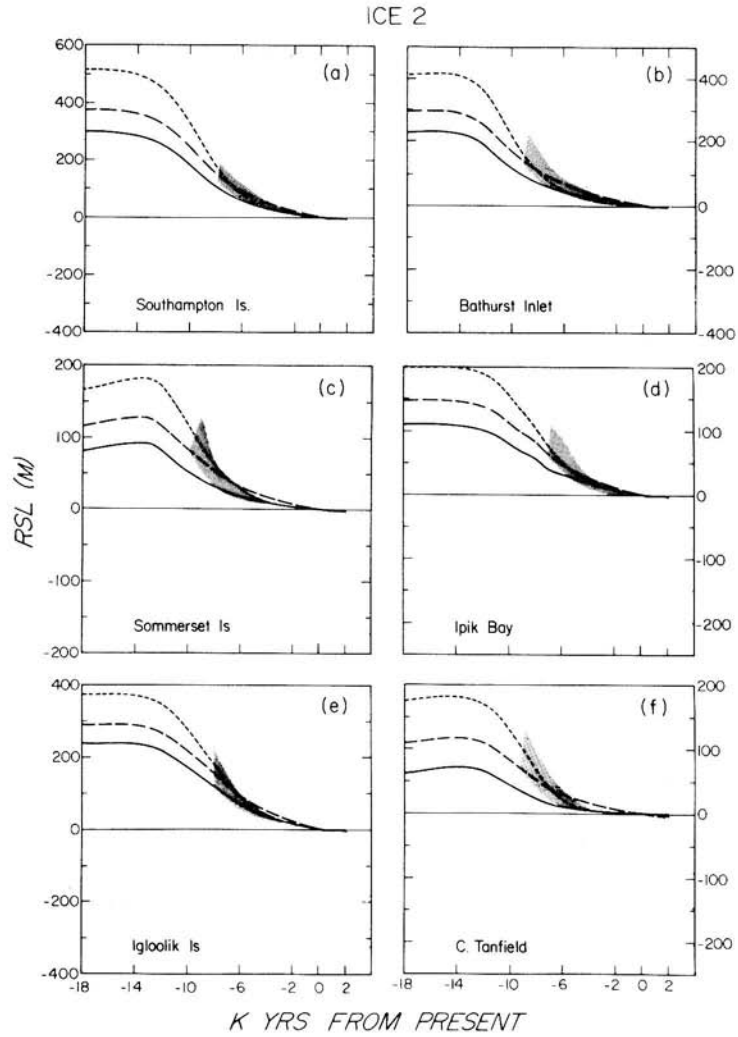

Figure 20. Same as Fig. 14 except ICE-2 is used for all of them.

5×10^{23} poise lower mantle, the submergence at Boston is due predominantly to the effect of rise in sea-level which overwhelms the small amplitude of emergence at that time.

The modification of the ice history does little to remedy the misfits between theory and observation at greater distances from the ice sheet, however. Along the entire east coast of the United States, north of Southport, North Carolina we still find the observed sea-levels to be higher than predicted with the misfits largest for the uniform mantle viscosity model (Figs 16, 17). South of Southport, however, the situation is reversed since sea-levels are lower than those predicted by the uniform viscosity model. Although increasing the viscosity of the lower mantle does reduce these misfits somewhat, there are reasons which we will discuss in the next section why this avenue of argument is unsatisfactory. Closer inspection of the misfits of the uniform 10^{22} poise model with the observations at Georgia, Southport, Norfolk, Delaware, Brigantine and Clinton shows that they increase as one goes north along the coast from Southport. The observation is that the deviation between the observed and predicted submergence of the 6 kyr beach increases linearly to the north as shown in Fig. 21.

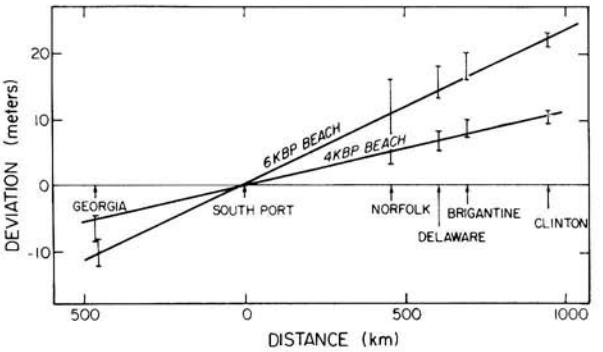

Figure 21. Deviation of the predicted 6 kBP beach, and the 4 kBP beach from the observation data is plotted against distance from Southport. The deviation is shown to be systematic.

Also shown in this figure is the difference between the observed and predicted submergence at 4 kBP which also varies linearly with distance. One possible explanation of the misfits at the sites between Clinton, Connecticut and Georgia for the uniform viscosity model could be that some epeirogenic process has tilted Clinton upwards with respect to Southport by about 2 cm km^{-1} in the last 6000 yr. It is interesting to note that Newman *et al.* (1980) have suggested that offshore sedimentary loading along this coast may be responsible for just this sort of differential vertical motion. We cannot, of course, rule out the possibility that the observed misfits are associated with inadequacies of the earth model such as lithospheric thickness or lateral inhomogeneity. As will be shown elsewhere, the misfits can in fact be explained by an increased lithospheric thickness.

As mentioned previously, the observations at far field sites such as those shown in Fig. 18 are much more sensitive to the deglaciation history than they are to the viscosity model and the fits of these data for ICE-2 are essentially identical to the fits for ICE-1. All viscosity models predict the appearance of a raised beach at 8 kBP rather than at 6 kBP which is observed. Although one might take this as an argument for delaying the entire melting event in time by 2000 yr as assumed in Clark *et al.* (1978) this turns out to be implausible for reasons which will be fully discussed in Section 7 of this paper.

Besides direct comparison of individual observed and predicted RSL curves, we may also distinguish between the different velocity models on the basis of the *global* patterns of relative sea-level variations to which they give rise. This global pattern is described by the field $S(\theta, \varphi, t)$ which is the solution of the sea-level equation (4). In Fig. 22 we show the global $S(\theta, \varphi, t)$ solution for the uniform mantle viscosity model and for four times in the disintegration history: 12, 8, 4 and 0 kBP. Fig. 23 shows the same time sequence for the model which has the 10^{23} poise lower mantle. Inspection of these two figures shows that initially most of the meltwater floods the southern ocean basins. For the model which has uniform mantle viscosity, however, the region of maximum increase of relative sea-level propagates quickly inwards towards the deglaciation centre. The inward migration of this RSL maximum is also accompanied by a collapse of its width. This characteristic behaviour is, of course, a direct reflection of the inward migrating peripheral bulge. For the model with high lower mantle viscosity the RSL increase in the southern oceans initially continues monotonically and there is no substantial migration of the pattern with time. Following the cessation of melting, however, the maximum decreases in amplitude as water floods the neighbouring ocean basins.

Based upon the above described global RSL maps we may divide the surface of the Earth

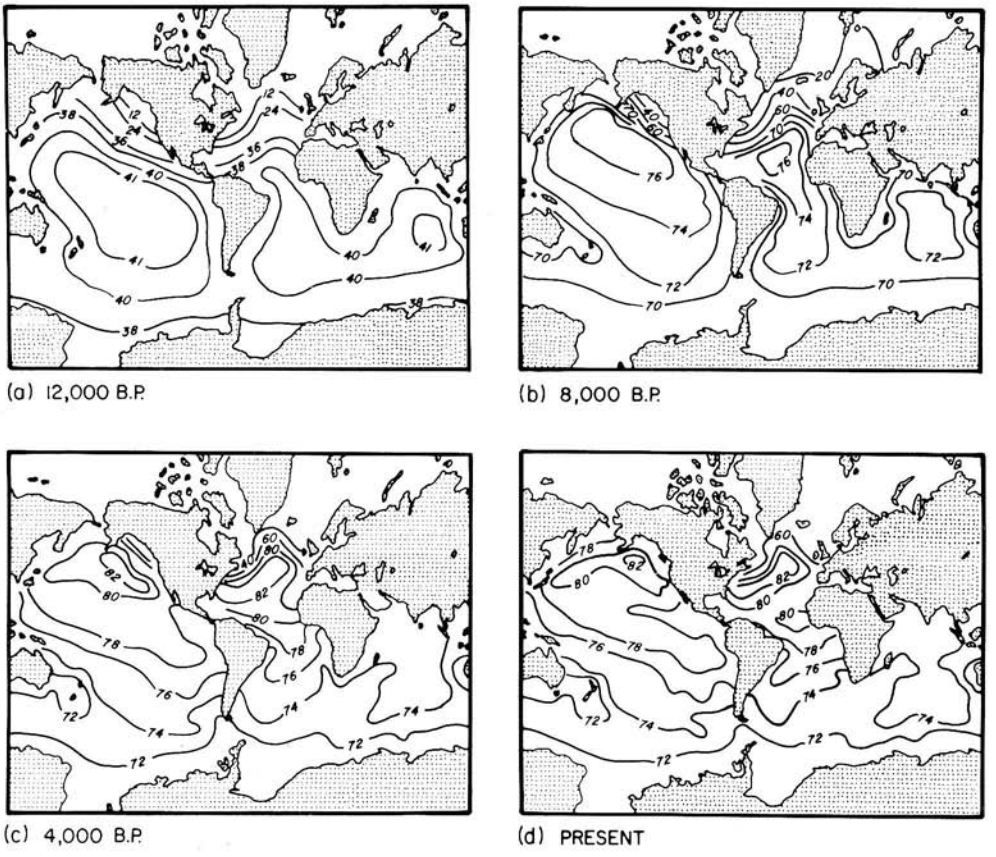

Figure 22. Predicted change in sea-level (metres) since the Late Wisconsin maximum at 18 kBP. The ice chronology is given by ICE-2 and the earth model has 10^{22} poise uniform mantle.

into a number of zones within each of which the RSL signature has a characteristic form. The zone boundaries for the uniform viscosity model and for the model with the 10^{23} poise lower mantle are shown in Figs 24 and 25 respectively. Clark *et al.* (1978) inferred the existence of six such zones in their preliminary study of the sea-level equation using ICE-1 and Green's functions for an earth model with a uniform mantle viscosity of 10^{22} poise and no lithosphere. The difference between their result and that shown in Fig. 24 is therefore due mostly to the presence of the lithosphere. The six zones may be characterized as follows.

Zone I is the region of continuous emergence which was once ice covered and is the same geographically for both viscosity models.

Zone II is characterized by continuous submergence due to the collapse of the peripheral bulge. Inspection of Figs 24 and 25 shows that this region is very much broader for the model with high lower mantle viscosity than it is in the uniform 10^{22} poise case. This difference is completely explicable on the basis of the Green's functions for the two models.

In each model zone III is characterized by delayed emergence following the cessation of melting. The emergence is produced after the RSL maximum migrates past the site so that the timing of this event is near the present for sites that are closer to the deglaciation centres. Fig. 24 shows a much wider zone III than found by Clark *et al.* (1978) and in Fig. 25

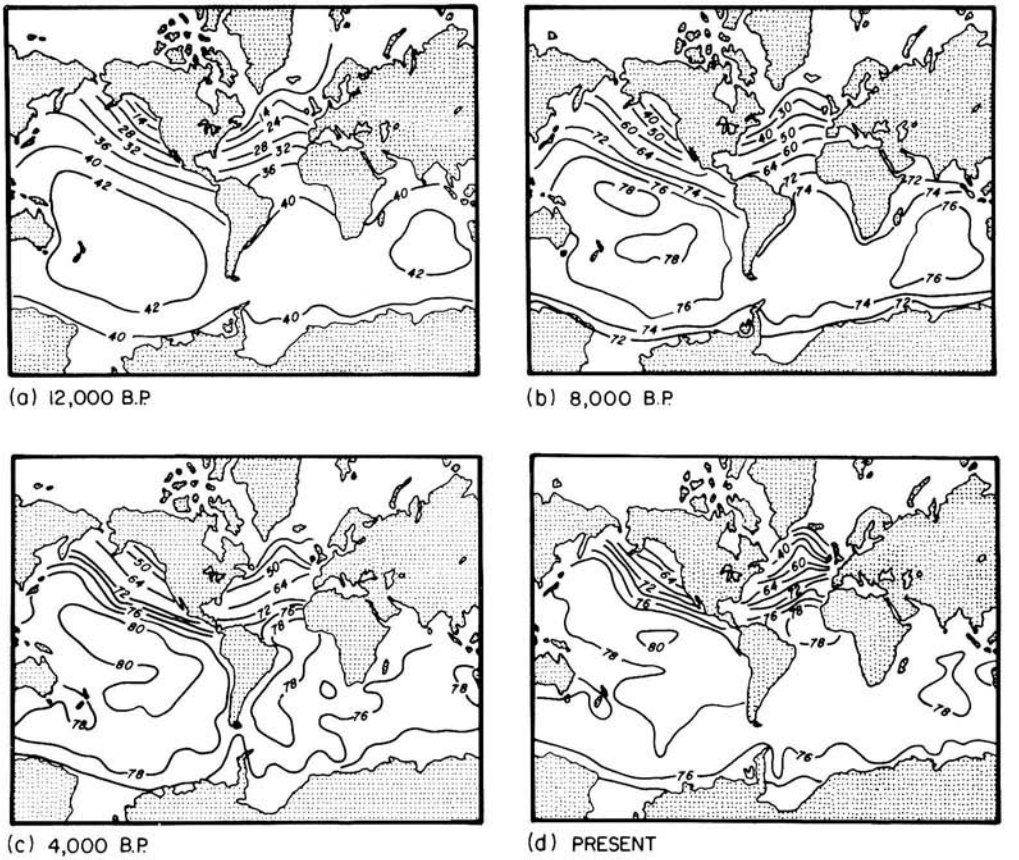

Figure 23. Same as in Fig. 22 except that the earth model has 10^{23} poise lower mantle.

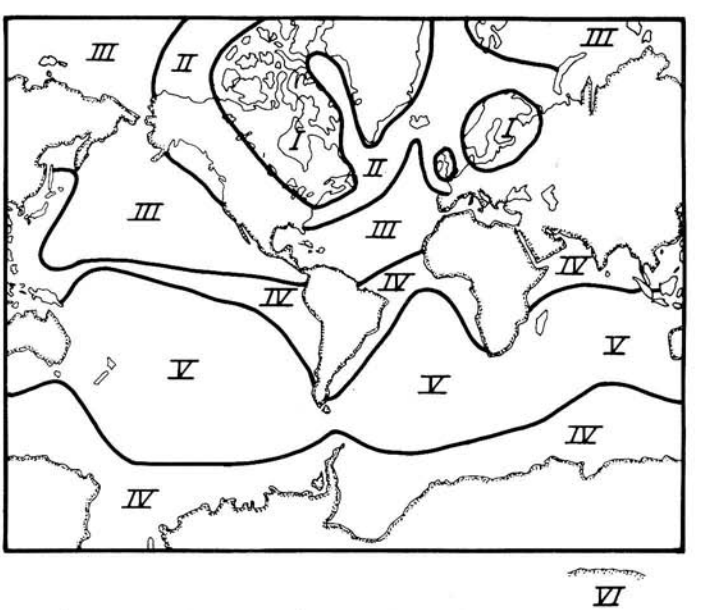

Figure 24. Location of the six sea-level zones for the melting of the ICE-2 chronology. The earth model has 10^{22} poise uniform mantle.

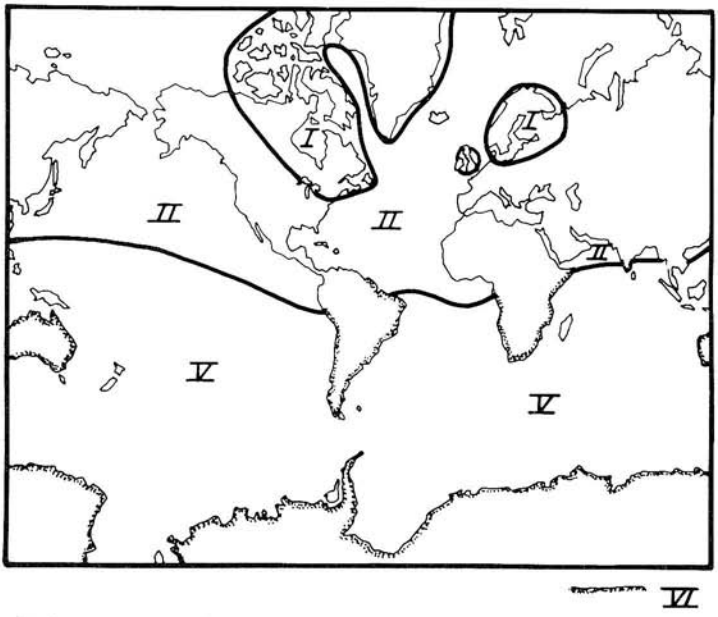

Figure 25. Same as in Fig. 24 except for an earth model with a 10^{23} poise lower mantle.

this region is essentially absent because for the model with high lower mantle viscosity the bulge does not migrate.

Zone IV is a region of continual submergence. In Fig. 24 this consists of two narrow regions north and south of zone V, while in Fig. 25 it is again absent. It is interesting to note that the observed relative sea-level data along the west coast of Africa (Faure 1980) do show just this sort of transition between a region of submergence followed by emergence and then continuous submergence in the vicinity of Dakar, Senegal which is indicated by Fig. 24. No such boundary is found in Fig. 25.

The characteristic signature of the RSL curves in zone V is that emergence occurs immediately upon the cessation of melting. For the high lower mantle viscosity model, zone V occupies most of the southern oceans and the boundary with zone II runs south of the Hawaiian Islands. One might then hope to use the data from this region to distinguish between the different viscosity models, i.e. if the data at Hawaii showed continuous submergence then one might argue that the high lower mantle viscosity was preferred. Unfortunately, these data may be contaminated by vertical movements induced by processes not connected with deglaciation.

Zone VI consists of all continental shorelines which are sufficiently remote from the main deglaciation centres. The RSL variations at sites in this zone are only weakly dependent upon the mantle viscosity profile and are characterized by late emergence forced by the offshore water load (Walcott 1972). It should be pointed out that although the causes of the characteristic sea-level signature in zones III, V and VI are different, the signatures themselves are really quite similar. In practise it is often difficult to assign, based on observational data, a given site unambiguously to one of these zones so that the utility of the classification employed by Clark *et al.* (1978) is rather unclear in so far as far field sites are concerned. The location of far field zone boundaries is therefore not a particularly useful diagnostic for discriminating between viscosity models.

The present-day free air gravity anomalies predicted by the ICE-2 melting history are shown in Fig. 26 for two of the viscosity models which we have been employing and for the

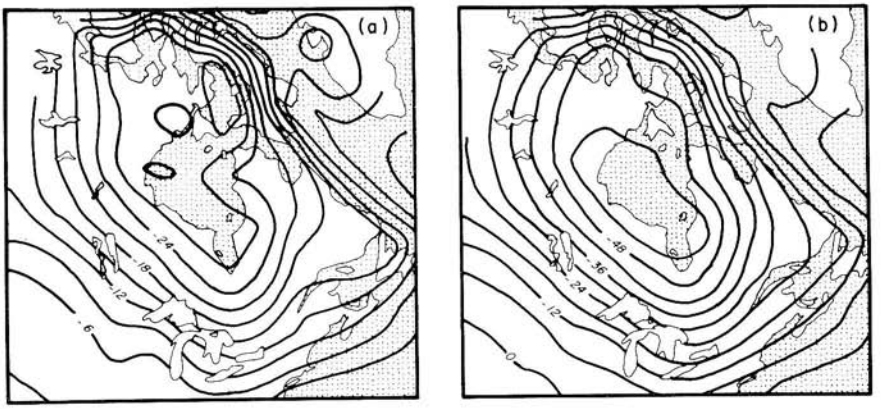

Figure 26. Free air gravity predictions for the Laurentide region when ICE-2 is used. (a) is for the uniform viscosity model, (b) is for model with 10^{23} poise lower mantle.

Laurentian region. (a) is for the uniform 10^{22} poise viscosity model, (b) is for the model with 10^{23} poise lower mantle. Although the peak anomalies for these models are not substantially different from those predicted by ICE-1, the shape and orientation of the anomaly is now much closer to the observed. In addition, the anomalous lows over Eskimo Point and the Foxe Basin are reasonably well fitted by the uniform viscosity model. The $5° \times 5°$ spatial resolution of our calculations does not allow the representation of smaller-scale features than this. One feature of the free air map which is not particularly well fitted by the uniform viscosity model (or either of the others) is the location of the zero anomaly contour separating the interior low from the weak exterior high associated with the peripheral bulge. In Section 7 we will show that this mislocation of the zero anomaly contour may be partly attributed to the effect of initial isostatic disequilibrium.

It is important for the reader to realize the novelty of the result which we have obtained for the free air gravity anomaly. All authors who have considered this problem previously (e.g. Walcott 1972) believed that it was impossible for a model with a uniform mantle viscosity of 10^{22} poise to fit the observed gravity anomaly over Laurentia. We have shown, here and in Peltier (1981), that the contrary is in fact true. The reason why the uniform viscosity model fits this datum is that it supports extra modes of relaxation with long relaxation times due to the internal density discontinuities in the mantle associated with the olivine → spinel and the spinel → perovskite + magnesiowustite phase transitions. The existence of these modes was first pointed out by Peltier (1976). It is because of the presence of these seismically resolved discontinuities that the uniform viscosity model is able to fit both relative sea-level and free air gravity data.

5.4 THE ICE-2 CHRONOLOGY WITH OTHER MANTLE VISCOSITY PROFILES

In the last subsection we saw that in order to reconcile the model with uniform 10^{22} poise mantle viscosity with the submergence data from the east coast of the US we were obliged to invoke the existence of some epeirogenic process (such as sedimentary loading) which has tilted the seaboard with respect to Southport. The question which we will address here is whether it might be possible to explain these data by invoking more complicated viscosity models rather than epeirogeny. To this end we will discuss the prediction of models with lower mantle viscosities of 3×10^{22}, 7×10^{22} and 10^{23} poise. The last of these models also contains a 100 km thick low viscosity channel beneath the lithosphere in which the viscosity

is 10^{21} poise. Our reason for restricting consideration to models with increased viscosity in the lower mantle are two-fold: (i) the previously discussed RSL calculations for east coast sites (Fig. 16) showed that the misfits were minimized for the model with 10^{23} poise lower mantle since both lower (10^{22} poise) and higher (5×10^{23} poise) values increased the error, (ii) a small subset of the RSL data around Hudson Bay (south-west sector) showed a clear preference for some increase in deep mantle viscosity and although the 5×10^{23} poise lower mantle model was excluded by all observations the case against the 10^{23} poise lower mantle model was not always completely clear unless the free air data were invoked. Since there is some latitude for, and even requirement of, an increase in lower mantle viscosity in order to fit the free air anomaly when the effect of initial disequilibrium is included (Section 6) we cannot rule out the possibility of such models on this account. The observation which seems most sensitive to increase of viscosity in the lower mantle is that of peripheral bulge migration at edge sites like Boston, and the Bay of Fundy, Nova Scotia. However, even here we have only shown that models with 10^{23} poise lower mantles are apparently ruled out by the data and we thus have no idea how large an increase is required to fully prevent the observed migration. Our purpose in employing the model with 10^{23} poise lower mantle in conjunction with a shallow low viscosity channel is to investigate the extent to which the undesirable characteristics of the 10^{23} poise model (i.e. non-migrating peripheral bulge) might be mitigated by the latter feature.

Relative sea-level curves for the three new models are shown in Fig. 27 for six Laurentian sites. On these plates the short dashed line, the long dashed line, and the solid line respectively represent the models with 3×10^{22}, 7×10^{22} and 10^{23} poise lower mantles, the latter being combined with a low viscosity channel. For sites under the ice sheet like Ottawa Islands and Churchill we see that increasing the lower mantle viscosity leads to a gradual decrease of the amplitude of emergence and an increase of the predicted present-day rate of emergence. This enables the model to reconcile the data from south-west quadrant sites like Churchill. At these interior sites the effect of the low viscosity channel is minor as expected.

For sites near the edge of the ice sheet like Prince Edward Island and Boston we note that an increase of lower mantle viscosity to 3×10^{22} poise reduces the amplitude of submergence at 8 kBP and so degrades the fit to these data which was achieved with the uniform viscosity model. The model does continue to predict an inward migrating bulge, though, which is the crucial characteristic of the RSL signature at such sites and we could presumably correct the misfit to this viscosity model by increasing the thickness of local ice. Further increases of lower mantle viscosity to 7×10^{22} poise, however, prevent forebulge migration and so such models cannot predict the observation of emergence followed by submergence. When a low viscosity zone is included in the model with 10^{23} poise lower mantle the misfit is only increased beyond that obtained when the low viscosity channel was absent (see Fig. 15). This is because the presence of this feature causes the peripheral bulge to migrate outwards rather than inwards.

At sites further to the south along the US east coast such as Clinton and Delaware we note as before that increasing the viscosity of the lower mantle reduces the amplitude of predicted submergence and thus reduces the misfit to the observations. The minimum misfit, however, is that achieved previously with the 10^{23} poise lower mantle model. When the low viscosity zone is introduced into the latter model the prediction fits the observations very nicely at Clinton but this is unfortunately not the case for other sites along the US east coast.

Gravity maps predicted by these models have the same form as those shown previously in Fig. 26. The magnitude of the low over Hudson Bay for the models with lower mantle

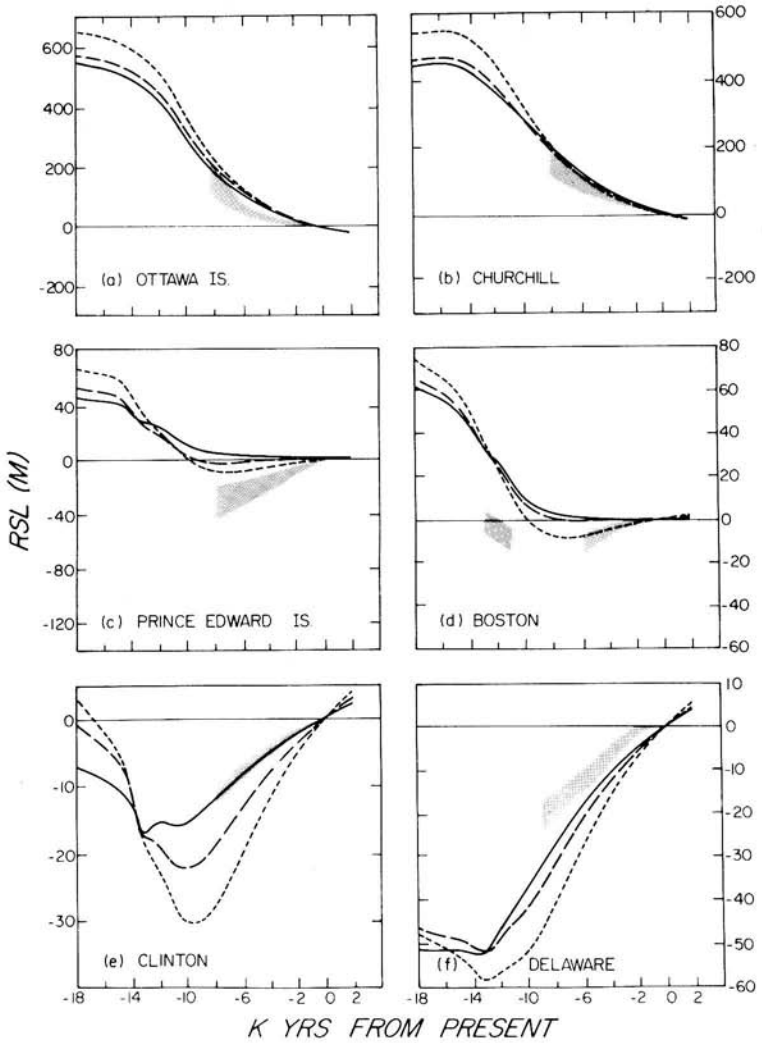

Figure 27. Same as Fig. 14 except that the dotted line, the long dashed line and the solid line now represent earth models with 3×10^{22}, 7×10^{22} and 10^{23} poise in the lower mantle respectively. The last model also has a 100 km thick 10^{21} poise low viscosity zone beneath the lithosphere.

viscosities of 3×10^{22}, 7×10^{23} and 10^{23} poise are respectively -36, -50 and -50 mgal. The equality of the last two numbers is due to the fact that the higher viscosity of the 10^{23} poise lower mantle model is offset by the low viscosity channel. Comparing these predictions with the -30 to -40 mgal observed anomaly we see that only the model with the 3×10^{22} poise lower mantle is able to satisfy the observations when initial isostatic equilibrium is assumed.

The results of the preceding two sections of this paper are summarized in Table 1 on the basis of which it is clear that the uniform viscosity model is the one best able to reconcile the totality of the RSL and gravity data from the Laurentian region. The model with lower mantle viscosity of 3×10^{22} poise is almost equally acceptable while those with still higher lower mantle viscosity are significantly inferior. In the next section we will proceed to investigate the question as to whether these conclusions are upheld when the effect of initial isostatic disequilibrium is taken into account.

Table 1. Summary of agreement between prediction and observation when the ICE-2 chronology is employed as deglaciation history.

	Viscosity model Lower mantle viscosity (P)	No. 1 10^{22}	No. 4 3×10^{22}	No. 5 7×10^{22}	No. 2 10^{23}	No. 3 5×10^{23}	No. 6 10^{23} + LVZ	Observed
I	Under the ICE sheet							Ottawa Islands
	(a) Present-day rate of uplift (mm yr^{-1})	4.8	12.1	14.3	14.1	15.8	10.9	4.7
	(b) Height of the 7 kBP beach (m)	150	160	150	155	110	155	140 ± 20
	(c) Curvature	√	√	×	×	×	×	√
II	Transition zone							Boston
	(a) Present-day rate of uplift (mm yr^{-1})	−1.36	−1.0	−0.2	−0.06	−0.11	+0.01	−0.9
	(b) Height of 5 kBP beach (m)	−12	−6	−0.2	+0.2	−0.2	+0.5	−8
	(c) Migration of forebulge	√	√	×	×	×	×	√
III	US east coast							Delaware
	(a) Present-day rate of uplift (mm yr^{-1})	−2.3	−3.0	−2.7	−2.4	−2.3	−2.3	−0.5
	(b) Height of 8 kBP beach (m)	−50	−41	−32	−30	−28	−29	−21
IV	Far field oldest raised beach (kBP)	8	8	8	8	8	8	6
V	Deglaciation isochrones	0.0	0.0	0.0	0.0	0.0	0.0	0.0
VI	Laurentia gravity (mgal) (Corrected for initial disequilibrium)	−24 (−19)	−42 (−36)	−60 (−44)	−62 (−49)	−80 (−52)	−50	−37 ± 5

6 The effect of initial isostatic disequilibrium

In the last subsection we demonstrated that when initial isostatic equilibrium is assumed we are able to constrain the viscosity increase across the seismic discontinuity at 670 km depth to be less than a factor of about three. In fact, notwithstanding misfits along the east coast of the US which may be epeirogenic in origin, the model with a uniform mantle viscosity of 10^{22} poise was preferred. The purpose of this section is to investigate the import of initial disequilibrium upon this conclusion. A preliminary analysis of this question was presented in Wu & Peltier (1982) but the discussion there was based upon the assumption of a circular disc load with parabolic height profile whose radius was independent of time. Under these assumptions we showed that the influence of initial disequilibrium was very important in so far as the free air gravity data were concerned but was very much less important for the relative sea-level information, at least at sites near the centre of the disc load.

The analysis to follow here is intended to extend our preliminary discussion in several important ways. First, we will explicitly allow for the variation of ice sheet radius with time as the volume of the ice sheet expands and contracts in response to the astronomical forcing. Secondly, we will investigate the influence of initial disequilibrium at sites both inside and outside the glaciated area. This is particularly important because the misfits along the east coast of the US could conceivably be due to the influence of initial disequilibrium rather than to epeirogenic processes. Finally, we will employ our formalism for incorporating disequilibrium effects in a full gravitationally self-consistent calculation.

6.1 THE RESPONSE DUE TO A SYMMETRICAL CIRCULAR DISC LOAD

We will begin to develop the formalism by considering a circular ice sheet of radius α_0 and centre at 0. The surface load per unit area applied to the Earth by this ice sheet may be represented by $L(\gamma, t)$ where γ is the angular distance from O and t is the time. The response at a field point Q due to $L(\gamma, t)$ may be calculated by convolution of L with the appropriate space–time Green's function $G(\theta, t)$. That is, if angular distance $\overline{OQ}$ is θ and the response is $R(\theta, t)$ then

$$R(\theta, t) = \int_{-\infty}^{t} \int_{s^1} L(\theta^1, t^1)\, G(\gamma^1, t - t^1)\, ds^1\, dt \tag{19}$$

where γ^1 is the angular distance between Q and the surface element ds^1 and s^1 is the surface area covered by the ice sheet. Now the impulse response Green's function has the normal mode expansion (Peltier 1976)

$$G(\theta, t) = G^{\mathrm{E}}(\theta)\, \delta(t) + \sum_{nj}\sum r_j^n \exp(-s_j^n t) P_n(\cos\theta) \tag{20}$$

where $G^{\mathrm{E}}(\theta)$ is the elastic part of the response and r_j^n and s_j^n are the initial amplitude and inverse relaxation time of the jth mode for the nth harmonic respectively. P_n is the usual Legendre polynomial.

If Q is a point outside the ice sheet then application of simple notions of spherical geometry and the notation of Fig. 28 results in the following expression for the viscous part of the response

$$R(\theta, t) = \sum_{nj}\sum \frac{r_j^n}{s_j^n} \exp(-s_j^n t)\, Q_j^n(\theta, t) \tag{21a}$$

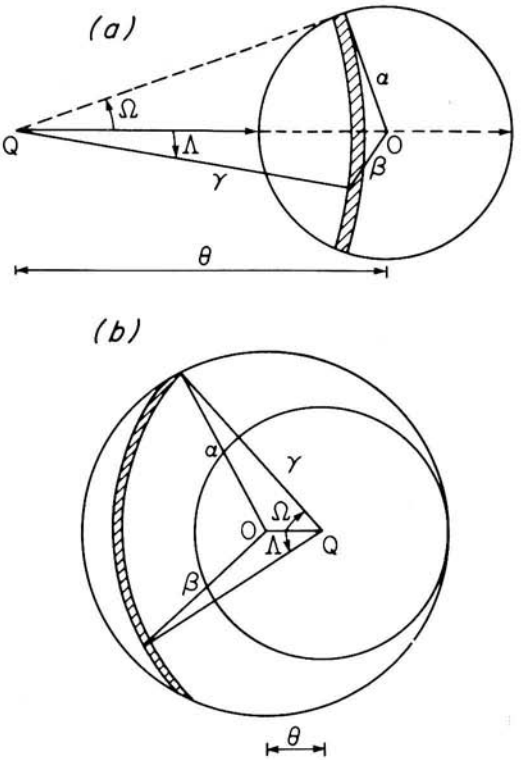

Figure 28. Notation used for the integration over parabolic loads.

where

$$Q_j^n(\theta, t) = \int_{-\infty}^{t} s_j^n \exp(s_j^n t^1) \left\{ \int_{\theta-\alpha_0}^{\theta+\alpha_0} F_n(\gamma, t^1, \theta)\, d\gamma \right\} dt^1 \tag{21b}$$

$$F_n(\gamma, t^1, \theta) = 2a^2 \sin\gamma P_n(\cos\gamma) \int_0^z L(\beta_+, t^1)\, d\Lambda \tag{21c}$$

$$\beta_+ = \cos^{-1}\left[\cos\theta\cos\gamma \pm \sin\theta\sin\gamma\cos\Lambda\right] \tag{21d}$$

$$Z = \cos^{-1}\left[\frac{\cos\alpha_0 - \cos\theta\cos\gamma}{\sin\theta\sin\gamma}\right]. \tag{21e}$$

If Q is a point inside the ice sheet, on the other hand, then making use of the notation in Fig. 28 we may express the viscous part of the response as

$$R(\theta, t) = \int_{-\infty}^{t} \left[\int_{\gamma=0}^{\alpha_0-\theta} \int_{\Lambda=0}^{2\pi} L(\beta, t^1)\, G(\gamma, t-t^1)\, a^2 \sin\gamma d\gamma d\Lambda + \int_{\gamma=\alpha_0-\theta}^{\alpha_0+\theta} \int_{\Lambda=-\Omega}^{+\Omega} L(\beta, t^1) G(\gamma, t-t^1)\, a^2 \sin\gamma d\gamma d\Lambda \right] dt^1 \tag{22}$$

or

$$R(\theta, t) = \sum_{nj}\sum \frac{r_j^n}{s_j^n} \exp(-s_j^n t)\, q_j^n(\theta, t) \tag{23a}$$

where

$$q_j^n(\theta, t) = \int_{-\infty}^{t} s_j^n \exp(s_j^n t^1) \left[\int_0^{\alpha_0+\theta} f_n(\gamma, t^1, \theta)\, d\gamma \right] dt^1 \tag{23b}$$

$$f_n(\gamma, t^1, \theta) = \begin{cases} 2a^2 \sin\gamma P_n(\cos\gamma) \displaystyle\int_0^{\pi} L(\beta_-, t^1)\, d\Lambda, & 0 \leqslant \gamma \leqslant \alpha_0 - \theta \\ 2a^2 \sin\gamma P_n(\cos\gamma) \displaystyle\int_0^{\Omega} L(\beta_+, t^1)\, d\Lambda, & \alpha_0 - \theta \leqslant \gamma \leqslant \alpha_0 + \theta \end{cases} \tag{23c}$$

$$\Omega = 2\cos^{-1}\left\{ \frac{\sqrt{\sin\xi \sin(\xi - \alpha_0)}}{\sin\gamma \sin\theta} \right\} \tag{23d}$$

$$\xi = 1/2(\gamma + \theta + \alpha_0). \tag{23e}$$

The above formulation will allow us to calculate the response given any space–time deglaciation history $L(\gamma, t)$. We will proceed to apply it to a sequence of interesting special cases.

6.2 THE RESPONSE TO ACCUMULATION AND DISINTEGRATION OF A DISC MODEL ICE SHEET OF FIXED RADIUS

If the radius of the circular load does not change in time and the thickness variations take place in concert at each point within the sheet then we may write L as

$$L(\gamma, t) = L_0(\gamma)\, \zeta(t) \tag{24}$$

in which case equations (21b) and (23b) above reduce to

$$Q_j^n(\theta, t) = \left\{ \int_{-\infty}^{t} s_j^n \exp(s_j^n t^1) \zeta(t^1)\, dt^1 \right\} \left\{ \int_{\theta-\alpha_0}^{\theta+\alpha_0} F_n(\gamma, \theta)\, d\gamma \right\} \tag{25}$$

$$q_j^n(\theta, t) = \left\{ \int_{-\infty}^{t} s_j^n \exp(s_j^n t^1) \zeta(t^1)\, dt^1 \right\} \left\{ \int_0^{\alpha_0+\theta} f_n(\gamma, \theta)\, d\gamma \right\} \tag{26}$$

and L in the expressions for F_n and f_n is to be replaced by L_0.

For the purposes of our present calculations we will assume that the load is parabolic in shape so that

$$L_0(\theta) = \begin{cases} \rho_1 \sqrt{a\lambda[\alpha_0 - \theta]}, & 0 \leqslant \theta \leqslant \alpha_0 \\ 0, & \theta > \alpha_0. \end{cases} \tag{27}$$

In this expression we take λ such as to give an ice sheet thickness of 3500 m for a disc load with radius equal to the Laurentia radius or to give a thickness equal to 2500 m for an ice sheet of Fennoscandia scale.

As in the companion paper (Wu & Peltier 1982) we may approximate the time dependence $\zeta(t)$ on the basis of oxygen isotope data taken from deep sea sedimentary cores. Imbrie & Kipp (1971) showed that the variability of the O^{18}/O^{16} ratio for the most part reflected the variation of northern hemisphere ice volume. Broecker & Van Donk (1970) pointed out from the same data that the glacial–deglacial cycle had a period of about 10^5 yr which has since been very elegantly verified by Hays, Imbrie & Shackleton (1976). These data have furthermore established that the time-scale of accumulation of an Ice Age ice sheet

is very much longer than the time-scale of disintegration. This suggests that a reasonable approximation to $\zeta(t)$ for the present purposes might be

$$\zeta(t) = \frac{t + k\Delta t}{\Delta t}, \quad -k\Delta t \leqslant t \leqslant -(k-1)\,\Delta t \tag{28}$$

with $\Delta t = 10^5$ yr.

For the sake of simplicity we shall assume as in the companion paper (Wu & Peltier 1982) that there have been $N = 30$ such cycles since the Ice Age began (in fact $N = 20$ would be a better approximation but this makes no difference to our conclusions). If t is time measured from the end of the last of these 30 cycles then the time integrals in equations (25) and (26) may be expressed analytically as

$$\beta_j^n = \sum_{k=1}^{N} \int_{-k\Delta t}^{-(k-1)\Delta t} s_j^n \exp(s_j^n t') \frac{(t' + k\Delta t)}{\Delta t}\, dt'$$

$$= \left[1 - \frac{1-\exp(-s_j^n \Delta t)}{s_j^n \Delta t}\right] \left[\frac{1-\exp(-Ns_j^n \Delta t)}{1-\exp(-s_j^n \Delta t)}\right]. \tag{29}$$

The response at time t can then be calculated by doing the numerical quadratures in γ in (25) and (26) to obtain Q_j^n and q_j^n for the summations (21a) and (23a). Discussion of numerical results for these fixed radius models will be deferred until the next subsection where they will be compared to calculations which include the effect of variable radius.

6.3 THE RESPONSE TO DISC LOADS WITH CONTINUOUS VARIATION OF RADIUS

Throughout the glaciation cycle of the Ice Age, as ice sheets grow and decay their horizontal scale increases as the volume increases (and vice versa) and this continuous change of horizontal scale can be expected to contribute substantially to the departure of a given ice complex from isostatic equilibrium at a given time. The model distintegration histories discussed in the last subsection were based upon the assumption that the ice sheet maintained its maximum horizontal scale at all times, even while its volume decreased to zero. This is of course completely unrealistic and one might expect, because the largest horizontal scales tend to have the shortest isostatic adjustment times, that fixed radius models would severely underestimate the importance of initial isostatic disequilibrium. Analysis presented in this subsection will demonstrate that this simple intuitive expectation is not realized because of the complex relaxation spectrum of realistic viscoelastic models of the Earth.

In order to incorporate the effect of radius variations into our parabolic load models we may simply write

$$L(\beta, t) = \begin{cases} \rho_I \sqrt{a\lambda[\alpha(t) - \beta]}, & 0 \leqslant \beta \leqslant \alpha(t) \\ 0, \quad \text{otherwise} \end{cases} \tag{30}$$

which amounts to assuming that the ice sheet maintains an equilibrium plastic profile at all times in its history (Paterson 1981). The function $\alpha(t)$ is then fixed by an assumption as to how the ice sheet volume changes in time and this is determined by the oxygen isotope stratigraphy in deep sea sedimentary cores as discussed previously. The volume of an ice sheet with profile described by the perfectly plastic relation (30) is given by

$$V(t) = \frac{8\pi}{15} \sqrt{\lambda a^5 \alpha^5(t)}. \tag{31}$$

Since the previously discussed oxygen isotope stratigraphy suggests a saw-tooth time history

for ice volume we may again take

$$V(t) = V_0 \frac{(t + k\Delta t)}{\Delta t}, \quad -k\Delta t \leqslant t \leqslant -(k-1)\,\Delta t \tag{32}$$

for the functional dependence of V in each glaciation cycle. Comparison of (32) with (31) gives

$$V_0 = \frac{8\pi}{15}\sqrt{\lambda a^5 \alpha_0^5} \tag{33}$$

$$\alpha(t) = \alpha_0 \left[\frac{(t + k\Delta t)^{2/5}}{\Delta t^{2/5}}\right], \quad -k\Delta t \leqslant t \leqslant -(k-1)\,\Delta t$$

V_0 is then the volume of the ice sheet at its maximum radius α_0. The variation of $\alpha(t)$ in each load cycle is illustrated in Fig. 29(b), inspection of which shows that the radius initially increases very rapidly such that it exceeds 50 per cent of its final value in the first 30 per cent of the load cycle (i.e. 30 000 yr). This figure therefore serves to demonstrate that the assumption of a fixed large radius for the ice sheet throughout the load cycle should be a good first approximation so long as the assumption of perfect plasticity does not introduce significant error.

When (3) and (33) are substituted into (21c) and (23c) the response to the continuously expanding and contracting disc model ice sheet can be calculated by direct numerical quadrature. An important difficulty which must be carefully kept track of while doing these calculations is that as the disc expands and contracts, points which are at times inside the disc may later lie outside the disc and this determines whether equations (21) or (23) should be used for that time.

In Fig. 30(a, b) we illustrate the effect of initial disequilibrium on the free air gravity anomaly measured at the centre of parabolic disc load approximations to the Laurentian and Fennoscandian ice sheets. The present-day gravity anomaly is shown as a function of lower mantle viscosity for three different models of the glaciation prehistory. The hatched regions show the range within which the peak anomalies over Laurentia and Fennoscandia are observed to lie. The upper dash-dot curves in these figures are the present-day anomalies computed on the basis of the assumption that isostatic equilibrium prevails initially. The

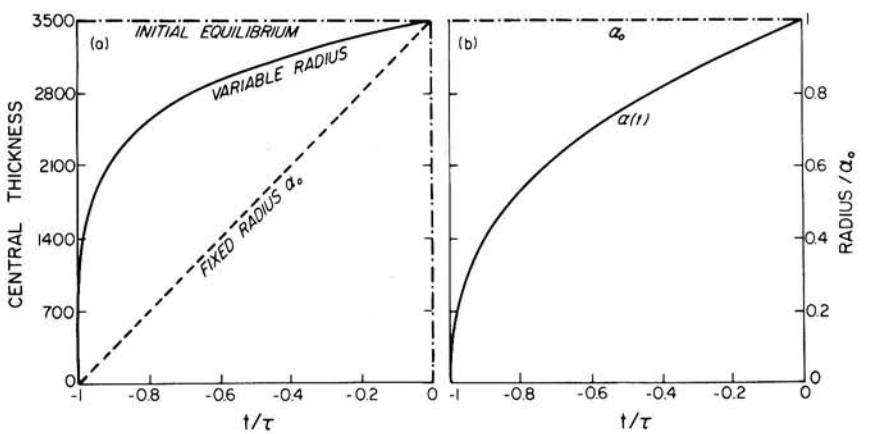

Figure 29. (a) This plot shows how the thickness at the centre of a parabolic ice load with size comparable to the Laurentide changes in one cycle of glacial loading. (b) This shows how the radius of the parabolic ice load change in one cycle of glacial loading. τ is the period of loading, approximately 10^5 yr. α_0 is the radius at glacial maximum.

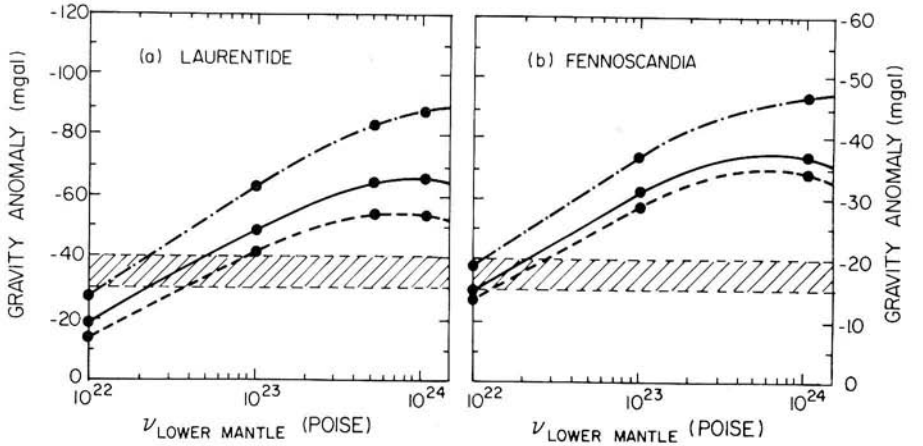

Figure 30. Plot of present-day gravity anomaly predicted at the centre of the parabolic loads as a function of lower mantle viscosity. The horizontal hatched region is the observed range of anomaly over these deglaciated areas. The dash-dot lines shows the anomaly which would obtain if initial equilibrium is assumed. The dashed line shows the effect of disequilibrium if the size of the ice load is fixed. The solid lines show the effect of disequilibrium when the size of the load is allowed to vary in time.

lower dashed curves in the figures include the effect of initial disequilibrium when the radius of the disc loads are held constant and equal to the radius at Würm–Wisconsin maximum. The first two curves in Fig. 30(a) are the same as obtained previously in Wu & Peltier (1982). The solid curves which lie intermediate between the two extremes include the time variation of the load radius which is predicted on the basis of the assumption that the ice sheet is perfectly plastic.

Comparison of the two dashed curves in Fig. 30 shows that when account is taken of the effect of initial isostatic disequilibrium the predicted present-day gravity anomaly is reduced from that obtained in the absence of this effect. For models with lower mantle viscosity of 10^{22} poise the dominant relaxation times of the earth model are shorter than the loading time-scale of 10^5 yr and so including the effect of initial disequilibrium does not substantially modify the prediction. Such reduction of the anomaly as is obtained is due to the fact that the viscoelastic model also supports an important secondary family of modes with rather long relaxation times due to the internal density jumps in the mantle associated with the phase transitions in the 'transition' region between 400 and 700 km depth. As the viscosity of the lower mantle increases, however, the dominant relaxation times become long compared to the time-scale of loading and eventually, for lower mantle viscosities in excess of about 10^{24} poise, the central anomaly decreases with further increase of viscosity.

When the effect of time variation of ice sheet radius is taken into account (the solid curves in Fig. 30) we discover an effect which was initially unexpected. In this case the influence of initial disequilibrium is reduced for that in the fixed radius case rather than increased. The reason for this is to be found in the nature of the relaxation spectra for these realistic viscoelastic earth models. Inspection of fig. 9(a) of Wu & Peltier (1982) shows that decreasing the dominant horizontal scale of the load decreases the relaxation time of the M1 mode supported by the spinel → perovskite + magnesiowustite transition at 670 km depth. Table VIII of Wu & Peltier (1982) also shows that the importance of this slowly decaying mode also decreases as the scale decreases. The response to the load with varying radius will therefore be less affected by initial disequilibrium. In Fig. 29(a) we show how the thickness of the Laurentian ice sheet changes through one loading cycle when the radius is fixed and when it is computed on the assumption of perfect plasticity. The time dependence of the

radius for the latter case is also given and inspection of the figure shows that it initially increases very rapidly, reaching 60 per cent of its final thickness in the first 8 per cent of the load cycle. Since the equilibrium plastic approximation to the instantaneous ice sheet profile is probably a good first estimate (Paterson 1981), we can see why our initial approximation of constant ice sheet radius yielded a good estimate of the influence of disequilibrium.

Fig. 30(a) shows, to the extent that the disc model Laurentian load is an adequate approximation, that the observed free air gravity anomaly can be invoked to place rather stringent bounds upon the viscosity of the deep mantle ν_{LM}. When the effect of initial disequilibrium is ignored, then the bounds are 10^{22} poise $\leqslant \nu_{LM} \leqslant 2$–$3 \times 10^{22}$ poise if the observed peak anomaly is taken as $-40\,\text{mgal} \leqslant \Delta g_{max} \leqslant -30\,\text{mgal}$. When the effect of disequilibrium is included but the ice sheet radius is kept fixed the bounds are 4×10^{22} Poise $\leqslant \nu_{LM} \leqslant 8 \times 10^{22}$ poise, while with varying ice sheet radius we obtain 2×10^{22} poise $\leqslant \nu_{LM} \leqslant 5 \times 10^{22}$ poise. (The ultra-high viscosity root near $\nu_{LM} = 10^{25}$ poise as shown in the last section is clearly incompatible with the relative sea-level observations discussed previously.) On the basis of the disc model calculations some small increase of viscosity will therefore be required to fit the observed free air anomaly over the Laurentia and Fennoscandia regions. On the basis of results discussed in the last section the required increase is not ruled out by the relative sea-level data. Fig. 30(b) also shows that in order to fit the gravity data in Fennoscandia, the viscosity of the lower mantle has to be between 10^{22} and 2×10^{22} poise when the effect of disequilibrium is taken into account and the radius of the ice sheet is allowed to vary. This is a rather important point which we expect to hold up when the effect of disequilibrium is included in a more realistic calculation (Section 6.5) because the gravity anomalies described in the last section do agree with those obtained with the simple disc load computation described here.

Of course the deviation from initial isostatic equilibrium affects not only the gravity anomaly but also the history of radial displacement, which to a good first approximation provides a reasonable estimate of the relative sea-level record in the post-glaciation era. Here we wish to consider the extent to which this effect might be invoked to explain the misfits between theory and observation previously obtained (Section 5) for sites along the east coast of the USA. In Fig. 31(a, b) we show expanded views of the radial displacement response in the vicinity of the edge of the parabolic disc load of Laurentian size (radius =

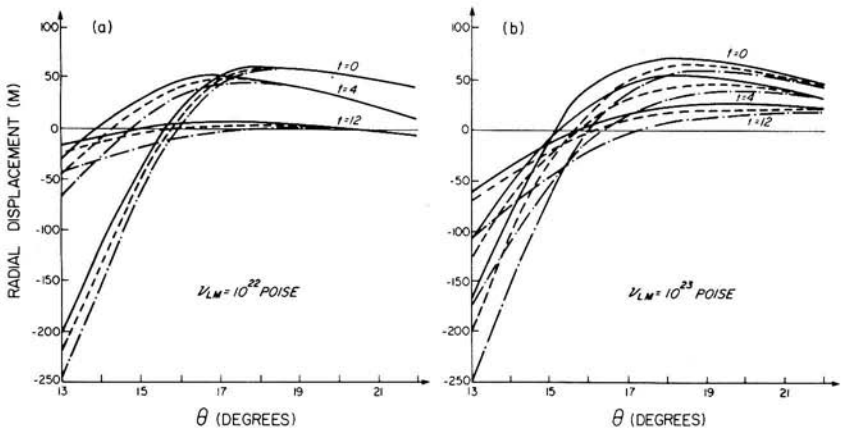

Figure 31. A cross-country portrayal of the isostatic adjustment of the Earth's surface at time t after the removal of a parabolic load of radius 15°. The number beside the curves are the time in thousands of years after the instantaneous removal of the load. The notation of the lines are the same as in Fig. 30. (a) is for the uniform viscosity model, (b) is for the model with 10^{23} poise lower mantle.

15°). (a) is for the uniform viscosity model and (b) is for the model with 10^{23} poise lower mantle viscosity. For each viscosity model we show the response at three times ($t = 0$, 4 and 12 kyr) and for each time we show the response computed on the basis of three different assumptions as to the time history of loading. The dash-dot curve, short dashed curve and solid curve for each time describes respectively the response assuming initial equilibrium, assuming a glacial cycle with fixed ice sheet radius, and assuming a glacial cycle with ice sheet radius a function of time determined on the basis of the assumption of perfect plasticity. Inspection of (a) and (b) shows the markedly different characteristic response of models with and without high lower mantle viscosity. For the uniform 10^{22} poise model the peripheral bulge first migrates inwards slightly but after about 4 kyr its direction of migration reverses, migrating quickly outwards such as to cover 5° in only 8 kyr. As the bulge migrates its amplitude rapidly collapses. For the model with the 10^{23} poise lower mantle, on the other hand, the bulge does not migrate substantially in time, it collapses almost *in situ*. Including the effect of initial isostatic disequilibrium only enhances this tendency. For such models the hinge of zero response has, however, moved somewhat closer to the ice sheet edge. In the next subsection we shall investigate this effect through analysis of the free air gravity field since, as we demonstrated in Section 5, the predicted free air gravity maps have their zero contours somewhat further from the ice sheet terminus than the observations would suggest. As we shall show, initial disequilibrium might be invoked to reconcile this difficulty.

On the basis of a complete sequence of calculations of the sort shown in Figs 32 and 33 we have computed the radial displacement response curves at six different locations with respect to the ice sheet centre ($\theta = 0°$, 13°, 15°, 16°, 18°, 25°). At each site we have done these computations using each of the three previously discussed models of the deglaciation prehistory and for both the uniform mantle viscosity model and that with high viscosity (10^{23} poise) beneath 670 km depth. Also shown in each plate is a set of observational data from a site which is from an equivalent location with respect to the disc edge. The correspondence is roughly $\theta = 0°$ (Ottawa Islands), $\theta = 13°$ (Newfoundland), $\theta = 15°$ (Prince Edward Island), $\theta = 16°$ (Clinton, Connecticut), $\theta = 18°$ (Brigantine, New Jersey), $\theta = 25°$ (Florida). Inspection of the response at the disc centre ($\theta = 0°$) shows that the effect of initial disequilibrium is very limited at sites in this region and is unaffected by the time dependence of the ice sheet radius. This confirms the conclusion reached in Wu & Peltier (1982). As one approaches the edge of the ice sheet this effect increases, however, and its magnitude *is* a strong function of whether or not one takes into account the time variation of ice sheet scale. The sense of this dependence is particularly important at sites like Prince Edward Island and Clinton. As was shown in Section 5 the latter site had a strong preference for some considerable increase in lower mantle viscosity since such models minimized the RSL misfits at these locations when initial isostatic equilibrium was assumed. This is also predicted by the disc load responses at $\theta = 16°$ shown in Fig. 33. The plausibility of this explanation (high lower mantle viscosity) of the misfits at Clinton is completely undermined, however, when the effect of initial disequilibrium is taken into account. Incorporation of the effect of varying ice sheet radius on the high lower mantle viscosity model completely destroys the improved fit to the data. The effect for the 10^{22} poise uniform viscosity model is very much less extreme. Also of interest are the comparisons at $\theta = 25°$ (in Florida) which show that the influence of initial disequilibrium decreases again with increasing distance from the disc edge. At this site the observations are bracketed by the uniform viscosity model and that with 10^{23} poise in the lower mantle, indicating that the preferred viscosity model is intermediate between these two. This is very encouraging given that the free air anomalies discussed in connection with Fig. 30(a) show precisely the same preference.

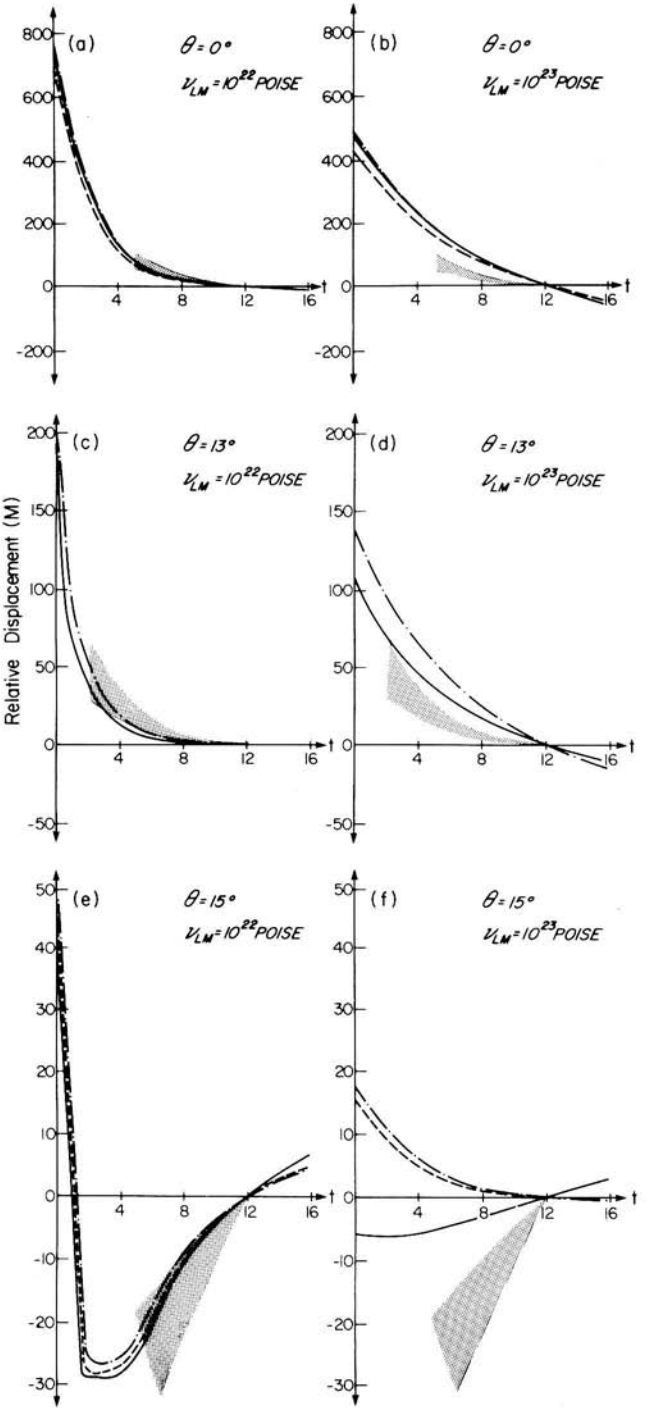

Figure 32. Relative displacement curves at $\theta = 0$ (a, b), 13° (c, d), and 15° (e, f) from the centre of the parabolic load of radius 15°, which is removed instantaneously at $t = 0$. The stippled areas are the observations at Ottawa Islands, NW Newfoundland and Prince Edward Island respectively. The notation of the lines are the same as in Fig. 30. The left-hand plates are for the uniform viscosity model and the right-hand plates are for the model with 10^{23} poise lower mantle.

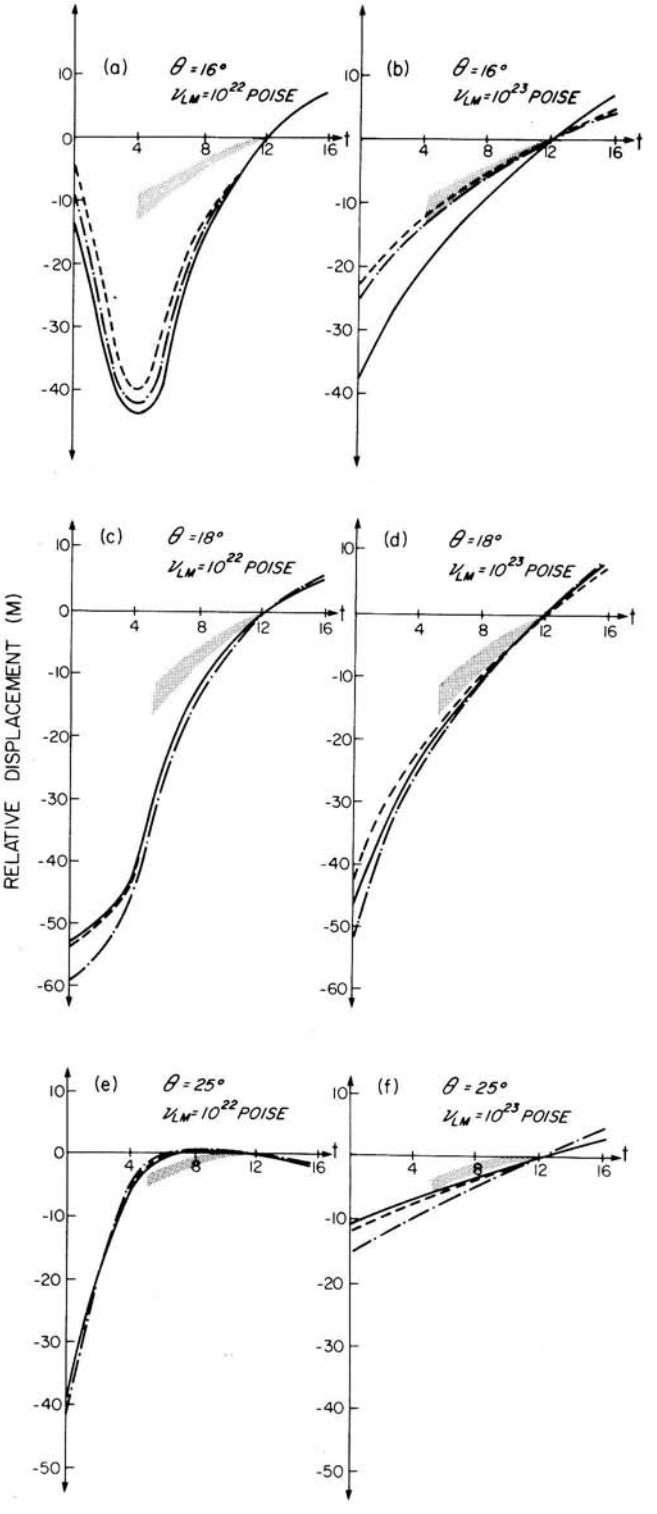

Figure 33. Same as Fig. 32 except the locations are at θ = 16°, 18°, 25° for (a) and (b), (c) and (d), and (e) and (f) respectively. The data are from Clinton, Brigantine and Florida.

6.4 THE EFFECT OF INITIAL DISEQUILIBRIUM UPON GRAVITATIONALLY SELF-CONSISTENT CALCULATIONS

Virtually all of the conclusions reached previously on the basis of the disc load histories are further reinforced when the realistic deglaciation chronology ICE-2 is employed and the response calculation is done using the gravitationally self-consistent theory. Of course, in order to include the effect of initial disequilibrium accurately in such calculations one would have to know the detailed history of glaciation and deglaciation for at least the last half-million years and this clearly is unavailable. The approach which we will follow here is rather to make use of the concept of an error Green's function developed in Wu & Peltier (1982) in order to correct the calculations based upon the assumption of initial equilibrium by invoking the simple saw-tooth prehistory based upon the observed oxygen isotope stratigraphy in deep sea sedimentary cores. The calculation proceeds as follows.

Suppose we denote by $L_p(\mathbf{r}, t)$ the history of glaciation prior to 18 kBP at which time the last major deglaciation event began. The deglaciation history to 18 kBP will be denoted by $h(\mathbf{r}, t)$ so that the entire load history $L(\mathbf{r}, t)$ is

$$\begin{aligned} L(\mathbf{r}, t) &= L_p(\mathbf{r}, t), \quad t < t_0 \\ &= h(\mathbf{r}, t), \quad t \geq t_0 \end{aligned} \tag{34}$$

where $t_0 = 18$ kBP. We may compute any response by convolving $L(\mathbf{r}, t)$ with an appropriate Green's function as

$$R(\mathbf{r}, t) = \int_{-\infty}^{t_0} G(t-t')^* L_p(t')\, dt' + \int_{t_0}^{t} G(t-t')^* h(t')\, dt' \tag{35}$$

where the spatial convolution is denoted by *. If we assume that the prehistory may be separated into a product of spatial and temporal parts then we may write

$$L_p(\mathbf{r}, t) = L_p(\mathbf{r})\, \zeta(t) \tag{36}$$

and the first integral on the rhs of (35) may be written as

$$\int_{-\infty}^{t_0} G(t-t')^* L_p(t')\, dt' = L_p^* \sum_{nj}\sum \frac{r_j^n}{s_j^n} \exp(-s_j^n t)\, \beta_j^n P_n(\cos\theta) \tag{37}$$

where

$$\beta_j^n = \int_{-\infty}^{t_0} s_j^n \exp(s_j^n t')\, \zeta(t')\, dt'. \tag{38}$$

It therefore follows that if one prehistory $L_{p1}(\mathbf{r}, t) = L_p(\mathbf{r})\, \zeta_1(t)$ gives a response $R_1(t)$ and another $L_{p2}(\mathbf{r}, t) = L_p(\mathbf{r})\, \zeta_2(t)$ gives $R_2(t)$ then the difference between them is just

$$R_1(t) - R_2(t) = L_p^* \sum_{nj}\sum \frac{r_j^n}{s_j^n} \cdot \exp(-s_j^n t\, [\beta_{1j}^n - \beta_{2j}^n]\, P_n(\cos\theta). \tag{39}$$

For the special case

$$\zeta_2(t) = 1 - H(t-t_0) \tag{40}$$

which describes a load which is left on the surface of the Earth an infinite length of time and then instantaneously removed, initial equilibrium clearly obtains at $t = t_0$ and from (38) $\beta_j^n = 1$. The difference (39) can then be interpreted as the error committed by assuming equilibrium when the actual prehistory is described by $\zeta_1(t)$. This difference can clearly be written as

$$R_1(t) - R_2(t) = - L_p * E(t) \tag{41}$$

where $E(\mathbf{r}, t)$ is the error Green's function. Given the error Green's function

$$E(\mathbf{r}, t) = - \sum_{nj} \sum \frac{r_j^n}{s_j^n} \exp(-s_j^n t\,[1 - \beta_{1j}^n]\, P_n(\cos\theta) \tag{42}$$

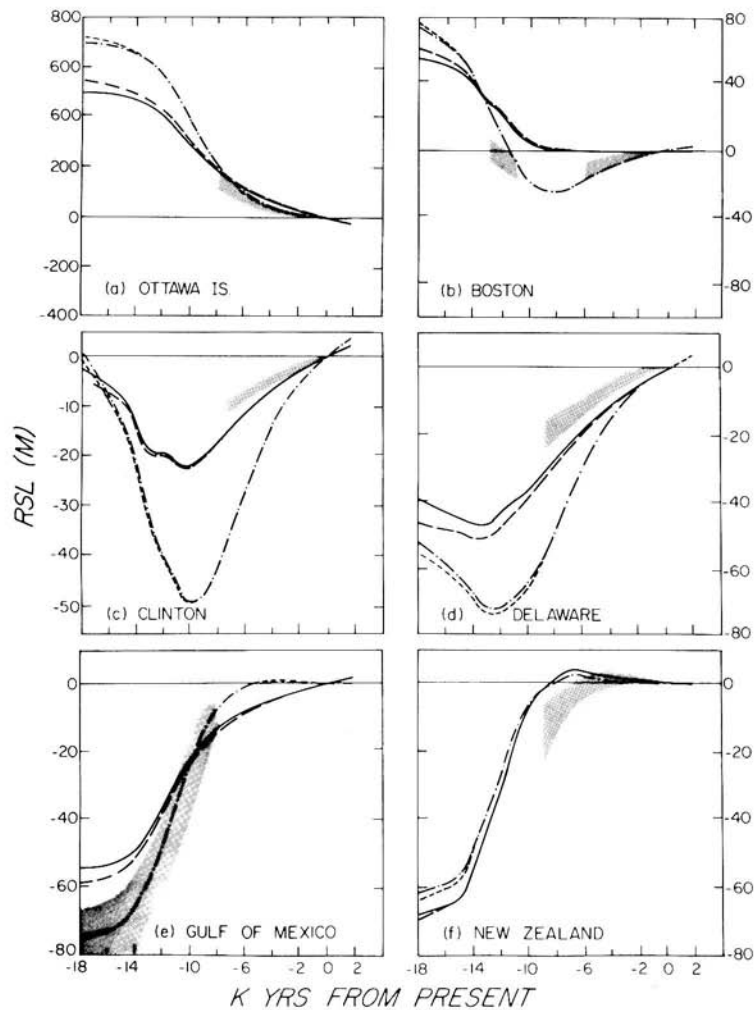

Figure 34. The effect of disequilibrium for RSL curves calculated with realistic deglaciation histories. The short dashed lines and the dash-dot lines are RSL curves for the uniform viscosity model. The short dashed lines assume initial equilibrium but the dash-dot line takes into account the effect of disequilibrium. The long dashed lines and the solid lines are for model with 10^{23} poise lower mantle. Again the former assume initial equilibrium but the latter do not.

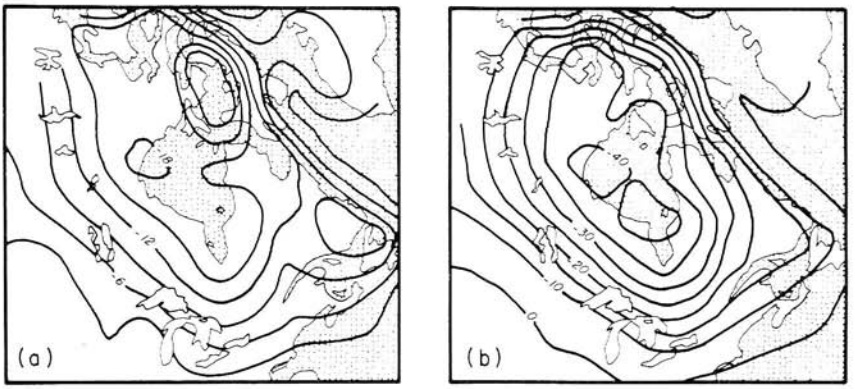

Figure 35. Same as Fig. 26 except here the effect of disequilibrium has been taken into account.

one can then compute the error committed at point **r** by convolution with the 'initial' load to $t = t_0$ or, for the realistic calculations with the total surface load (ice and water) at 18 kBP. For absolute measurements such as free air gravity anomalies the actual response is just the sum of that obtained under the assumption of initial equilibrium and the correction determined by the expression (41). For a relative response, such as relative displacement or relative sea-level, the correction factor is just $-h_0^*[E(t) - E(t_p)]$ where t_p is the present time.

In order to estimate the effect of disequilibrium we have chosen $\zeta_1(t)$ to be the saw-tooth function employed previously with the period fixed at 10^5 yr. Error Green's functions for both uniform viscosity model and for the model with 10^{23} poise lower mantle were constructed and relative sea-level curves for both models which include the disequilibrium effect are shown in Fig. 34. The short dashed curve and the long dashed curve are calculated assuming initial equilibrium. The short dashed curve is for a model with 10^{22} poise lower mantle, the long dashed curve is for 10^{23} poise lower mantle. They are the same ones as in Figs 14–18, and assume ICE-2. The dash-dot curve and the solid curve include the effect of disequilibrium and are for models with 10^{22} and 10^{23} poise viscosity in the lower mantle respectively. Inspection of these curves shows that the effect is generally small, particularly during the last 10 kyr and is in the sense of reducing the amount of submergence or emergence predicted. This is in accord with our conclusions in the last subsection.

The effect of initial disequilibrium on the free air gravity anomalies for these two viscosity models is illustrated in Fig. 35 (a, b). Comparing these results with those for the disc models shown in Fig. 30 shows that the disc calculations were very good approximations. The most significant effect of initial disequilibrium obtains for the model with 10^{23} poise lower mantle which shows the expected reduction of the peak gravity anomaly of about 20 mgal. It is also important to note (Fig. 35b) that the zero anomaly contour on this map is everywhere significantly closer to the ice sheet centre than was predicted under the assumption that initial equilibrium prevailed (Fig. 26). This may be taken as an additional argument for some increase of deep mantle viscosity although the error in the location of the zero observational isobase is quite large so that we must be careful not to attach too much significance to it.

7 The sensitivity of the inferred mantle viscosity profile to errors in the deglaciation history

All of the analysis in the preceding sections has been predicated upon the assumption that the actual deglaciation chronology is very well approximated by ICE-2. However, it has not

proved to be possible to fit all of the observed RSL and gravity data in terms of this model and the question remains as to whether the actual deglaciation history might not be significantly different from ICE-2. The major observational constraint on ICE-2 is the pattern of distintegration isochrones which control the time dependence of the location of the ice margin (Bryson *et al.* 1969). Although the measurement errors in the timing of ice sheet contraction should not be much greater than ± 500 yr and the systematic errors (Suess 1970) are such that sidereal age is systematically greater than radiocarbon age (see Section 4) we will investigate the possibility in this section that the actual melting event may have been considerably delayed from that for the ICE-1(2) chronology tabulated by Peltier & Andrews (1976).

Our reason for investigating this *a priori* unlikely possibility is based upon the far field RSL data discussed in Section 5 and shown in Fig. 18. These data demonstrate that the far field emergence curves predicted by all viscosity models are time-shifted by about 2000 yr from the observed RSL data in the sense that melting has apparently occurred too early in the model. In their initial study of the gravitationally self-consistent problem for the RSL variation, Clark *et al.* (1978) assumed this apparent difficulty to be real and based their calculations on a time-shifted version of the Peltier & Andrews (1976) melting history. What we will proceed to demonstrate here is that this extreme modification of the load history is impossible to reconcile with the observed RSL and free air gravity data. As we will point out at the end of this section the explanation of the misfits of observation and theory at far field sites are readily explicable without the necessity of recourse to such dramatic modification of what is after all a well-constrained input to the sea-level calculation.

With their time-shifted version of the ICE-1(2) melting chronology, Clark *et al.* (1978) were able to fit far field RSL data but only at the expense of introducing far larger errors at near field sites. As pointed out in Peltier *et al.* (1978), the misfits in the near field were huge, with errors along the east coast of the US typically on the order of 300 per cent and those under the ice on the order of 100 per cent. Clark (1980) has employed linear inverse theory to make the obvious point that the near field misfits require that the Laurentian ice sheet thickness be reduced (see Peltier 1980). In order to demonstrate that this approach leads to inconsistent results what we will do is to refine this delayed melting history in order to best fit the near field RSL data. This will lead to the requirement of high lower mantle viscosity to simultaneously fit the observed gravity anomaly even when initial equilibrium is assumed. For this high lower mantle viscosity model, however, the effect of initial isostatic equilibriumum is extremely important and this requires a lower mantle viscosity which is so high that RSL data cannot be simultaneously reconciled with gravity information. The exercise amounts to an extremely useful demonstration of the power of the *joint* constraints provided by RSL and free air gravity information.

7.1 A THIN ICE SHEET WHICH MELTS LATE: THE ICE-3 CHRONOLOGY

On the basis of the discussion in Clark *et al.* (1978) and Peltier *et al.* (1978) it is quite clear that the thickness of the Laurentian ice sheet must be reduced by a factor of approximately 2 if melting is delayed by 2000 yr from that in the ICE-1(2) chronology. We produced a preliminary version of the thin ice sheet which melts late by introducing this modification and some others which were required after preliminary calculations had been completed (see Fig. 38a). It was found necessary to remove the ice from over Nova Scotia in order to obtain sea-level curves characterized by submergence followed by emergence. Also, deglaciation over NW Newfoundland had to be delayed by a further 4 kyr in order that the prediction show pure emergence. Some RSL data predicted with this preliminary model are shown in Figs 36 and 37 for our three basic velocity models, that with uniform mantle viscosity of

10^{22} poise, that with a lower mantle viscosity of 10^{23} poise, and that with a lower mantle viscosity of 5×10^{23} poise.

Inspection of Fig. 36 shows that the RSL data prefer the same viscosity model as found with the ICE-2 melting chronology. Most of the data from interior sites are best fitted by the uniform viscosity model though some prefer that with the 10^{23} poise lower mantle (i.e. in the south-west sector of Hudson Bay). Again the model with lower mantle viscosity of 5×10^{23} poise is quite strongly rejected since it predicts too little total emergence.

At sites near the ice sheet, this thin ice sheet is seen to produce a much smaller amplitude of submergence and emergence. In fact the emergence in Boston is so small for models with high viscosity lower mantle that the relative sea-level response is dominated completely by the rise in sea-level at that location. There are also some errors in timing which appear to require further adjustment of the ice history to fit the data. For sites further down the US east coast (Fig. 37a, c, e) we find the same problem as with ICE-2 in that the amplitude of

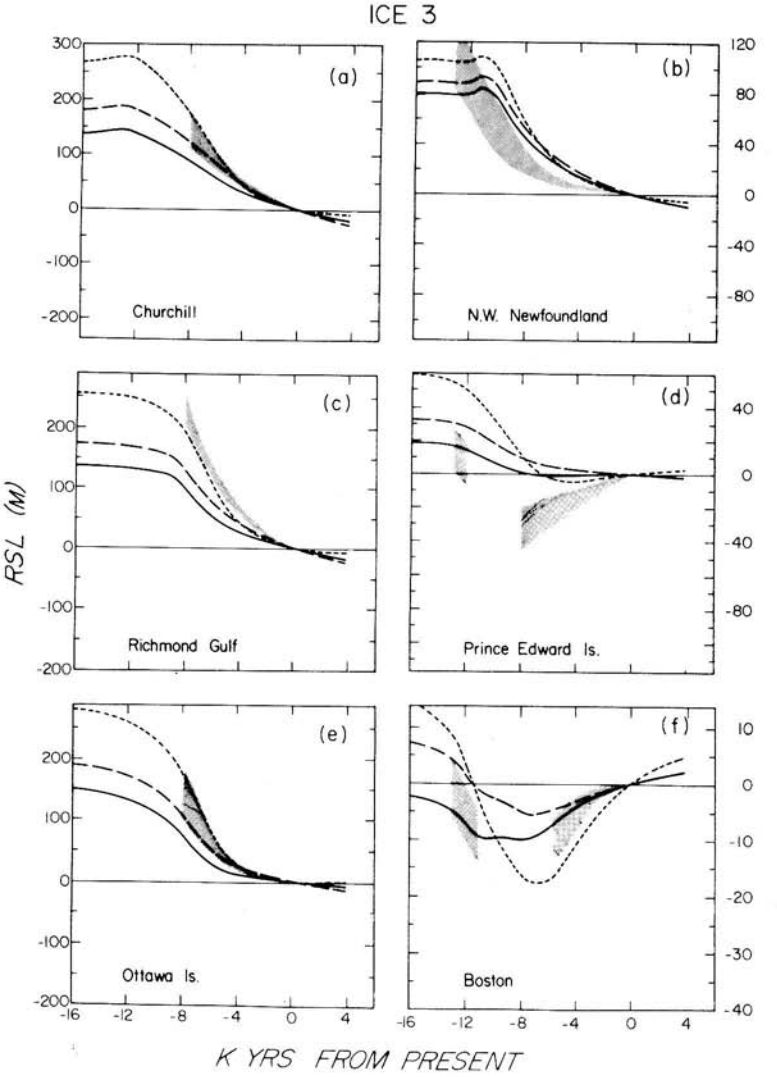

Figure 36. Same as Fig. 14 except that the ICE-3 model is used.

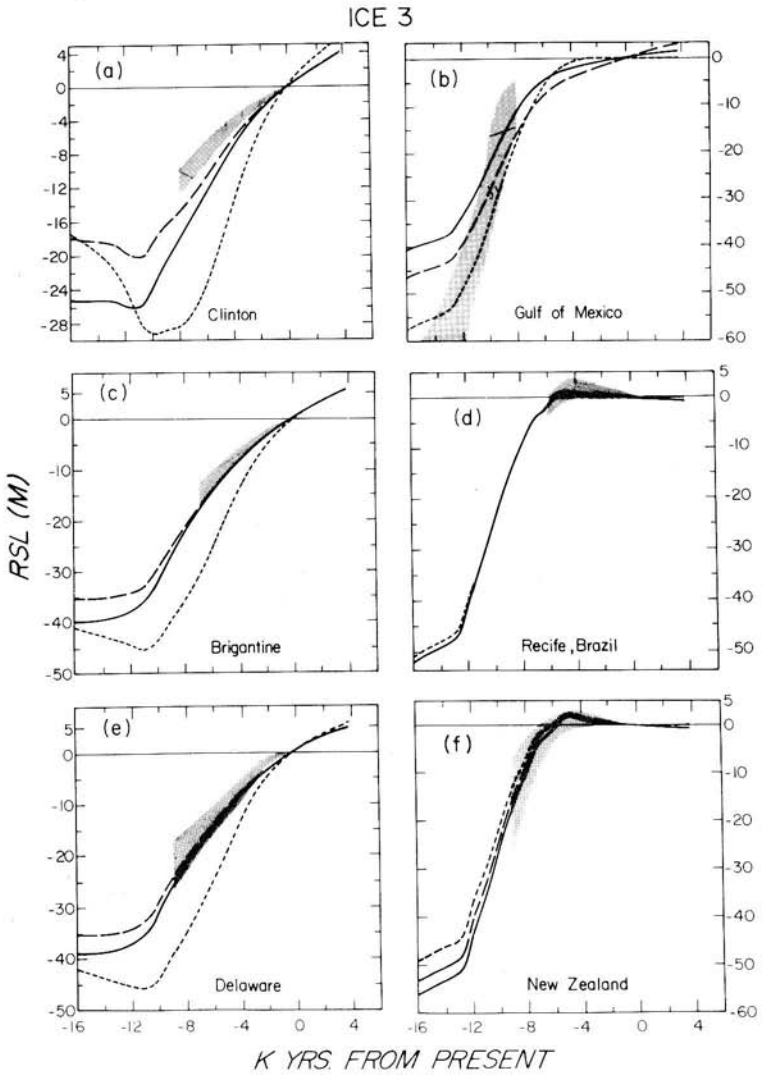

Figure 37. Same as Fig. 36.

submergence predicted by the 10^{22} poise model is too large. For models with high lower mantle viscosity, however, the predicted and observed RSL curves are very close (e.g. Brigantine, Delaware). This is for the most part due to the reduced amount of water in ICE-3. In the Gulf of Mexico (Fig. 37b) this deficit of meltwater has a very unsatisfactory effect since the predicted submergence at 16 kBP is less by about 20 m than the observed submergence. At the sites most distant from the deglaciation centres (Recife, Brazil; South Island, New Zealand) we should not be too surprised to discover that with the deglaciation delayed by 2000 yr all these data are fitted quite nicely. It must be kept in mind, however, that the good fit to these far field data has been achieved only by sacrificing the fit of the deglaciation model to the disintegration isochrones – which is clearly unsatisfactory.

On the basis of the RSL data alone, the ICE-3 melting history shows some preference for the 10^{22} poise uniform viscosity model at sites under the ice sheet and near the ice sheet margin. On the other hand, outside the margin and for some sites in the SW corner of

Hudson Bay the model with the 10^{23} poise lower mantle is preferred. This situation is very similar to that encountered with ICE-1(2).

The similarity does not extend to the free air gravity signal, however. The predicted present-day free air gravity anomalies for our three viscosity models are -15, -30 and -37 mgal for the models with lower mantle viscosities of 10^{22}, 10^{23} and 5×10^{23} poise. (See fig. 9 in Peltier 1981.) In this case the former model must be rejected on the basis of its inability to fit the free air data. We are therefore forced to accept a value of the viscosity

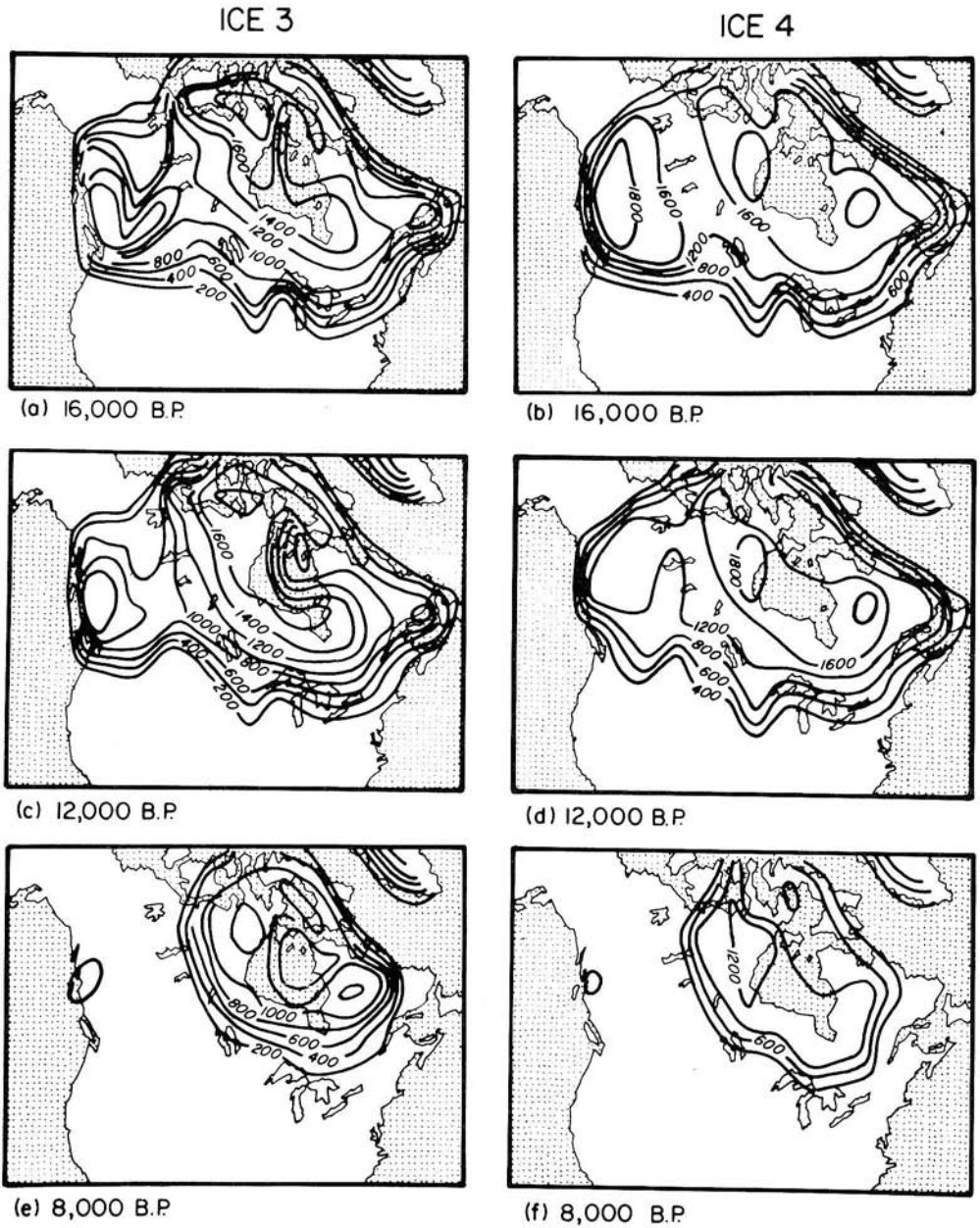

Figure 38. Same as Fig. 9 except that the deglaciation of ICE-3 is shown on the left side and the deglaciation of ICE-4 is shown on the right.

in the lower mantle of at least 10^{23} poise if the actual melting history of the ice sheets is closer to ICE-3 than it is to ICE-1(2). From Fig. 36, however, the fits to most of the RSL data under the ice sheet are not terribly satisfactory. What we will proceed to do in the next two subsections is to determine whether the difficulties with ICE-3 can be mitigrated by further refinement.

7.2 A REFINED VERSION OF THE BASIC ICE-3 HISTORY: ICE-4

We employed the same computationally interactive procedure for the refinement of ICE-3 as was employed with ICE-1 but use the Green's function for the model with 10^{23} poise lower mantle in order to optimize the modifications. We are clearly forced to do this by virtue of the inability of the uniform viscosity model to fit the free air gravity observations when we employ the ICE-3 chronology. A few time slices through the refined ICE-4 history determined in this way are shown in Fig. 38(b) which should be compared with the corresponding figure for the ICE-3 history.

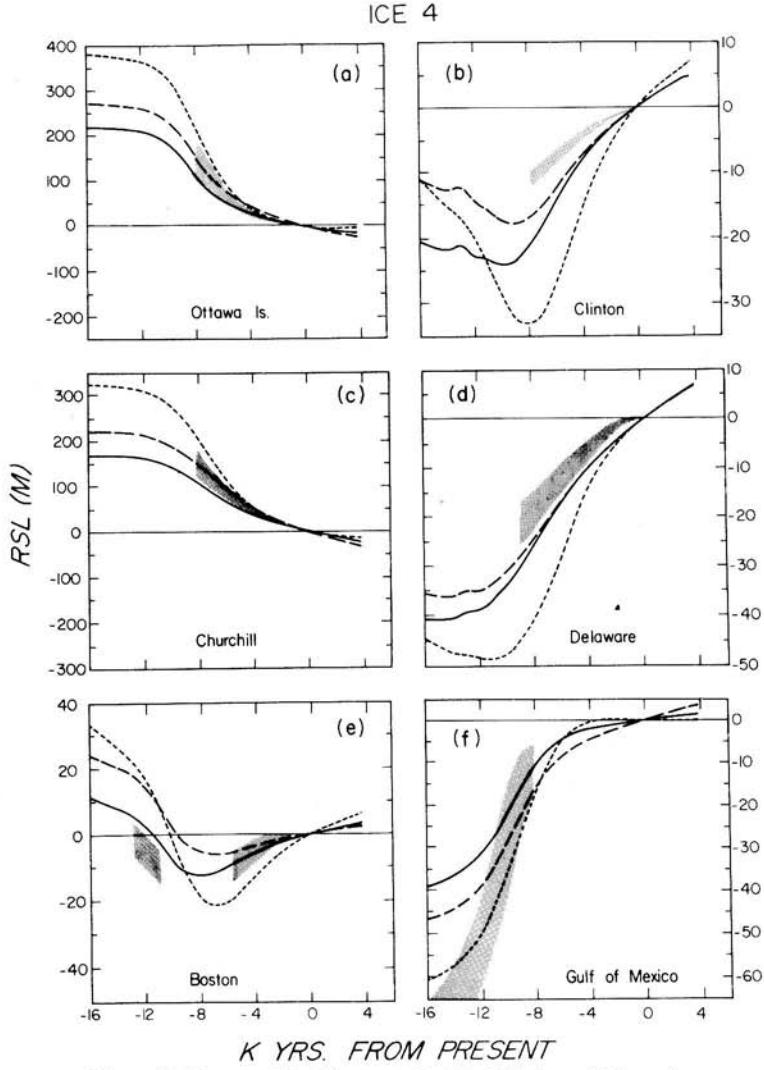

Figure 39. Same as Fig. 14 except that the ICE-4 model is used.

In order to test the ability of the RSL observations to discriminate between viscosity models we again generated sea-level histories using the gravitationally self-consistent theory described in Section 2 and in Fig. 39 we illustrate several of the results obtained. Inspection of these data shows, however, that when the ice thickness was adjusted to fit the observed relaxation amplitude the predicted present-day emergence rate is much higher than observed (e.g. Ottawa Islands). The only exceptions to this general rule are again found at some sites in the south-west corner of Hudson Bay (e.g. Churchill). The modification of the ice thickness inside the ice sheet does little to improve the fit of the 10^{23} poise lower mantle model to the data at sites near the ice margin like Prince Edward Island and Boston. As pointed out previously, this is because the data from such sites show clear evidence of peripheral bulge migration, which is inhibited by high lower mantle viscosity. At sites along the US east coast, the increase of ice thickness required to fit emergence amplitude under the ice now leads to an overestimate of submergence amplitude in this region. With the ICE-3(4) histories there is therefore a trade-off between the ability of the model to fit data under the ice and in the immediately peripheral region.

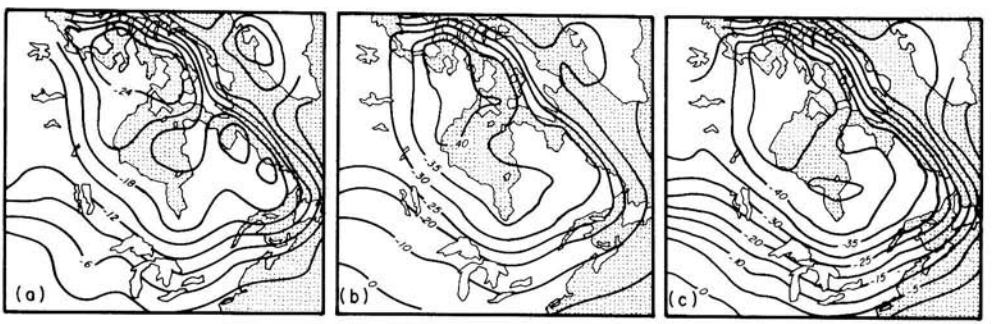

Figure 40. Predicted present-day gravity anomaly maps when ICE-4 chronology is used. (a) is for the uniform viscosity model, (b) and (c) are for the models with 10^{23} and 5×10^{23} poise in the lower mantle respectively.

The free air gravity maps predicted for the Laurentian region with the ICE-4 chronology are shown in Fig. 40. These are modified only slightly from those obtained with ICE-3 and the new peak anomalies are -18, -35 and -43 mgal for the models with 10^{22}, 10^{23} and 5×10^{23} poise lower mantle viscosities respectively. The former viscosity model is still strongly rejected by the free air data.

Summarizing the discussion of this subsection we are forced to conclude that ICE-3(4) (the thin ice sheet which melts late) requires high lower mantle viscosity in order to explain the free air gravity anomaly over Hudson Bay, but the fits of this model to the RSL data are markedly inferior to those obtained with the ICE-1(2) chronology. The *only* significant exceptions to this rule obtained at far field sites such as Recife, Brazil and South Island, New Zealand where the delayed melting chronology correctly predicts the emergence of beaches at 6 kBP rather than the 8 kBP predicted by ICE-1(2). Aside from the fundamental point that it does not match the observed disintegration isochrones is the fact that it does not contain sufficient ice to explain the net submergence at far field sites (e.g. Gulf of Mexico). The extent to which this objection might be met by invoking a contemporaneous melting event in addition to those associated with the decay of the Laurentia and Fennoscandia ice sheets is discussed in the next subsection.

7.3 LARGE-SCALE DEGLACIATION IN WEST ANTARCTICA: AN ADDITIONAL SOURCE OF MELTWATER

It has been reasonably well established in the past several years that significant melting of the Antarctic ice sheet quite likely occurred simultaneously with the disintegration of those over Canada and Fennoscandia. In this subsection we will investigate the way in which such a southern hemisphere deglaciation event would interact with those in the northern hemisphere and in particular will address the question of the impact of such an event upon the RSL record. The Antarctic melting chronology to be employed is that described by Hughes (1981), a smoothed version of which is illustrated through the time sections in Fig. 41. Although Clark & Lingle (1979) have previously investigated the effect of deglaciation in West Antarctica they did not melt the northern hemisphere ice sheets simultaneously. Our model differs from theirs mainly in this respect. The results to be discussed here were obtained by coupling the Hughes (1981) history with ICE-4. (Our Antarctic melting history is listed in Appendix B.)

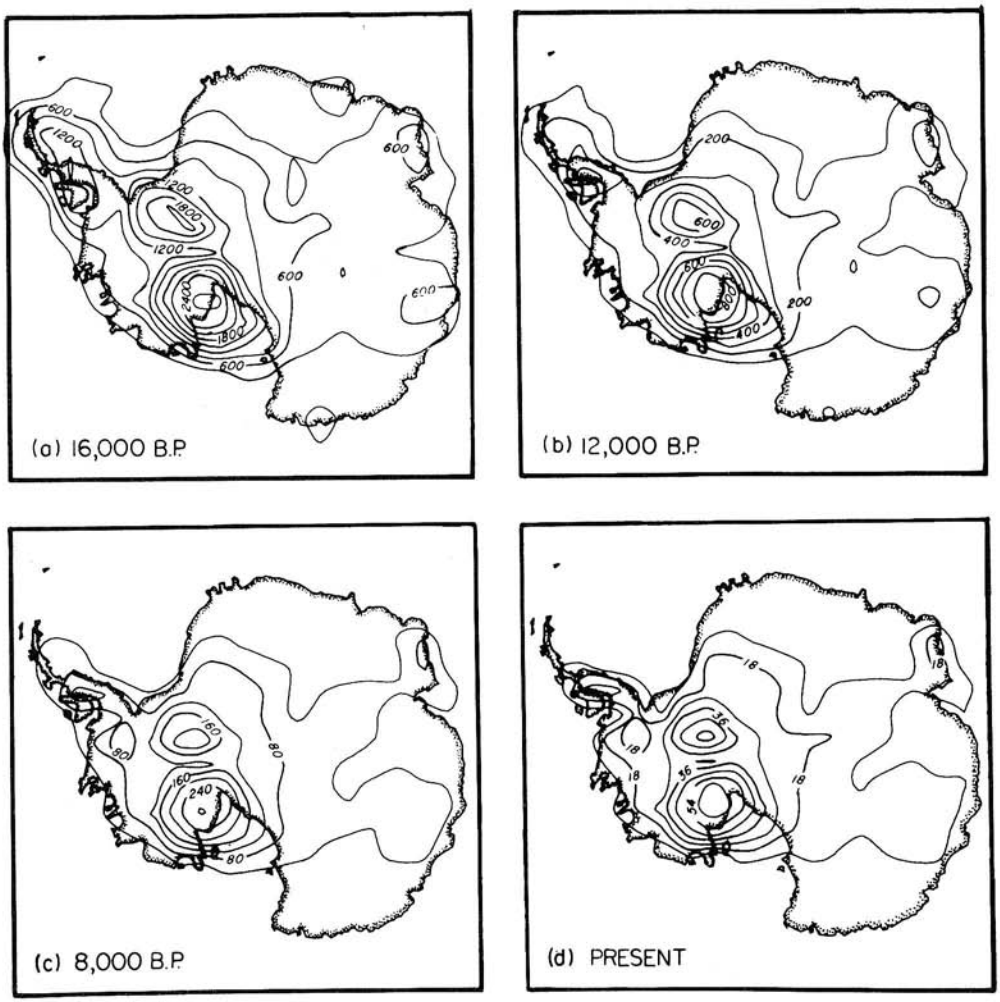

Figure 41. Four time slices showing the deglaciation of Antartic ice sheet. Contours are change of ice sheet thickness in metres (adapted from Hughes 1981).

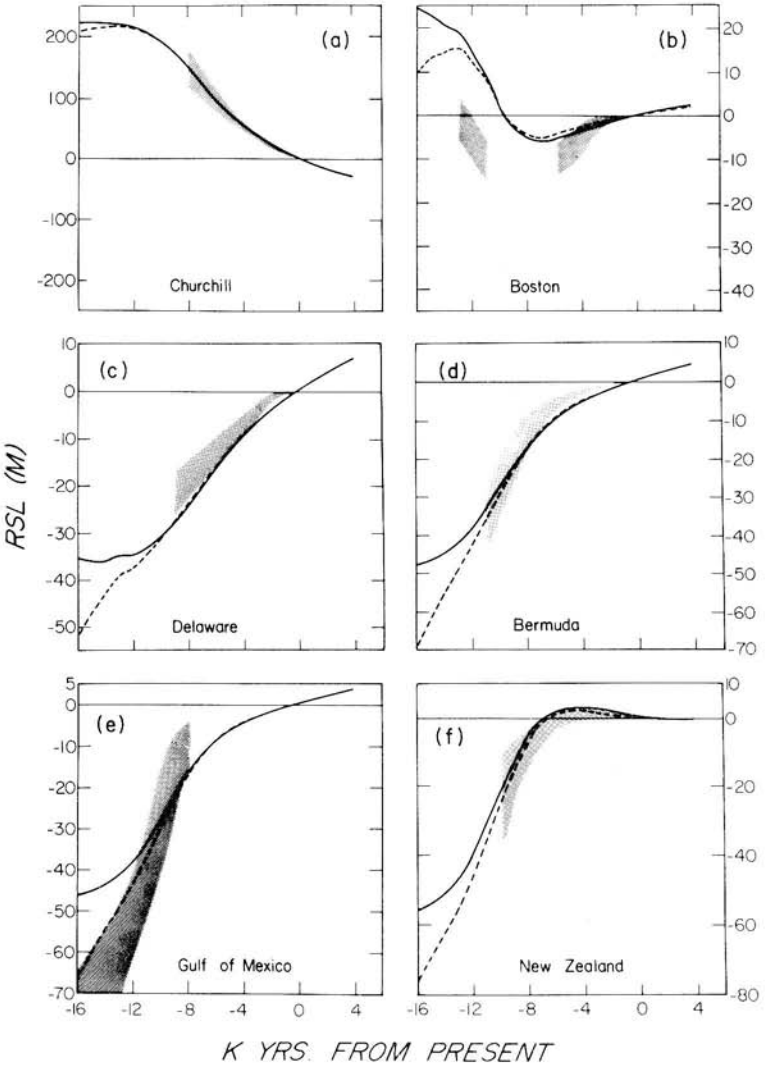

Figure 42. RSL curves for the 10^{23} poise lower mantle. The deglaciation of the northern hemisphere ice sheets are described by ICE-4. The solid curves do not include the melting of the Antarctica ice sheet whereas the dashed curves do.

Some relative sea-level curves forced by this deglaciation chronology are shown in Fig. 42 and were computed on the basis of the model with 10^{23} poise viscosity in the lower mantle. The short dashed curve on each plate is the RSL prediction for the deglaciation model which includes Antarctic melting while the solid curve is for ICE-4. These comparisons demonstrate that including the effect of melting in West Antarctica does not alter the RSL predictions substantially during the last 10 kyr. Only for times prior to this are the effects substantial with the increased submergence due to the extra meltwater (15–20 m of eustatic rise) apparent for sites like South Island, New Zealand, the Gulf of Mexico and Bermuda. We note that with the effect of melting in West Antarctica included, we have restored the fit of the model prediction to the Gulf of Mexico data.

For the sake of completeness of this subsection, we show in Fig. 43(a, b) the free air gravity anomaly over West Antarctica computed with the Hughes (1981) local deglaciation

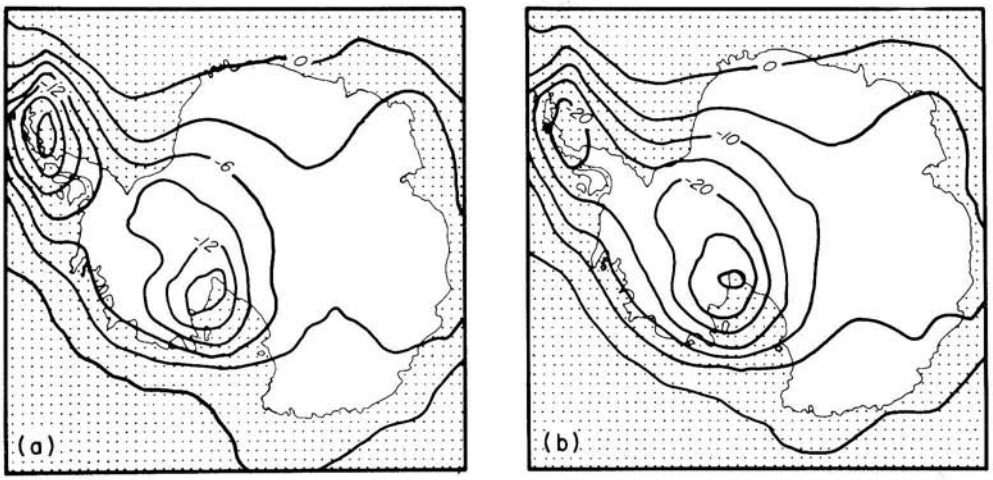

Figure 43. Predicted present-day gravity anomaly map over Antarctica. (a) is for the uniform viscosity model, (b) is for the model with 10^{23} poise lower mantle.

chronology. Fig. 43(a, b) was calculated using the Green's function for the models with 10^{22} and 10^{23} poise viscosity in the lower mantle respectively. Inspection of the figures show that the model with 10^{23} poise lower mantle predicts an anomaly of -25 mgal over the Ross Ice Shelf. The uniform mantle viscosity model predicts an anomaly of -15 mgal. It is interesting in this connection to note that the observed free air anomaly over the Ross Ice Shelf (Bentley, Robertson & Greischer 1978) is intermediate between these two predictions.

7.4 THE PLAUSIBILITY OF THE ICE-3(4) DISINTEGRATION HISTORY AND IMPLICATIONS OF THE CALCULATIONS DONE WITH IT

It may help for purposes of this summary to begin by listing the arguments for and against melting histories of the sort considered in this section which differ from those like ICE-1(2) in that the ice sheets themselves are taken to be thinner and to have disintegrated later in time. On the basis of the previous discussion this list is as follows:

For: (1) Far field RSL data shows raised beaches at 6 kBP whereas the ICE-1(2) histories predict these beaches to appear at 8 kBP.

Against: (1) Deglaciation chronologies like ICE-3(4) violate the radiocarbon controlled disintegration isochrones of Bryson *et al.* (1969).

(2) In order to fit the observed free air signal over Hudson Bay we require high lower mantle viscosity but such models do not fit the majority of RSL records from sites under the ice sheets.

In fact there is a third argument against the ICE-3(4) histories which completely rules them out even if one is willing to allow that there may be significant error in the timing of the Bryson *et al.* disintegration isochrones (which we are not). This argument makes use of the ideas developed in Section 6 concerning the impact of initial isostatic equilibrium upon model predictions of free air gravity and RSL data. In Fig. 44 we show the gravity anomaly at the centre of the parabolic disc load approximation to the Laurentian ice sheet as a function of lower mantle viscosity both including and excluding the effect of initial isostatic equilibrium. For the initial disequilibrium case the ice sheet prehistory was assumed to have the same saw-tooth form discussed previously with period 10^5 yr between successive inter-

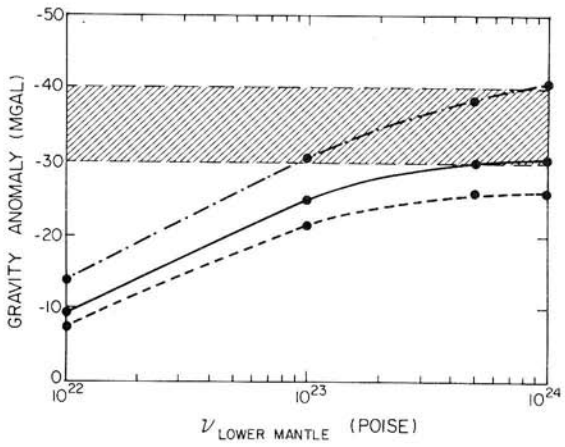

Figure 44. Same as Fig. 30 except that the parabolic ice sheet has central thickness of 1650 m.

glacials. Fig. 44 is therefore similar to Fig. 30, except that the ice sheet is thinner (1650 m) and melts 2 kyr later. Inspection of Fig. 44 shows that although the model with 10^{23} poise viscosity in the lower mantle can explain the magnitude of the observed free air anomaly if the system is initially in equilibrium, when the effect of initial disequilibrium is included this viscosity model predicts a peak gravity anomaly of only −25 mgal which is completely unacceptable. Therefore, in order to allow ICE-4 to fit the observed gravity anomaly we would, allowing for disequilibrium effects, have to increase the lower mantle viscosity to about 10^{24} poise. Since we have already shown that such models could not come anywhere close to satisfying the RSL data it is quite clear the models of the ICE-3(4) type are completely excluded by the data. This argument illustrates very well the power of the *combined* free air gravity and RSL data to constrain both the deglaciation chronology and the mantle viscosity profile. A summary of comparisons of theory and observation using the ICE-4 chronology is given in Table 2.

Given that the ICE-3(4) type chronologies are completely untenable we are still left with the problem of explaining why the ICE-1(2) histories are unable to explain the far field emergence data (i.e. the appearance of raised beaches at 6 kBP rather than the predicted 8 kBP). There is in fact a very simple explanation of these observations which does not require that the entire melting chronology be delayed by 2000 yr. This can be understood by simply noting that the amount of emergence observed at these sites is very small, on the order of 1–3 m. It should be quite clear that if the melting history did not end as abruptly as it does in ICE-1(2) at about 6 kBP but rather continued with a long 'tail' as it does in Shepard's (1963) observations, then the appearance of raised beaches in the far field will be delayed and the fit to the observations markedly improved.

8 Conclusions

This study has focused upon an attempt to determine the extent to which the relative sea-level record of the past 18 kyr and the observed free air gravity data over the main centres of Würm–Wisconsin deglaciation can be employed to constrain the viscosity of the Earth's mantle beneath 670 km depth. One of the most important results obtained in this work, and that discussed previously in Peltier (1981, 1982), is that it is possible to simultaneously reconcile both these types of data with a single mantle viscosity profile in terms of a model in which the deglaciation history is fixed by the constraints provided us by results from Quaternary

Table 2. Summary of agreement between prediction and observation when the ICE-4 chronology is employed as deglaciation history.

Viscosity model Lower mantle viscosity (P)		No. 1 10^{22}	No. 2 10^{23}	No. 3 5×10^{23}	Observed
I	Under the ice sheet				Ottawa Islands
	(a) Present-day rate of uplift (mm yr^{-1})	4.0	8.7	5.8	4.7
	(b) Height of 7 kBP beach (m)	151	110	78	140 ± 20
	(c) Curvature	√	×	×	√
II	Transition zone				Boston
	(a) Present-day rate of uplift (mm yr^{-1})	−2.1	−0.7	−0.9	−0.9
	(b) Height of 5 kBP beach (m)	−17	−9	−8	−8.0
	(c) Migration of forebulge	√	×	×	√
III	US East Coast				Delaware
	(a) Rate of uplift (mm yr^{-1})	−2.3	−2.0	−1.9	−0.5
	(b) Height of 8BP beach (m)	−41	−24	−26	−21
IV	Far field oldest raised beach (kBP)	6	6	6	6
V	Deglaciation isochrones	× (+2 kyr)	× (+2 kyr)	× (+2 kyr)	0.0
VI	Laurentia gravity (mgal) (Corrected for initial disequilibrium)	−18 (−13)	−35 (−30)	−43 (−34)	−37 ± 5

geomorphology. Prior to this work it was rather universally believed (e.g. Walcott 1980) that these two data sets were in a sense irreconcilable, with the RSL data appearing to demand more or less uniform viscosity in the mantle and the free air gravity data insisting equally strongly that viscosity of the lower mantle had to be high. Our work has completely resolved this difficulty. The reason our models are able to effect this reconciliation is that they are constructed on the basis of realistic viscoelastic models of the planet whose elastic structure (Lamé constants and density) is assumed fixed by the observations of body wave and free oscillation seismology. It turns out that the crucial ingredient in these models is the presence of the rather large internal density jump in the mantle associated with the phase transition at 670 km depth from the mineral spinel to a more closely packed mixture of perovskite plus magnesiowustite. This structural phase transition supports an extra mode of viscous gravitational relaxation whose relaxation time for fixed spherical harmonic degree is very much longer than that of the fundamental mode which carries most of the response. The short time-scale mode explains the short relaxation time-scale observed in the RSL data from sites under the Laurentide ice sheet while excitation of the long relaxation time mode explains why a significant gravity anomaly is still observed today (Peltier & Wu 1982).

In this paper we constructed a number of realistic viscoelastic models of the planet for different mantle viscosity profiles and fixed elastic structure. These viscoelastic earth models were employed in conjunction with realistic models of the Würm–Wisconsin deglaciation history to make predictions of RSL variations at many sites on the Earth's surface and of free air gravity anomaly maps over the main deglaciation centres. Using the melting chronology ICE-1(2) which fits the distintegration isochrones of Bryson *et al.* (1969) we were able to show that earth models with lower mantle viscosity of 10^{23} poise or greater could not fit

both the RSL and free air data simultaneously. Allowing for the effect of initial isostatic disequilibrium, using a deglaciation prehistory controlled by oxygen isotropic data from deep sea sedimentary cores, our preferred models have lower mantle viscosities in the range $2-5 \times 10^{22}$ poise with the increase across 670 km depth required to fit the free air gravity data.

We believe that the calculations discussed here have very clearly established the strength of the constraint upon lower mantle viscosity which is provided when both RSL and free air gravity data are employed. An important illustration of this fact was provided by our analysis of the ICE-3(4) chronology which established that irrespective of the mantle viscosity profile this model was completely untenable since it is impossible to simultaneously reconcile both data sets. The correct melting chronology is essentially that tabulated by Peltier & Andrews (1976) with the modifications which we have made to produce the refined history ICE-2 tabulated in Appendix A.

It is worth noting as a final point in this paper that although our calculations with the ICE-2 chronology did not include a West Antarctic melting event it is quite clear on the basis of results obtained in Section 7 that the effect of such an event upon our conclusions concerning the viscosity profile will be nil. It is interesting to note, furthermore, that our preferred viscosity models deduced from the analysis of northern hemisphere RSL and gravity data predict the free air anomaly over the Ross Ice Shelf observed by Bentley *et al.* (1978) when it is coupled with the disintegration history for West Antarctica given by Hughes (1981). This then clearly provides a useful independent check on the model and of its global validity.

References

Artyushkov, E. V., 1971. Rheological properties of the crust and upper mantle according to data on isostatic movements, *J. geophys. Res.*, **76**, 1376–1390.

Backus, G. E. & Gilbert, J. F., 1967. Numerical applications of a formalism for geophysical inverse problems, *Geophys. J. R. astr. Soc.*, **13**, 247–276.

Backus, G. E. & Gilbert, J. F., 1968. The resolving power of gross earth data, *Geophys. J. R. astr. Soc.*, **16**, 169–205.

Backus, G. E. & Gilbert, J. F., 1970. Uniqueness in the inversion of accurate gross earth data, *Phil. Trans. R. Soc. A*, **266**, 123–192.

Balling, N., 1980. The land uplift in Fennoscandia, gravity field anomalies and isostasy, in *Earth Rheology, Isostasy and Eustasy*, ed. Morner, N., Wiley, New York.

Bentley, C. R., Robertson, J. D. & Greischer, L. L., 1978. Isostatic gravity anomalies in the Ross Ice Shelf, Antarctica, preprint.

Bloom, A. L., 1980. Late Quaternary sea level change on South Pacific coasts, in *Earth Rheology, Isostasy and Eustasy*, ed. Mörner, N., Wiley, New York.

Broecker, W. S. & Van Donk, J., 1970. Insolation changes, Ice volumes, and the O^{18} record in deep-sea cores, *Rev. Geophys. Space Phys.*, **8**, 169–198.

Bryson, R. A., Wendland, W. M., Ives, J. D. & Andrews, J. T., 1969. Radiocarbon isochrons on the disintegration of Laurentide ice sheet, *Arctic Alpine Res.*, **1**, 1–14.

Cathles, L. M., 1975. *The Viscosity of the Earth's Mantle*, Princeton University Press, New Jersey.

Clark, J. A., 1980. The reconstruction of the Laurentide ice sheet of North America from sea level data: method and preliminary results, *J. geophys. Res.*, **85**, 4307–4323.

Clark, J. A., Farrell, W. E. & Peltier, W. R., 1978. Global changes in postglacial sea level: a numerical calculation, *Quat. Res.*, **9**, 265–287.

Clark, J. A. & Lingle, C. S., 1979. Predicted relative sea-level changes (18,000 years B.P. to present) caused by late glacial retreat of the Antarctic ice sheet, *Quat. Res.*, **11**, 279–298.

DePaolo, D. J. & Wasserburg, G. J., 1976. Nd isostopic variations and petrogenetic models, *Geophys. Res. Lett.*, **3**, 249–252.

DePaolo, D. J. & Wasserburg, G. J., 1979. Sm-Nd age of the Stillwater complex and the mantle evolution curve for neodynium, *Geochim. Cosmochim. Acta*, **43**, 999–1008.

Farrell, W. E., 1973. Earth tides, ocean tides and tidal loading, *Phil. Trans. R. Soc. A*, **274**, 253–259.

Farrell, W. E. & Clark, J. A., 1976. On postglacial sea level, *Geophys. J. R. astr. Soc.*, **46**, 647.

Faure, H., 1980. Late Cenozoic vertical movement in Africa, in *Earth Rheology, Isostasy and Eustasy*, ed. Mörner, N., Wiley, New York.

Gilbert, F. & Dziewonski, A., 1975. An application of normal mode theory to the retrieval of structural parameters and source mechanisms from seismic spectra, *Phil. Trans. R. Soc. A*, **278**, 187.

Godwin, H., 1962. Radio-carbon dating, *Nature*, **195**, 984.

Hays, J. D., Imbrie, J. & Shackleton, N. J., 1976. Variations in the Earth's orbit: pacemaker of the Ice Ages, *Science*, **194**, 1121.

Heiskanen, W. A. & Vening Meinesz, F. A., 1958. *The Earth and its Gravity Field*, McGraw-Hill, New York.

Honkasolo, T., 1964. On the use of gravity measurements for investigation of the land upheaveal in Fennoscandia, *Fennia*, **89**, 21–23.

Hughes, T. J., 1981. The last great ice sheets: a global view, in *The Last Great Ice Sheets*, eds Denton G. H. & Hughes, T. J., Wiley, New York.

Imbrie, J. & Kipp, B. G., 1971. A new micropaleontological method for quantitative paleoclimatology: application to a late Pleistocene Caribbean core, in *Late Cenozoic Glacial Ages*, ed. Turekian, K. K., Yale University Press, New Haven.

Jeanloz, R. & Richter, F. M., 1979. Convection, composition, and the thermal state of the lower mantle, *J. geophys. Res.*, **84**, 5497–5504.

Mao, H. K., Bell, P. M. & Yagi, T., 1979. Iron-magnesium fractionation model for the Earth, *Yb. Carnegie Instn Wash.*, **78**, 621–625.

Morner, N. (ed.), 1980. The Fennoscandian uplift: geological data and their geodynamic implication, in *Earth Rheology, Isostasy and Eustasy*, Wiley, New York.

Newman, W. S., Cinquemani, L. J., Pardi, R. R. & Marcus, L. F., 1980. Holocene delevelling of the United States' east coast, in *Earth Rheology, Isostasy and Eustasy*, ed. Morner, N., Wiley, New York.

Niskanen, E., 1939. On the upheaval of Land in Fennoscandia, *Ann. Acad. Sci. Fennicae A*, **53**, 1–30.

O'Connell, R. J., 1971. Pleistocene glaciation and the viscosity of the lower mantle, *Geophys. J. R. astr. Soc.*, **23**, 299–327.

O'Nions, R. K., Evensen, N. M. & Hamilton, P. J., 1979. Geochemical modelling of mantle differentiation and crustal growth, *J. geophys. Res.*, **84**, 6091–6101.

Paterson, W. S. B., 1972. Laurentide ice sheet: estimated volumes during late Wisconsin, *Rev. Geophys. Space Phys.*, **10**, 885–917.

Paterson, W. S. B., 1981. *The Physics of Glaciers*, Pergamon Press, Oxford.

Peltier, W. R., 1974. The impulse response of a Maxwell earth, *Rev. Geophys. Space Phys.*, **12**, 649–669.

Peltier, W. R., 1976. Glacial-isostatic adjustment II – the inverse problem, *Geophys. J. R. astr. Soc.*, **46**, 669–705.

Peltier, W. R., 1980. Mantle convection and viscosity, in *Physics of the Earth's Interior*, eds Dziewonski, A. M. & Boschi, E., North-Holland, New York.

Peltier, W. R., 1981. Ice age geodynamics, *Ann. Rev. Earth planet. Sci.*, **9**, 199–225.

Peltier, W. R., 1982. Dynamics of the ice age Earth, *Adv. Geophys.*, **24**, 1–146.

Peltier, W. R. & Andrews, J. T., 1976. Glacial-isostatic adjustment I – the forward problem, *Geophys. J. R. astr. Soc.*, **46**, 605–646.

Peltier, W. R., Farrell, W. E. & Clark, J. A., 1978. Glacial isostasy and relative sea level: a global finite element model, *Tectonophys.*, **50**, 81–110.

Peltier, W. R., Yuen, D. A. & Wu, P., 1980a. Postglacial rebound and transient rheology, *Geophys. Res. Lett.*, **7**, 733–736.

Peltier, W. R., Wu, P. & Yuen, D. A., 1980b. The viscosities of the Earth's mantle, in *Anelasticity in the Earth*, eds Stacey, F. D., Paterson, M. S. & Nicholas, A., American Geophysical Union, Washington, DC.

Peltier, W. R. & Wu, Patrick, 1982. Mantle phase transitions and the free air gravity anomalies over Fennoscandia and Laurentia, *Geophys. Res. Lett.*, **9**, 731–734.

Phillips, R. J. & Lambeck, K., 1980. Gravity fields of the terrestrial planets: long wavelength anomalies and tectonics, *Rev. Geophys. Space Phys.*, **18**, 27–76.

Platzman, G. W., 1971. Ocean tides and related waves, in *Mathematical Problems in the Geophysical Sciences 2: Inverse Problems, Dynamo Theory and Tides*, ed. Reid, W. H., American Mathematical Society, Providence, Rhode Island.

Sammis, C. G., Smith, J. C., Schubert, G. & Yuen, D. A., 1977. Viscosity–depth profile of the Earth's mantle: effects of polymorphic phase transitions, *J. geophys. Res.*, **82**, 3747–3761.

Shepard, F. P., 1963. Thirty-five thousand years of sea level, in *Essays in Marine Geology in Honor of K. O. Emergy.*, pp. 1–10, eds Clements, T., Stevenson, [illegible]. & Halmos, D., University of Southern California Press, Los Angeles.

Stuiver, M., 1971. Evidence for the variation of atmospheric C^{14} content in the late Quaternary, in *The Late Cenozoic Glacial Ages,* chapter 4, ed. Turekian, K. K., Yale University Press, New Haven.

Suess, H. E., 1970. Bristlecone pine calibration of the radio carbon timescale 5200 B.C. to the present, in *Radiocarbon Variations and Absolute Chronology, Proc. XII Nobel Symp,* Wiley, New York.

Van Bremmelen, R. W. & Berlage, H. P., 1935. Versuch Einer Mathmatischen Besonderer Berucksichtegung der Undationstheorie, *Beitr. Geophys.*, **43,** 19–55.

Walcott, R. I., 1970. Isostatic response to loading of the crust in Canada, *Can. J. Earth Sci.*, **7,** 716–727.

Walcott, R. I., 1972. Late Quaternary vertical movements in eastern north America: quantitative evidence of glacial-isostatic rebound, *Rev. Geophys. Space Phys.*, **10,** 849–884.

Walcott, R. I., 1980. Rheological models and observational data of glacio-isostatic rebound, in *Earth Rheology, Isostasy and Eustasy,* ed. Morner, N., Wiley, London.

Woodward, R. S., 1888. On the form and position of mean sea level, *Bull. U.S. geol. [illegible]*., **48,** 87–170.

Wu, P. & Peltier, W. R., 1982. Viscous gravitational relaxation, *Geophys. J. [illegible] Soc.*, **70,** 435–485.

Appendix A: ICE-2 load history

COLAT	ELONG	18	17	16	15	14	13	12	11	10	9	8	7	6	5	4
10.	265.	500	450	400	350	300	250	200	200	200	100	0	0	0	0	0
10.	270.	1000	1000	1000	963	925	888	850	825	800	800	800	850	900	700	500
10.	275.	2000	2000	2000	1813	1625	1438	1250	1225	1200	1200	1200	850	500	250	0
10.	280.	2000	1813	1625	1438	1250	1225	1200	1200	1200	1100	1000	750	50	50	50
10.	285.	1000	913	825	738	650	625	600	600	600	400	200	350	500	500	500
10.	295.	500	375	250	125	0	0	0	0	0	50	100	50	0	0	0
10.	300.	1000	1000	1000	1000	1000	750	500	500	500	700	900	700	500	500	500
10.	305.	1500	1487	1475	1462	1450	1325	1200	1200	1200	1325	1450	1225	1000	1000	1000
10.	310.	1500	1487	1475	1462	1450	1325	1200	1200	1200	1325	1450	1425	1400	1400	1400
10.	315.	2000	2000	2000	2000	2000	1975	1950	1950	1950	1950	1950	1975	2000	2000	2000
10.	320.	2200	2188	2175	2162	2150	2125	2100	2075	2050	2025	2000	1950	1900	1900	1900
10.	325.	2500	2487	2475	2462	2450	2425	2400	2375	2350	2300	2250	2200	2150	2150	2150
10.	330.	2200	2188	2175	2162	2150	2100	2050	2025	2000	1900	1800	1700	1600	1600	1600
10.	335.	1500	1475	1450	1425	1400	1350	1300	900	500	250	0	0	0	0	0
15.	250.	200	225	250	275	300	300	300	150	0	0	0	0	0	0	0
15.	255.	200	400	600	800	1000	1000	1000	500	0	0	0	0	0	0	0
15.	260.	1100	1100	1200	1300	1400	1400	1400	1400	1400	1100	850	575	300	0	0
15.	265.	1000	1125	1250	1375	1500	1500	1500	1050	600	300	0	0	0	0	0
15.	270.	1200	1200	1200	1200	1200	1200	1200	1160	1120	1000	875	750	500	350	350
15.	275.	1275	1250	1230	1220	1200	1130	1100	1100	1100	1100	1100	1100	700	500	500
15.	280.	250	250	250	250	250	240	200	165	130	100	70	40	0	0	0
15.	305.	1000	975	950	925	900	750	600	550	500	700	900	700	500	500	500
15.	310.	2000	2000	2000	2000	2000	2000	2000	1975	1950	1925	1900	1900	1900	1900	1900
15.	315.	2700	2700	2700	2700	2700	2700	2700	2675	2650	2650	2650	2675	2700	2700	2700
15.	320.	2800	2787	2775	2762	2750	2725	2700	2675	2650	2625	2600	2550	2500	2500	2500
15.	325.	3000	2987	2975	2962	2950	2925	2900	2875	2850	2825	2800	2750	2700	2700	2700
15.	330.	3000	2987	2975	2962	2950	2925	2900	2875	2850	2825	2800	2750	2700	2700	2700
15.	335.	2000	1987	1975	1962	1950	1925	1900	1850	1800	1650	1500	1400	1300	1300	1300
20.	235.	10	83	155	227	300	300	300	150	0	0	0	0	0	0	0
20.	240.	1200	1250	1300	1350	1400	1400	1400	700	0	0	0	0	0	0	0
20.	245.	1800	1700	1600	1500	1400	1400	1400	700	0	0	0	0	0	0	0
20.	250.	1900	1825	1750	1675	1600	1600	1600	950	300	150	0	0	0	0	0
20.	255.	2100	2075	2050	2025	2000	2000	2000	1500	1000	500	0	0	0	0	0
20.	260.	2000	2000	2000	2000	1750	1750	1650	1225	800	400	0	0	0	0	0
20.	265.	1100	1085	1075	1065	1050	900	850	650	450	150	0	0	0	0	0
20.	270.	1100	1045	1037	1030	1025	850	825	588	350	150	0	0	0	0	0
20.	275.	1900	1900	1900	1900	1900	1900	1900	1550	1200	750	300	150	0	0	0
20.	280.	1850	1850	1850	1850	1850	1850	1850	1875	1900	1650	1475	1100	400	0	0
20.	285.	1600	1550	1500	1450	1400	1400	1400	1400	1400	1075	930	864	800	800	800
20.	290.	600	650	700	750	800	800	800	750	700	575	550	450	225	125	10
20.	305.	400	400	400	400	400	200	0	0	0	0	0	0	0	0	0
20.	310.	2000	2000	2000	2000	2000	1400	800	800	800	900	1000	600	200	200	200
20.	315.	2600	2600	2600	2600	2600	2650	2700	2675	2650	2575	2500	2550	2600	2600	2600
20.	320.	3200	3188	3175	3162	3150	3125	3100	3075	3050	3025	3000	3000	3000	3000	3000
20.	325.	3500	3487	3475	3462	3450	3375	3300	3250	3200	3150	3100	3075	3050	3050	3050
20.	330.	2000	1987	1975	1962	1950	1925	1900	1750	1600	1400	1200	1000	800	800	800
20.	335.	200	175	150	125	100	50	0	0	0	0	0	0	0	0	0

Appendix A – *continued*

COLAT	ELONG	18	17	16	15	14	13	12	11	10	9	8	7	6	5	4
25.	230.	1000	875	750	625	500	400	300	150	0	0	0	0	0	0	0
25.	235.	1200	1287	1375	1462	1550	1525	1500	750	0	0	0	0	0	0	0
25.	240.	1800	1813	1825	1837	1850	1825	1600	800	0	0	0	0	0	0	0
25.	245.	2100	2075	2050	2025	2000	1900	1650	850	50	25	0	0	0	0	0
25.	250.	2300	2450	2400	2425	2500	2350	1900	1500	1100	500	0	0	0	0	0
25.	255.	2600	2650	2700	2750	2800	2625	2250	1775	1300	600	0	0	0	0	0
25.	260.	2700	2725	2850	2925	2900	2875	2450	2000	1550	1100	1000	500	0	0	0
25.	265.	2800	2800	2850	2850	2850	2850	2800	2400	2000	1700	1400	1050	650	500	500
25.	270.	2600	2550	2500	2400	2250	2100	1800	1625	1450	900	500	250	0	0	0
25.	275.	1700	1665	1650	1635	1620	1605	1590	1395	1200	800	375	195	0	0	0
25.	280.	1900	1900	1900	1900	1900	1900	1900	1550	1200	750	300	150	0	0	0
25.	285.	1950	1975	2000	2025	2050	2050	2050	1925	1800	1500	1000	450	0	0	0
25.	290.	1000	1125	1250	1375	1500	1500	1500	1300	1100	1050	1000	750	500	500	500
25.	310.	1800	1800	1800	1800	1800	1400	1000	1000	1000	1000	1000	750	500	500	500
25.	315.	2700	2700	2700	2700	2700	2675	2650	2650	2650	2625	2600	2600	2600	2600	2600
30.	225.	1000	975	950	925	900	450	0	0	0	0	0	0	0	0	0
30.	230.	1000	975	950	925	900	850	800	400	0	0	0	0	0	0	0
30.	235.	1000	975	950	925	900	450	0	0	0	0	0	0	0	0	0
30.	240.	1200	1250	1300	1350	1400	1350	1300	650	0	0	0	0	0	0	0
30.	245.	2000	1962	1925	1887	1850	1825	1600	800	0	0	0	0	0	0	0
30.	250.	2100	2150	2100	2250	2200	1900	1650	825	0	0	0	0	0	0	0
30.	255.	2400	2475	2500	2600	2600	2350	1900	1500	1100	500	200	200	0	0	0
30.	260.	2800	2862	2900	2875	2850	2625	2250	1775	1300	600	400	250	0	0	0
30.	265.	3250	3300	3350	3400	3150	2900	2500	2075	1650	1300	650	350	0	0	0
30.	270.	3500	3475	3450	3425	3400	3200	2650	2050	1450	750	475	270	0	0	0
30.	275.	3400	3250	3100	2950	2800	2650	2500	1925	1350	650	350	200	0	0	0
30.	280.	2600	2500	2400	2300	2200	2100	1800	1450	1100	600	250	150	0	0	0
30.	285.	2450	2460	2325	2188	2050	2075	2100	1750	1400	1000	500	220	0	0	0
30.	290.	1800	1725	1650	1575	1500	1550	1600	1450	1300	950	400	300	0	0	0
30.	295.	500	575	650	725	800	700	600	650	700	500	300	150	0	0	0
30.	315.	200	175	150	125	100	50	0	0	0	0	0	0	0	0	0
35.	230.	1500	1475	1450	1425	1400	1200	1000	750	500	250	0	0	0	0	0
35.	235.	1500	1475	1450	1425	1400	1200	1000	500	0	0	0	0	0	0	0
35.	240.	1000	1000	1000	1000	1000	500	0	0	0	0	0	0	0	0	0
35.	245.	1600	1450	1300	1150	1000	600	200	100	0	0	0	0	0	0	0
35.	250.	2000	1950	1900	1850	1800	1400	1000	500	0	0	0	0	0	0	0
35.	255.	2000	2050	2100	2150	2200	1750	1400	700	0	0	0	0	0	0	0
35.	260.	2000	2100	2200	2300	2400	1900	1650	1300	950	300	200	100	0	0	0
35.	265.	2400	2500	2550	2620	2675	2350	1900	1550	1200	550	200	200	0	0	0
35.	270.	2800	2862	2900	2875	2850	2625	2200	1750	1300	600	400	250	0	0	0
35.	275.	3100	3200	3300	3400	3100	2800	2450	1925	1400	700	450	250	0	0	0
35.	280.	3475	3450	3425	3400	3325	3250	2600	2025	1450	650	450	200	0	0	0
35.	285.	3100	3075	3050	3025	3025	3025	2600	2025	1450	650	470	220	0	0	0
35.	290.	2800	2850	2100	2150	2200	2350	2500	2000	1500	750	500	500	500	500	500
35.	295.	1400	1400	1400	1400	1400	1575	1750	1500	1250	600	140	70	0	0	0
35.	300.	600	600	600	600	600	600	600	600	600	500	300	0	0	0	0
40.	235.	1500	1450	1400	1350	1300	650	0	0	0	0	0	0	0	0	0
40.	240.	1500	1375	1250	1125	1000	1000	1000	500	0	0	0	0	0	0	0
40.	245.	1000	950	900	850	800	400	0	0	0	0	0	0	0	0	0
40.	250.	800	600	400	200	0	0	0	0	0	0	0	0	0	0	0
40.	255.	900	750	600	450	300	150	0	0	0	0	0	0	0	0	0
40.	260.	1400	1350	1300	1250	1200	600	0	0	0	0	0	0	0	0	0
40.	265.	1800	1825	1850	1875	1900	950	0	0	0	0	0	0	0	0	0
40.	270.	2000	2050	2100	2150	2400	1900	1650	975	300	150	0	0	0	0	0
40.	275.	2400	2475	2550	2625	2600	2350	1900	1500	1100	500	0	0	0	0	0
40.	280.	2800	2862	2900	2875	2850	2625	2200	1750	1300	600	400	200	0	0	0
40.	285.	2600	2612	2825	2837	2850	2475	2100	1650	1200	600	0	0	0	0	0
40.	290.	1600	1500	1400	1320	1230	885	540	480	420	210	0	0	0	0	0
40.	295.	1800	1725	1625	1575	1500	750	0	0	0	0	0	0	0	0	0
40.	300.	1700	1600	1500	1400	1300	650	0	0	0	0	0	0	0	0	0
40.	305.	600	600	600	600	600	600	600	600	600	500	300	0	0	0	0
45.	265.	1200	1150	1100	1050	1000	500	0	0	0	0	0	0	0	0	0
45.	270.	0	50	100	150	200	100	0	0	0	0	0	0	0	0	0
45.	275.	1900	1650	1400	1150	900	550	200	100	0	0	0	0	0	0	0
45.	280.	1900	1775	1650	1525	1400	1150	900	450	0	0	0	0	0	0	0
45.	285.	1900	1775	1650	1525	1400	800	200	100	0	0	0	0	0	0	0
45.	290.	1100	950	875	800	720	600	480	240	0	0	0	0	0	0	0
45.	295.	0	0	0	0	0	0	0	0	0	0	0	0	0	0	0
50.	275.	300	225	150	75	0	0	0	0	0	0	0	0	0	0	0
50.	280.	300	225	150	75	0	0	0	0	0	0	0	0	0	0	0
10.	15.	900	875	850	825	800	650	500	350	200	100	0	0	0	0	0
10.	20.	900	875	850	825	800	650	500	350	200	100	0	0	0	0	0
10.	25.	900	875	850	825	800	650	500	350	200	100	0	0	0	0	0
10.	40.	800	800	800	800	800	400	0	0	0	0	0	0	0	0	0
10.	45.	500	425	350	275	200	200	200	150	100	50	0	0	0	0	0
10.	50.	500	425	350	275	200	200	200	150	100	50	0	0	0	0	0
10.	55.	500	425	350	275	200	200	200	150	100	50	0	0	0	0	0

Appendix A – *continued*

COLAT	ELONG	18	17	16	15	14	13	12	11	10	9	8	7	6	5	4
10.	60.	500	425	350	275	200	200	200	150	100	50	0	0	0	0	0
10.	65.	100	88	75	63	50	25	0	0	0	0	0	0	0	0	0
15.	65.	500	475	450	425	400	350	300	200	100	50	0	0	0	0	0
20.	20.	600	525	450	375	300	150	0	0	0	0	0	0	0	0	0
20.	25.	1125	1106	1087	1069	1050	825	600	300	0	0	0	0	0	0	0
20.	30.	1125	1106	1087	1069	1050	525	0	0	0	0	0	0	0	0	0
20.	35.	375	319	262	206	150	75	0	0	0	0	0	0	0	0	0
20.	65.	500	475	450	425	400	300	200	100	0	0	0	0	0	0	0
25.	340.	1500	1425	1350	1275	1200	1050	900	700	500	250	0	0	0	0	0
25.	345.	1000	925	850	775	700	350	0	0	0	0	0	0	0	0	0
25.	15.	1350	1331	1312	1294	1275	1012	750	675	600	300	0	0	0	0	0
25.	20.	2175	2146	2119	2090	2062	1875	1687	1519	1350	675	0	0	0	0	0
25.	25.	2250	2221	2194	2165	2137	1931	1725	1575	1425	712	0	0	0	0	0
25.	30.	2175	2119	2062	2006	1950	1856	1762	1069	375	187	0	0	0	0	0
25.	35.	1875	1837	1800	1762	1725	1725	1725	863	0	0	0	0	0	0	0
25.	40.	1125	1069	1012	956	900	637	375	188	0	0	0	0	0	0	0
25.	45.	150	112	75	37	0	0	0	0	0	0	0	0	0	0	0
25.	65.	100	75	50	25	0	0	0	0	0	0	0	0	0	0	0
30.	5.	600	487	375	262	150	75	0	0	0	0	0	0	0	0	0
30.	10.	1125	1087	1050	1012	975	862	750	713	675	337	0	0	0	0	0
30.	15.	1500	1462	1425	1387	1350	1312	1275	900	525	262	0	0	0	0	0
30.	20.	2100	2044	1987	1931	1875	1650	1425	731	37	19	0	0	0	0	0
30.	25.	2100	2062	2025	1987	1950	1725	1500	750	0	0	0	0	0	0	0
30.	30.	2100	2062	2025	1987	1950	1162	375	188	0	0	0	0	0	0	0
30.	35.	900	685	469	253	37	56	75	38	0	0	0	0	0	0	0
30.	40.	37	28	19	10	0	0	0	0	0	0	0	0	0	0	0
35.	355.	1000	950	900	850	800	525	250	125	0	0	0	0	0	0	0
35.	10.	375	281	187	94	0	0	0	0	0	0	0	0	0	0	0
35.	15.	900	806	712	619	525	262	0	0	0	0	0	0	0	0	0
35.	20.	975	900	825	750	675	337	0	0	0	0	0	0	0	0	0
35.	25.	600	450	300	150	0	0	0	0	0	0	0	0	0	0	0
10.	30.	0	0	0	0	0	0	0	0	0	0	0	0	0	0	0
10.	35.	0	0	0	0	0	0	0	0	0	0	0	0	0	0	0
15.	15.	0	0	0	0	0	0	0	0	0	0	0	0	0	0	0
15.	20.	0	0	0	0	0	0	0	0	0	0	0	0	0	0	0
15.	25.	0	0	0	0	0	0	0	0	0	0	0	0	0	0	0
15.	30.	0	0	0	0	0	0	0	0	0	0	0	0	0	0	0
15.	35.	0	0	0	0	0	0	0	0	0	0	0	0	0	0	0
15.	40.	0	0	0	0	0	0	0	0	0	0	0	0	0	0	0
15.	45.	0	0	0	0	0	0	0	0	0	0	0	0	0	0	0
15.	50.	0	0	0	0	0	0	0	0	0	0	0	0	0	0	0
15.	55.	0	0	0	0	0	0	0	0	0	0	0	0	0	0	0
15.	60.	0	0	0	0	0	0	0	0	0	0	0	0	0	0	0
20.	15.	0	0	0	0	0	0	0	0	0	0	0	0	0	0	0
20.	45.	0	0	0	0	0	0	0	0	0	0	0	0	0	0	0
20.	50.	0	0	0	0	0	0	0	0	0	0	0	0	0	0	0
20.	55.	0	0	0	0	0	0	0	0	0	0	0	0	0	0	0
25.	50.	0	0	0	0	0	0	0	0	0	0	0	0	0	0	0
25.	55.	0	0	0	0	0	0	0	0	0	0	0	0	0	0	0
25.	60.	0	0	0	0	0	0	0	0	0	0	0	0	0	0	0

Appendix B: Antarctic ice history

COLAT.	ELONG	18	17	16	15	14	13	12	11	10	9	8	7	6	5	4
159.	165.	138	91	60	39	26	17	11	7	5	3	2	1	0	0	0
162.	165.	188	142	108	82	62	47	35	27	20	15	12	9	7	5	5
164.	165.	188	82	35	15	7	3	0	0	0	0	0	0	0	0	0
166.	165.	308	177	101	58	33	19	11	6	4	0	0	0	0	0	0
168.	165.	1038	684	451	297	196	129	85	56	37	24	16	11	0	0	0
170.	165.	1438	1030	738	529	379	272	195	139	100	72	51	37	26	19	19
172.	170.	1688	1235	903	661	484	354	259	189	139	101	74	54	40	29	29
173.	165.	1438	1089	825	625	473	359	272	206	156	118	89	68	51	39	39
174.	165.	938	710	538	408	309	234	177	134	102	77	58	44	33	25	25
174.	175.	1438	1089	825	625	473	359	272	206	156	118	89	68	51	39	39
173.	175.	1938	1444	1076	802	598	455	332	247	184	137	102	76	57	42	42
170.	175.	1438	1030	738	529	379	272	195	139	100	72	51	37	26	19	19
168.	175.	688	453	299	197	130	86	56	37	25	16	11	7	0	0	0
166.	175.	238	136	78	45	26	15	8	5	3	0	0	0	0	0	0
164.	175.	58	25	11	5	2	1	0	0	0	0	0	0	0	0	0
162.	175.	10	2	0	0	0	0	0	0	0	0	0	0	0	0	0
164.	185.	10	4	2	1	0	0	0	0	0	0	0	0	0	0	0
166.	185.	58	33	19	11	6	4	2	1	1	0	0	0	0	0	0
168.	185.	1038	684	451	297	196	129	85	56	37	24	16	11	0	0	0

Appendix B – *continued*

COLAT.	ELONG	18	17	16	15	14	13	12	11	10	9	8	7	6	5	4
170.	185.	1938	1389	995	713	511	366	262	188	135	96	69	50	35	25	25
172.	190.	2538	1857	1358	994	727	532	389	285	208	152	112	82	60	44	44
173.	185.	2438	1817	1354	1009	752	560	417	311	232	173	129	96	71	53	53
174.	185.	2138	1593	1187	885	659	491	366	273	203	151	113	84	63	47	47
174.	195.	2558	1906	1420	1058	789	588	438	326	243	181	135	101	75	56	56
173.	195.	2788	2077	1548	1154	860	641	477	356	265	198	147	110	82	61	61
170.	195.	2188	1568	1123	805	577	413	296	212	152	109	78	56	40	29	29
168.	195.	1188	783	516	340	224	148	98	64	42	28	18	12	0	0	0
166.	195.	188	108	62	35	20	12	7	4	2	0	0	0	0	0	0
166.	205.	188	108	62	35	20	12	7	4	2	0	0	0	0	0	0
168.	205.	1188	783	516	340	224	148	98	64	42	28	18	12	0	0	0
170.	205.	2438	1747	1252	897	643	460	330	236	169	121	87	62	45	32	32
172.	210.	2938	2149	1573	1150	842	616	451	330	241	176	129	94	69	51	51
173.	205.	2938	2189	1631	1216	906	675	503	375	279	208	155	116	86	64	64
174.	205.	2733	2040	1520	1133	844	629	469	349	260	194	145	108	80	60	60
174.	215.	2688	2036	1542	1168	885	670	508	385	291	221	167	127	96	73	73
173.	215.	2938	2225	1686	1277	967	733	555	420	318	241	183	138	105	79	79
170.	215.	2538	1922	1456	1103	835	633	479	363	275	208	158	120	91	69	69
168.	215.	938	710	538	408	309	234	177	134	102	77	58	44	33	24	24
166.	215.	338	223	147	97	64	42	28	18	12	8	5	3	0	0	0
165.	225.	308	203	134	88	58	38	25	17	11	7	5	3	0	0	0
167.	226.	538	407	309	234	177	134	102	77	58	44	33	25	19	15	15
170.	226.	2138	1619	1227	929	704	533	404	306	232	175	133	101	76	58	58
172.	226.	2558	1937	1468	1112	842	638	483	366	277	210	159	120	91	69	69
174.	226.	2688	2036	1542	1168	885	670	508	385	291	221	167	127	96	73	73
174.	239.	2438	1847	1399	1059	803	608	460	349	264	200	152	115	87	66	66
172.	239.	2308	1748	1324	1003	760	575	436	330	250	189	143	109	82	62	62
170.	239.	1688	1278	968	734	556	421	319	241	183	139	105	79	60	46	46
167.	239.	688	521	395	299	226	172	130	98	75	56	43	32	25	19	19
165.	234.	338	256	194	147	111	84	64	48	37	28	21	16	12	9	9
163.	234.	188	124	82	54	35	23	15	10	7	4	3	2	0	0	0
163.	241.	188	124	82	54	35	23	15	10	7	4	3	2	0	0	0
165.	241.	438	332	251	190	144	109	83	63	47	36	27	21	16	12	12
162.	249.	150	100	60	35	20	10	7	4	1	1	1	0	0	0	0
165.	249.	688	521	395	299	226	172	130	98	75	56	43	32	25	19	19
162.	256.	238	157	103	68	45	30	20	13	8	6	4	2	0	0	0
165.	256.	688	453	299	197	130	86	56	37	25	16	11	7	0	0	0
167.	251.	938	710	538	408	309	234	177	134	102	77	58	44	33	25	25
170.	251.	738	559	423	321	243	184	139	106	80	61	46	35	26	20	20
172.	251.	1538	1165	882	668	506	383	290	220	167	126	96	72	55	42	42
174.	251.	1938	1468	1112	842	638	483	366	277	210	159	120	91	69	52	52
174.	264.	938	710	538	408	309	234	177	134	102	77	58	44	33	25	25
172.	264.	938	710	538	408	309	234	177	134	102	77	58	44	33	25	25
170.	264.	938	710	538	408	309	234	177	134	102	77	58	44	33	25	25
167.	264.	838	635	481	364	276	209	158	120	91	69	52	39	30	23	23
164.	265.	538	407	309	234	177	134	102	77	58	44	33	19	15	15	15
161.	265.	238	157	103	68	45	30	20	13	8	6	4	2	0	0	0
161.	275.	438	289	190	125	83	55	36	24	16	10	7	4	0	0	0
164.	273.	438	332	251	190	144	109	83	63	47	36	27	21	16	12	12
164.	278.	938	710	538	408	309	234	177	134	102	77	58	44	33	25	25
166.	275.	558	423	320	242	184	139	105	80	60	46	35	26	20	15	15
168.	275.	808	612	464	351	266	201	153	116	88	66	50	38	29	22	22
170.	275.	1188	900	682	516	391	296	224	170	129	98	74	56	42	32	32
172.	280.	1738	1316	997	755	572	433	328	249	188	143	108	82	62	47	47
174.	278.	1438	1089	825	625	473	359	272	206	156	118	89	68	51	39	39
174.	293.	2338	1771	1341	1016	770	583	442	334	253	192	145	110	83	63	63
172.	295.	2238	1695	1284	973	737	558	423	320	243	184	139	105	80	60	60
171.	295.	1938	1418	1037	759	555	406	297	217	159	116	85	62	46	33	33
170.	285.	1938	1389	995	713	511	366	262	188	135	96	69	50	35	25	25
168.	285.	1188	783	516	340	224	148	98	64	42	28	18	12	0	0	0
166.	285.	558	423	320	242	184	139	105	80	60	46	35	26	20	15	15
164.	288.	1188	783	516	340	224	148	98	64	42	28	18	12	0	0	0
164.	283.	1188	783	516	340	224	148	98	64	42	28	18	12	0	0	0
162.	288.	1788	1179	777	512	338	223	147	97	64	42	28	18	0	0	0
162.	283.	1438	948	625	412	272	179	118	78	51	34	22	15	0	0	0
159.	285.	688	453	299	197	130	86	56	37	25	16	11	7	0	0	0
155.	290.	558	368	242	160	105	69	46	30	20	13	9	6	0	0	0
158.	293.	688	521	395	299	226	172	130	98	75	56	43	32	25	19	19
160.	293.	1438	1089	825	625	473	359	272	206	156	118	89	68	51	39	39
162.	293.	1438	1089	825	625	473	359	272	206	156	118	89	68	51	39	39
164.	293.	738	559	423	321	243	184	139	106	80	61	46	35	26	20	20
162.	298.	938	710	538	408	309	234	177	134	102	77	58	44	33	25	25
164.	298.	938	710	538	408	309	234	177	134	102	77	58	44	33	25	25
166.	295.	1188	900	682	516	391	296	224	170	129	98	74	56	42	32	32
168.	295.	1688	1113	734	484	319	210	139	91	60	40	26	17	0	0	0
170.	295.	1938	1389	995	713	511	366	262	188	135	96	69	50	35	25	25
174.	310.	1938	1468	1112	842	638	483	366	277	210	159	120	91	69	52	52
172.	305.	2438	1784	1305	955	698	511	374	274	200	146	107	78	57	42	42

Appendix B – *continued*

COLAT.	ELONG	18	17	16	15	14	13	12	11	10	9	8	7	6	5	4
171.	305.	2238	1637	1198	876	641	469	343	251	184	134	98	72	53	39	39
170.	305.	1938	1389	995	713	511	366	262	188	135	96	69	50	35	25	25
168.	305.	1538	1014	668	441	290	191	126	83	55	36	24	16	0	0	0
166.	305.	938	538	309	177	102	58	33	19	11	0	0	0	0	0	0
163.	305.	638	277	120	52	23	10	0	0	0	0	0	0	0	0	0
159.	300.	1588	1047	690	455	300	198	130	86	57	37	25	16	0	0	0
156.	298.	1218	803	529	349	230	152	100	66	43	29	19	12	0	0	0
154.	298.	938	618	408	269	177	117	77	51	33	22	15	10	0	0	0
152.	298.	438	289	190	125	83	55	36	24	16	10	7	4	0	0	0
153.	305.	688	453	299	197	130	86	56	37	25	16	11	7	0	0	0
156.	303.	1438	948	625	412	272	179	118	78	51	34	22	15	0	0	0
164.	315.	138	60	26	11	5	2	0	0	0	0	0	0	0	0	0
166.	315.	438	251	144	83	47	27	16	9	5	0	0	0	0	0	0
168.	315.	938	618	408	269	177	117	77	51	33	22	15	10	0	0	0
170.	315.	1188	851	610	437	313	224	161	115	83	59	42	30	22	16	16
171.	315.	1188	869	636	465	340	249	182	133	98	71	52	38	28	20	20
172.	315.	1188	900	682	516	391	296	224	170	129	98	74	56	42	32	32
174.	330.	938	710	538	408	309	234	177	134	102	77	58	44	33	25	25
172.	330.	938	710	538	408	309	234	177	134	102	77	58	44	33	25	25
170.	325.	938	672	482	345	247	177	127	91	65	47	33	24	17	12	12
168.	325.	688	453	299	197	130	86	56	37	25	16	11	7	0	0	0
170.	335.	938	710	538	408	309	234	177	134	102	77	58	44	33	25	25
168.	335.	938	710	538	408	309	234	177	134	102	77	58	44	33	25	25
165.	330.	188	108	62	35	20	12	7	4	2	0	0	0	0	0	0
162.	350.	238	157	103	68	45	30	20	13	8	6	4	2	0	0	0
167.	350.	388	294	223	169	128	97	73	55	42	32	24	18	14	10	10
170.	350.	838	635	481	364	276	209	158	120	91	69	52	39	30	23	23
173.	350.	938	710	538	408	309	234	177	134	102	77	58	44	33	25	25
172.	15.	838	635	481	364	276	209	158	120	91	69	52	39	30	23	23
167.	15.	188	142	108	82	62	47	35	27	20	15	12	9	7	5	5
162.	8.	38	29	22	16	12	9	7	5	4	3	2	1	1	1	1
162.	23.	338	256	194	147	111	84	64	48	37	28	21	16	12	9	9
160.	35.	438	289	190	125	83	55	36	24	16	10	7	4	0	0	0
164.	38.	188	142	108	82	62	47	35	27	20	15	12	9	7	5	5
168.	38.	238	180	136	103	78	59	45	34	26	20	15	11	8	6	6
164.	99.	538	407	309	234	177	134	102	77	58	44	33	25	19	15	15
168.	99.	188	142	108	82	62	47	35	27	20	15	12	9	7	5	5
172.	45.	138	104	79	60	45	34	26	20	15	11	9	6	5	4	4
168.	53.	438	332	251	190	144	109	83	63	47	36	27	21	16	12	12
164.	53.	438	289	190	125	83	55	36	24	16	10	7	4	0	0	0
160.	45.	188	142	108	82	62	47	35	27	20	15	12	9	7	5	5
157.	45.	108	71	47	31	20	13	9	6	4	3	2	1	0	0	0
160.	55.	438	289	190	125	83	55	36	24	16	10	7	4	0	0	0
157.	55.	838	635	481	364	276	209	158	120	91	69	52	39	30	23	23
158.	65.	938	710	538	408	309	234	177	134	102	77	58	44	33	25	25
161.	65.	438	332	251	190	144	109	83	63	47	36	27	21	16	12	12
164.	65.	538	407	309	234	177	134	102	77	58	44	33	25	15	15	15
167.	75.	638	483	366	277	210	159	120	91	69	52	40	30	23	17	17
172.	75.	688	521	395	299	226	172	130	98	75	56	43	32	25	19	19
164.	75.	238	144	87	53	32	20	12	7	4	3	0	0	0	0	0
161.	75.	438	289	190	125	83	55	36	24	16	10	7	4	0	0	0
158.	75.	438	332	251	190	144	109	83	63	47	36	27	21	16	12	12
157.	85.	238	180	136	103	78	59	45	34	26	20	15	11	8	6	6
160.	85.	438	289	190	125	83	55	36	24	16	10	7	4	0	0	0
163.	85.	138	104	79	60	45	34	26	20	15	11	9	6	5	4	4
156.	95.	188	142	108	82	62	47	35	27	20	15	12	9	7	5	5
160.	95.	188	142	108	82	62	47	35	27	20	15	12	9	7	5	5
172.	108.	438	332	251	190	144	109	83	63	47	36	27	21	16	12	12
168.	116.	438	332	251	190	144	109	83	63	47	36	27	21	16	12	12
164.	116.	388	294	223	169	128	97	73	55	42	32	24	18	14	10	10
160.	105.	688	521	395	299	226	172	130	98	75	56	43	32	25	19	19
156.	105.	738	486	321	211	139	92	61	40	26	17	11	8	0	0	0
156.	115.	438	289	190	125	83	55	36	24	16	10	7	4	0	0	0
160.	118.	688	521	395	299	226	172	130	98	75	56	43	32	25	19	19
156.	125.	38	25	16	11	7	5	3	2	1	1	1	0	0	0	0
156.	135.	10	7	4	3	2	1	1	1	0	0	0	0	0	0	0
160.	133.	10	8	6	4	3	2	2	1	1	1	1	0	0	0	0
164.	134.	168	127	96	73	55	42	32	24	18	14	10	8	6	5	5
168.	134.	418	316	240	182	138	104	79	60	45	34	26	20	15	11	11
172.	143.	638	483	366	277	210	159	120	91	69	52	40	30	23	17	17
168.	151.	438	332	251	190	144	109	83	63	47	36	27	21	16	12	12
164.	151.	38	29	22	16	12	9	7	5	4	3	2	2	1	1	1
160.	145.	188	142	108	82	62	47	35	27	20	15	12	9	7	5	5
157.	145.	188	124	82	54	35	23	15	10	7	4	3	2	0	0	0
157.	155.	438	289	190	125	83	55	36	24	16	10	7	4	0	0	0
160.	155.	368	279	211	160	121	92	69	53	40	30	23	17	13	10	10
180.	0.	1038	786	595	451	342	259	196	148	112	85	65	49	37	28	28